A full dimensional Discrete Variable Representation of H_2^+ and H_2 photoionization

Denis Jelovina

Departamento de Química
Universidad Autónoma de Madrid

This dissertation is submitted for the degree of
Doctor of Philosophy

September 2017

Abstract

The development of new accurate theoretical methods that are able to describe ultrafast photo-induced processes in molecules has become an active field of research with the advent of new ultrashort radiation sources. The progresses in laser technology in the last few years made possible the observation and manipulation of electron and nuclear dynamics at their intrinsic time scales. The complexity associated with the coupled electron and nuclear motion in molecular targets requires precise simulations to interpret, understand and predict the wide range of photo-induced ultrafast phenomena. This thesis has been focused on the development of a new numerical method to investigate multiphoton breakup processes of H_2 and H_2^+ molecular systems. Most existing methods are restricted to the study of excitation or single ionization working withing the fixed nuclei or the Born-Oppenheimer approximations. Our implementation includes all electronic and nuclear degrees of freedom, beyond the widely employed Born-Oppenheimer approximation. Our goal is to explore multiphoton processes induced by relatively intense fields, leading to single or double ionization of the system. Our approach thus implies the solution of the time-dependent Schrödinger equation in full dimensionality. The numerical wave function is represented in a single center expansion, combining spherical harmonics for the angular dependencies of the particles, while both nuclear and electronic radial components are described by *finite element method-discrete variable representation* basis functions. By using *exterior complex scaling* transformation of the electronic and nuclear spatial coordinates, the correct boundary conditions are implicitly imposed, allowing extraction of physical observables from the Coulomb breakup process. The method provides accurate total, energy- and angle-differential probabilities associated to excitation, ionization and dissociation events. We also discuss in detail the advantages, limitations, accuracy and numerical issues of our implementation with respect to the existing approaches.

We present the first application of the method to the H_2^+ system, where we show how to emulate a conventional pump-probe scheme using a single frequency-chirped ultrashort UV pulse to obtain a time-resolved image of ultrafast molecular dynamics. We also show that by tuning the chirp of the pulse, while keeping the spectral distributions

constant, one achieves a significant amount of control of the total ionization yields. We discuss our preliminary results on the H_2 molecular system, where we obtain one- and two-photon single and double ionization yields differential in angle and energy of the ejected particles. We benchmark our new implementation by comparison with existing data, when available, and introduce alternative approaches to extract transition (excitation and ionization) amplitudes from a numerically computed molecular wave packet.

We conclude providing a complete discussion on the formalism for the first accurate theoretical description of two-photon full breakup of H_2, we complete the formalism sufficient for the realistic description of two-photon breakup of H_2 molecule, which can be consider as advance towards the correct description of photo-induced molecular dynamics.

Resumen

El desarrollo de nuevos métodos teóricos con la precisión necesaria para describir procesos ultrarrápidos foto-inducidos en moléculas se ha convertido en una activa área de investigación tras la aparición de nuevas fuentes de radiación láser ultracorta. Los progresos en tecnología láser en los últimos años han hecho posible la observación y manipulación de la dinámica electrónica y nuclear en sus tiempos de escala naturales. La complejidad asociada al movimiento acoplado de electrones y núcleos en especies moleculares requiere de simulaciones precisas para interpretar, entender y predecir un amplio rango de fenómenos ultra-rápidos inducidos por luz. Esta tesis se centra en el desarrollo de nuevas herramientas numéricas para investigar la ruptura completa de los sistemas moleculares de H_2^+ y H_2 por absorción multi-fotónica. La mayor parte de los métodos existentes emplean la aproximación de Born-Oppehenimer y se restringen al estudio de la excitación o ionización simple. Nuestra implementación incluye todos los grados de libertad electrónicos y nucleares trabajando más allá de la aproximación Born-Oppenheimer. Nuestro objetivo es estudiar procesos multi-fotónicos inducidos por campos láser relativamente intensos, dando lugar a la ionización simple o doble el sistema molecular. El método por tanto resuelve la ecuación de Schr odinger dependiente del tiempo en toda su dimensionalidad. La representación numérica de la función de onda se hace mediante una expansión, combinando armónicos esféricos para tratar la dependencia angular de las partículas, mientras que las componentes radiales tanto nucleares como electrónicas se describen mediante una base empleando una representación de variable discreta en un método de elementos finitos (FEM-DVR). Las condiciones de contorno para el problema de fotoionización se imponen de forma implícita al emplear una transformación de escalado exterior complejo (ECS), lo que permite extraer los observables físicos para el proceso de ruptura Coulombiana. La metodología proporciona probabilidades totales y diferenciales en ángulo y energía, para los procesos de excitación, ionización y disociación. En este trabajo, se discuten en profundidad las ventajas, limitaciones, precisión y detalles numéricos de nuestra implementación con respecto a los métodos existentes.

Presentamos la primera aplicación del método al sistema de H_2+, donde mostramos cómo emular un esquema convencional de bombeo-prueba (pump-probe) usando un único pulso ultracorto en la región del UV definido con una frequencia que varía en el tiempo (chirp). Se ha demostrado que ajustando el parámetro de frequencia chirp -, y manteniendo invariable la distribución espectral del pulso, es posible controlar de forma significativa la eficiencia de ionización total. También, se discutirán nuestros resultados preliminares en estudios de fotoionización de la molécula de H_2, donde obtenemos probabilidades de ionización simple y doble por absorción de dos fotones. Dichas probabilidades también se presentan diferenciales en ángulo y energía de las partículas emitidas. Los resultados obtenidos se han comparado con los escasos datos existentes en la literatura con el fin de testear nuestra implementación. Además, esto ha permitido evaluar la precisión de diversos métodos para la extracción de las amplitudes de transición, tanto de excitación como de ionización, del paquete molecular numérico.

Concluimos, proporcionando una discusión detallada del formalismo que permite obtener la primera descripción teórica de la ruptura completa de la molécula de hidrógeno por absorción de dos fotones.

Table of contents

List of figures

List of tables

Nomenclature

Acronyms / Abbreviations

BO	Born–Oppenheimer
DE	Dissociative Excitation
DI	Dissociative Ionization
DVR	Discrete Variable Representation
ECS	Exterior Complex Scaling
FEL	Free Electron Laser
FEM	Finite Element Method
FNA	Fixed-nuclei approximation
HHG	High-order Harmonic Generation
IR	Infrared
LOPT	Lowest-order Perturbation Theory
MPI	Message Passing Interface
TDSE	Time-dependent Schrödinger Equation
UV	ultraviolet
XUV	Extreme Ultraviolet

Chapter 1

Introduction

The remarkable technological advances of free-electron-laser facilities and high-harmonic generation setups have opened the way to the production of intense and ultrashort ultraviolet (UV) pulses with durations in the femtosecond and attosecond range [36, 38, 8, 7]. These sources have opened the path to probe electron dynamics in atoms and molecules, generating pulses with durations in the the attosecond regime ($1as = 10^{-18} seconds$), which allows one probing time-resolved electronic motion [42, 18]. Time-resolved imaging and control of electron and nuclear dynamics in molecules has thus gained relevance in recent studies in physics, chemistry and even biology [89, 74].

The interaction of atoms and molecules with ultrashort pulses may lead to the fragmentation of the system, i.e. involve unbound states to the process. Molecular targets enriches the problem and introduces the difficulty of simultaneous treatment of electronic and nuclear motion. Accurate theoretical descriptions of unbound or continuum states in molecules is far from being a standard problem. Nevertheless, the number of theoretical works devoted to this kind of studies has significantly increased in the last few years due to the multidisciplinary character of the problem, as object of study for a variety of disciplines such as Atomic and Molecular Physics, Quantum Chemistry or Condensed Matter Physics.

Intense XUV pulses in the femtosecond and attosecond time domains are nowadays created through high-order harmonic generation (HHG) [73, 38] or free electron lasers (FEL) [4], offering the possibility of a new class of pump-probe experiments that can explore the dynamics of the electronic motion in molecules on ultrashort time scales and its coupling to the nuclear degrees of freedom. A deep knowledge and interpretation of such experiments inevitably involves state-of-the-art time-dependent theoretical methods, implemented in the most advanced computing resources.

The aim of this PhD work is to build a new set of theoretical tools to give an accurate and full description of the ultrafast coupled electron and nuclear dynamics involved in molecular fragmentation processes. In particular, we will focus of multiphoton Coulomb breakup of small molecules, for which current theoretical methods cannot be applied. The challenge that this problem presents is better illustrated by the existing approaches to treat the same, but much simpler, problem in atoms. For instance, along the last decade, several efforts have been made to solve two-photon double ionization in helium atom. Only in the last few years, an agreement between different theoretical approaches [61, 20] and experiments [77] was reached. Moreover, the role of electron correlation and the dynamics to be probed with intense XUV ultrashort pulses in pump-probe schemes on atoms is still open and subject of discussion, field in which important progress has been made [63]. This work is a further step in this field by exploring similar process in molecules to explain the role of ultrafast nuclear motion combined with the electron dynamics.

The theoretical description of the interaction of molecule with ultrafast pulses requires the solution of time-dependent non-relativistic Schrödinger equation (TDSE). The inability to obtain a solution of TDSE for any but the simplest physical systems, requires use of different approximation and simplification, producing results not always comparable with the experiments. Furthermore, even a numerical solution of Schrödinger equation for many body system does not eliminate problem of extraction of physical observables, due to unknown closed-form asymptotic solution of the three (and more) particle quantum problem. Rapid growth of computational resources and parallel development of theoretical methods in the last decades has made possible exact numerical treatment of the simplest few-body systems. For many years, the impossibility to describe both electronic and dissociative continua prevented a correct interpretation of the spectra obtained in several experiments, even for the simplest molecules. In the last decade, numerical methods have become available, accounting for a simultaneous description of both continua, for instance, studies on dissociative photoionization are now accessible theoretically [46], having a wide applicability in Astrophysics and Atmospheric Chemistry. The success of these numerical methods is due to their ability to reproduce the electronic continuum states far from the nuclei.

Single ionization problems in molecules have been successfully addressed within BO approximation by well established and accurate spectral methods [5], providing a realistic description of molecular processes that involve both electrons and nuclei. Such a quantum description is sufficient to explore phenomena such as excitation of doubly excited states that can subsequently decay through autoionization. In the

photoionization of H_2 molecules, autoionization occurs while the molecule dissociates, so that both electron and nuclear motions occur on the same time scale, and therefore must be properly described in the theoretical treatment. These spectral methods have allowed the description of the electron spectra, for instance, upon autoionization in H_2 pumped by attosecond XUV pulse and recorded in the presence of a weak IR field. This approach has pioneered the analysis of attosecond autoionization dynamics in the presence of weak IR fields, leading to the understanding [70] of the novel physics that underlies striking asymmetries in photoelectron spectra [46], however it is not adequate for the description of processes where electron-electron correlation in continuum plays an important role. The difficulty lays in the fact that full Coulomb breakup implies two electrons being ejected from the target, therefore one has to solve a multi-body break up problem. Existing spectral methods cannot properly describe the process, given the high photon energies involved and the fact that the final continuum state is defined by three or more charged particles.

Electron-electron correlations in continuum states have been accurately represented in time-independent treatment of one-photon [51], and two-photon double ionization of helium atom [55]. But only very recently, different approaches [61, 20] agreed in time-dependent description of two-photon double ionization of helium atom. The successful implementation [61] gives a clue how to treat two-electron correlation in an equivalent molecular case, but not offering answer how to describe molecular electron-nuclear correlation in Coulomb breakup or dissociation continuum. A correct representation of molecular electron-nuclear interaction has been demonstrated in [83], where in time-independent approach, single-photon double ionization of hydrogen molecule in fixed-nuclei approximation (FNA) has been solved. This approach has been extended to two-photon double ionization problem of hydrogen molecule in FNA [30] . There is still relatively small number of currently available time dependent methods [32, 25] for two-photon double ionization problem of hydrogen molecule in FNA. Besides single ionization, the two-photon breakup of hydrogen molecule within a full dimensional description and with nuclear motion remains unsolved.

We thus focus on the development of a theoretical formalism and a new numerical tool for complete quantum description of electrons and nuclei including all correlations in full dimensionality and beyond the Born-Oppenheimer approximation. Different from any existing spectral methods, the numerical approach that we use allows the extraction of the Coulomb breakup channel. Moreover, we are able to extract differential probabilities in energy and angles of emission of both ejected electrons and nuclei.

We have developed a new set of codes that solve the time-dependent Schrödinger equation (TDSE) using a numerical representation of the molecular wave-packet in terms of FEM-DVR (finite element method combined with a discrete variable representation) basis functions and employs a Exterior Complex Scaling (ECS) formalism to solve the scattering problem for the complete fragmentation [49]. We have used, as reference, an similar approach successfully employed to solve multiphoton double ionization of helium atom [61] and for double ionization of H_2 within the fixed nuclei approximation [83]. We have gone a step forward and have performed the first implementation that enables the description of molecular double ionization including nuclear motion, although in the present manuscript only preliminary results on multiphoton double ionization in full dimensionality are presented. We have explicitly constructed time-dependent Hamiltonian operator, accounting all interactions between all particles in the system with all degrees of freedom. In contrast to the spectral methods, we account for the all possible excitation and breakup channels, avoiding an explicit description of such channels. Most of the existing methods solve the TDSE under the influence of the field and then project onto final states in order to extract their corresponding amplitudes. When looking at Coulomb breakup channels, the description of the final double continuum states remains a challenge, since the final state is defined by three or more charged particles. Another difficulty when using time-dependent methods is to determine the limits of integration: the wave packet is propagated in time while the system is exposed to the electromagnetic field, but, once the radiation ends, the particles, electrons and nuclei, are still interacting, so that one needs keep propagating until reaching asymptotic limit, at which the rate does not depend on the final time of integration. The key point is to find this limit. To avoid these difficulties, we will use the approach in which for the extraction of the different channels one firstly solve the time-independent Schrödinger equation using as initial condition the propagated wave packet, which implies implicit integration until infinite time [62], and then from the calculated scattering wave function, extracts the amplitudes which can be expressed as a surface integral [49]. In this way, all energy and angular differential probabilities can be extracted. This formalism has proven its applicability on two-electron systems allowing a proper description of double-electronic continuum states.

We aim to develop the first time-dependent ab initio calculation on multiphoton double ionization of molecules. For obvious reasons, we will apply it to the simplest molecule in which double ionization can take place, the hydrogen molecule. To apply this method in H_2 molecule we need to properly describe nuclear motion, electronic motion in the presence of two-center potential, as well as electron-electron and electron-nuclear

interactions. Implementation of the surface integral technique requires construction so called *testing function*, which reproduces asymptotic behavior of the final sate in a channel of interest. It has been shown for Coulomb breakup, for helium atom and hydrogen molecule in FNA [61, 83], that two-electron testing function can be constructed as an uncorrelated product of single electron functions. The question that we address in this work is how to construct a testing function for a system with electronic and nuclear motion. To answer, this large part of this work we devote to development of the method for molecular hydrogen ion, where we show that the testing function for Coulomb breakup can be written as uncorrelated product of Coulomb functions describing nuclear motion and one-electron testing function in presence of two-center potential [83]. Surface integral technique can be equally well applied in time-independent perturbation theory as in TDSE, therefore will demonstrate agreement between the two approaches for single-photon absorption processes. Small part of this work we devote to implementation and demonstration of agreement with previous implementation of the same method for H_2 system in FNA. Having the method implemented for H_2^+ system in full dimensionality and H_2 in FNA, we have all ingredients for implementing the method in H_2 system, which presents huge technical challenge and unfortunately has not been performed to the conclusion of this work.

The high dimensionality of the problem implies implementation of huge matrices; therefore we employ a parallel implementation of the codes. In this point, we deal with the most recent software under MPI (message passing interface). In particular, we use the last updates of sparse matrix methods available on PETSC (Portable, Extensible Toolkit for Scientific Computation) and SLEPc (Scalable Library for Eigenvalue Problem Computations) libraries. Therefore we work in the frontier of the current possibilities of computational techniques, where state-of-the-art quantum chemistry, atomic physics and mathematical numerical analysis merge together. The impressive development of computers in the last few years allows one to consider more and more complex systems and to increase our ability to make realistic predictions that can guide future experiments.

The thesis is organized as follows. The newly developed methodology is described in chapters 2 to 5, including computational and numerical details. Chapters 6 and 7 present the first applications of our method in H_2^+ and H_2, respectively.

Chapter 2 provides a general theoretical framework on the description of the molecule fragmentation that will be investigated in this work, independently of particular method employed. We focus on mathematical expression for the non-relativistic Hamiltonian of H_2^+ and H_2 systems, i.e. the quantum description of the molecular structure, symmetry

properties and interactions with electromagnetic radiation treated in semi-classical dipole approximation in length and velocity gauges.

Chapter 3 gives the details of numerical representation of the wave function, Hamiltonian and interactions with electromagnetic radiation for H_2^+ and H_2 systems. It describes single center expansion of wave functions, where all angular dependencies are represented by spherical harmonic functions while radial dependencies of both electronic and nuclear motion are described by FEM-DVR functions using exterior complex scaling (ECS). Details of FEM-DVR discretization technique, which is frequently refered trough this work, is given here. We briefly discuss the boundary conditions of the photoabsorption problem at hand, and then give the self-contained numerical details of implementation of all relevant operators. Although we only provide preliminary data for the description of H_2 double photoionization including nuclear motion, this chapter includes a formalism and computational details for its correct implementation.

In chapter 4, we discuss the expressions of scattering theory to treat molecular fragmentation of H_2^+ and H_2 upon photo-absorption. In particular, we explain the advantages and limitations of employing time-dependent and time-independent approaches, as well as the formalism to extract transition (excitation and ionization) amplitudes from the numerical wave function. Specifically, we have implemented three different approaches. First, the optical theorem that provides accurate results for total photo-absorption yields. Then, we provide the specifics of the "quantum-mechanical flux", which allows us to disentangle dissociation and ionization channels. And, finally, we introduce the "surface integral technique" that can provide accurate energy and angular differential excitation and ionization amplitudes for all possible fragmentation channels. The comparison of the results obtained in these approaches is used as a benchmark to test the validity of our method.

Chapter 5: We provide a detailed analysis of the advantages, limitations, accuracy and numerical implementation for the extraction methods described in the previous section for H_2^+ system. We discuss the most relevant details of the implementation to compute the eigenstates, specifically, convergence issues associated to the solution of the eigenvalue problem to retrieve the initial state of the molecular target in our FEM-DVR implementation. In a second step, we demonstrate the validity of our method to compute photoionization cross sections in the H_2^+ system, by comparison with recent works, using both time-dependent and time-independent approaches. In the third place, we present a detailed study on the solution of the TDSE and the capabilities of our implementation to solve multiphoton ionization and excitation processes in one- and

two-electron diatomic molecular targets. Finally, we test the accuracy of the method by comparison with multiphoton single ionization problems in H_2^+.

Chapters 6 shows the first application of our methodology. We show how to emulate a conventional pump-probe scheme using a single frequency-chirped ultrashort UV pulse to obtain a time-resolved image of molecular ultrafast dynamics. The chirp introduces a spectral phase in time that encodes the delay between the pump and the probe frequencies contained in the pulse. By comparing the results of full dimensional ab initio calculations for the H_2^+ molecule with those of a simple sequential model, we demonstrate that, by tuning the chirp parameter, two-photon energy-differential ionization probabilities directly map the wave packet dynamics generated in the molecule. As a result, one can also achieve a significant amount of control of the total ionization yields, with possible enhancement by more than an order of magnitude [34].

In chapter 7, we present the most recent results on single- and multiphoton double ionization of the hydrogen molecule. We discuss the efficiency of the method on the computation of the molecular structure of the neutral molecule in comparison with existing theoretical data. We then solve the one-photon single and double ionization of H_2, with particular interest on the energy- and angle-differential probabilities, and compare with previous works when available. Finally, we show our most recent simulation on two-photon double ionization of H_2.

Chapter 2

Theory

We have developed a new numerical method to explore photo-induced Coulomb breakup processes in molecules. We focus on the simplest molecular systems in nature: the hydrogen molecular ion H_2^+ and the hydrogen molecule, H_2. These are the only targets that, with the current computational power, allow one for an exact full-quantum mechanically description giving access to an accurate simulations to reproduce photo-induced processes and elucidate the role of electron-electron and electron-nuclear correlation terms. A number of methods have been developed over the last years in order to describe photoionization of these molecular targets, employing different levels of approximation. However, none of the existing methods are able to solve the multiphoton Coulomb breakup of the H_2 molecule in full dimensionality. In the one hand, one needs to address the unsolved problem of describing the full-body breakup problem with three (H_2^+) or four charged (H_2) particles in the continuum, with no analytical solution available. A few methods have explored the H_2^+ multiphoton ionization employing grid methods [26, 75], with limited applications due to the size of the problem. For H_2 photoionization, the only existing reliable method to our knowledge, where both electron and nuclear degrees of freedom are taken into account, is a spectral method developed in the last two decades [69]. However, this methodology employs a close-coupling approach to treat the electronic continuum, that it is only valid to treat single ionization problems, with one electron in the continuum [46]. Moreover, this method employs Born-Oppenheimer approximation to describe the wave function and separately treats the nuclear dependencies only parametrically, i.e. ignoring the so-called adiabatic couplings, which may play an important role in a number of photoinduced processes, like neutral dissociation upon multiple excitation. In this context, and taking into account the availability of newly developed laser sources that generate UV and XUV pulses with enough intensity to induce multiphoton ionization,

together with detection techniques that can measure all photo-framents in coincidence, there is a need for exact methods that can address single and double ionization events in simple molecules accounting for all electron-electron and electron-nuclear interactions. This is the goal of our investigation.

In this chapter, we present the theory necessary to achieve a full-dimensional, full quantum mechanical description, beyond the BO approximation, of the H_2^+ and H_2 molecules in the presence of highly and moderately intense laser fields. The time evolution of the molecular system under the influence of an external field can be treated using a perturbative approach or directly solving the time-dependent Schrödinger equation. In the next chapter, we will describe both approaches that have been used in different contexts for molecular photoionization. We discuss in detail, in both methods, the molecular system treated fully quantum-mechanically, while the interaction with the laser radiation is represented semiclassically, i.e. the electromagnetic field is assumed to be properly described with classical mechanics expressions. In other words, we will investigate photo-induced processes using radiation with enough photons such that the radiation can be classically described. Moreover, the interaction between the laser field and the molecular target is treated within the dipole approximation, i.e. the wave-lengths associated to few-photon ionization processes are much larger than the typical distances where the interaction takes place, therefore one can ignore the spacial dependence of the electromagnetic field validating the dipole approximation. All details are provided in the next sections. We pay special attention to the technical details regarding the numerical treatment employed to treat electronic and nuclear degrees of freedom at equal footing. In brief, we will use a single center expansion for the angular components, which simplifies the computational implementation at the cost of requiring larger basis sets. For the spacial coordinates, both electronic and nuclear, we employ a Finete Element method combined with a Discrete Variable Representation, which has been shown to largely improve the computational efficiency with respect to existing methods using a grid representation [75]. Firstly we give the expression for field-free Hamilton and list its symmetry properties, firstly for H_2^+ system and then for H_2, which includes all internal electromagnetic interactions. Then we present the formalism for semi-classical treatment of the electromagnetic radiation with a system described fully quantum mechanically. Within semi-classical approximation we describe the dipole approximation, that we employ. And finally, we give a short overview of units we use in the rest of the thesis.

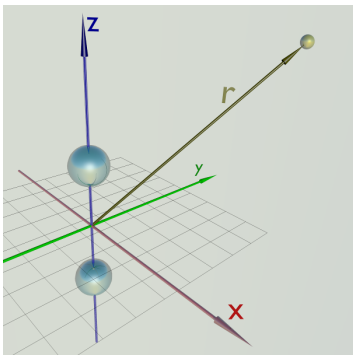

Fig. 2.1 Coordinate system for H_2^+ system, cyan: protons, yellow: electron.

2.1 Hydrogen molecule ion H_2^+

As a benchmark we use the simplest molecular system available, the hydrogen molecule ion, consisting of two nuclei and one electron. It enables one to study nuclear dynamics and electron-nuclear correlation effects using a full quantum treatment in full dimensionality with the current computational capabilities.

The hydrogen molecular ion, consists of two nuclei (at positions $\boldsymbol{R_1}$ and $\boldsymbol{R_2}$, with charges e and masses m_n) and one electron (at position $\boldsymbol{r}$, with charge $-e$ and masses m_e), as shown in figure 2.1. The non-relativistic Hamiltonian is given by the sum of kinetic energy operators and all inter-particle interaction operators.

$$\hat{\boldsymbol{H}}_0 = \frac{1}{2m_n}\left(\hat{\boldsymbol{P}}_{R_1}{}^2 + \hat{\boldsymbol{P}}_{R_2}{}^2\right) + \frac{1}{2m_e}\hat{\boldsymbol{p}}_r{}^2 + \sum_{i=1}^{2}\frac{-e^2}{|\boldsymbol{r}-\boldsymbol{R}_i|} + \frac{e^2}{|\boldsymbol{R}_1-\boldsymbol{R}_2|}, \tag{2.1}$$

where $\hat{\boldsymbol{P}}_{R_i} = -i\boldsymbol{\nabla}_{R_i}$ and $\boldsymbol{R}_i$ are nuclear momentum and position operators, and $\hat{\boldsymbol{p}}_r = -i\boldsymbol{\nabla}_r$ and $\boldsymbol{r}$ are electronic momentum and position operators.

We are going to use center-of-nuclear-mass by introducing coordinates

$$\boldsymbol{R} = \boldsymbol{R}_1 - \boldsymbol{R}_2 \tag{2.2}$$

$$\boldsymbol{Q} = \boldsymbol{R}_1 + \boldsymbol{R}_2 \tag{2.3}$$

to be able to separate internal dynamics, which we are interested in, from kinetic energy of the (center of mass of) nuclei described by $\boldsymbol{Q}$ coordinate.

We chose a coordinate system where the nuclei are placed in the z-axis, and center-of-nuclear-mass corresponds to the origin, where $\boldsymbol{Q} = 0$ and consequently $\boldsymbol{R}/2 = \boldsymbol{R}_1 = -\boldsymbol{R}_2$. Then, Hamiltonian describing internal degrees of freedom, in the absence of any external interaction ($\hat{\boldsymbol{H}}_0$) can be expressed as

$$\hat{\boldsymbol{H}}_0 = \frac{\hat{\boldsymbol{P}}_R^{\,2}}{2\mu_n} + \frac{\hat{\boldsymbol{p}}_r^{\,2}}{2m_e} + \frac{-e^2}{|\boldsymbol{r} - \boldsymbol{R}/2|} + \frac{-e^2}{|\boldsymbol{r} + \boldsymbol{R}/2|} + \frac{e^2}{R}, \tag{2.4}$$

where we neglect the mass polarization term. The time independent Schrödinger equation for the simplest molecular system,

$$\hat{\boldsymbol{H}}_0 \left|\Psi\right\rangle = E \left|\Psi\right\rangle, \tag{2.5}$$

is not separable in the nuclear and electronic coordinates, and does not have an analytic solution even for the simplest molecular system in spherical coordinates. Nevertheless, the molecular system has certain symmetry, associated to a different operators within the Hamiltonian, which allows us to classify the resulting eigenstates in equation 2.5, and therefore, to reduce the size of the problem in certain scenarios.

For the problems that we are interseted in, the relativistic effects for single-electron system, of light molecules can be neglected, therefore the spin-orbit coupling term is ignored in Hamiltonian.

In the absence of the external field, the system has the axial symmetry, in other words Hamiltonian commutes with the z-projection of angular momentum operator: $[\hat{\boldsymbol{H}}_0, \hat{J}_z] = 0$, which means they can be simultaneously diagonalized, and m is a good quantum number. In electronic state notation, different values of m are designated by Greek letters, where $m = 0, 1, 2...$ correspond to σ, π, δ ... .

In the contrast to the atomic case, the system doesn't have spherical symmetry, and l is not a good quantum number. The parity operator, $\hat{\Pi}$, also commutes with the Hamiltonian, which is related to the symmetry of the system with respect to the inversion:

$$\hat{\Pi}\Psi(\boldsymbol{r}) = (-1)^{\pi}\Psi(-\boldsymbol{r}) \tag{2.6}$$

where $\pi = 0$ corresponds to *gerade* (*even*) symmetry, and $\pi = 1$ corresponds to *ungerade* (*odd*) symmetry. Because of the parity of spherical harmonics functions

$$Y_l^m(\hat{\boldsymbol{r}}) = (-)^l Y_l^m(-\hat{\boldsymbol{r}}) \tag{2.7}$$

in the expansion of wave function in spherical harmonics, contributions with $l = 0, 2, 4...$ will corresponds to *gerade* symmetry, while $l = 1, 3, 5...$ will corresponds to *ungerade* symmetry. As we will see later, in one photon transition, the dipole operator always change the state of the system form *gerade* to *ungerade* symmetry and vice versa.

2.2 Hydrogen molecule H_2

The simplest and more abundant neutral molecule in nature is the hydrogen molecule, has an additional electron, which introduces electron-electron correlation enriching the problem and giving rise to a variety of new phenomena.

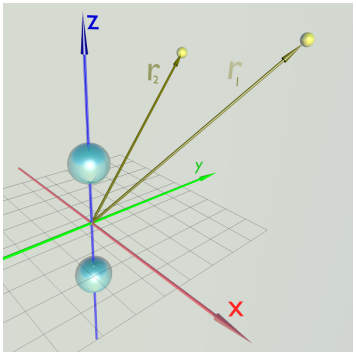

Fig. 2.2 Coordinate system for H_2 system, cyan: protons, yellow: electron.

For hydrogen molecule we use the same approximations as in the ion case. The mass polarization term is neglected, the spin effects are also neglected, however we cannot ignore the effects of *Pauli exclusion principle* which are latter taken into account in the construction of basis functions. The non-relativistic Hamiltonian of an isolated system has an additional terms (in comparison to H_2^+), coming from second electron-nuclear interaction and electron-electron interaction term, written in center-of-nuclear-mass, has the following form in coordinates indicated in figure 2.2,

$$\begin{aligned}\hat{\boldsymbol{H}}_0 =& \frac{\hat{\boldsymbol{P}}_R^{\,2}}{2\mu_n} + \frac{\hat{\boldsymbol{p}}_{r_1}^{\,2}}{2m_e} + \frac{\hat{\boldsymbol{p}}_{r_2}^{\,2}}{2m_e} \\ &+ \frac{-e^2}{|\boldsymbol{r}_1 - \boldsymbol{R}/2|} + \frac{-e^2}{|\boldsymbol{r}_1 + \boldsymbol{R}/2|} + \frac{-e^2}{|\boldsymbol{r}_2 - \boldsymbol{R}/2|} + \frac{-e^2}{|\boldsymbol{r}_2 + \boldsymbol{R}/2|} \\ &+ \frac{e^2}{|\boldsymbol{r}_2 - \boldsymbol{r}_1|} + \frac{e^2}{R}.\end{aligned} \tag{2.8}$$

Again, one can take the advantage of the commutation properties of operators that Hamiltonian commutes with, and that allow us to classify eigenstates by symmetry.

All spin effects are ignored except *Pauli exclusion principle*, which we explicitly include in the construction of basis functions. The permutation operator, $\hat{P}_{12}$, which exchanges electrons positions, and which acts on two-electron wave function in the following way:

$$\hat{P}_{12}\Psi(\boldsymbol{r}_1, \boldsymbol{r}_2) = \Psi(\boldsymbol{r}_2, \boldsymbol{r}_1), \tag{2.9}$$

and therefore, the eigenstates can be symmetric ($P = 0$) or anti-symmetric ($P = 1$) under the exchange of positions of the two electrons

$$\hat{P}_{12}\Psi(\boldsymbol{r}_1, \boldsymbol{r}_2) = (-1)^P \Psi(\boldsymbol{r}_2, \boldsymbol{r}_1). \tag{2.10}$$

The Hamiltonian (2.8) commutes with the permutation operator, so they can be simultaneously diagonalized, having eigenstates either symmetric or anti-symmetric under the exchange (of positions) of the electrons,

$$\hat{P}_{12}\Psi_s(\boldsymbol{r}_1, \boldsymbol{r}_2) = \Psi_s(\boldsymbol{r}_2, \boldsymbol{r}_1) \tag{2.11}$$

$$\hat{P}_{12}\Psi_a(\boldsymbol{r}_1, \boldsymbol{r}_2) = -\Psi_a(\boldsymbol{r}_2, \boldsymbol{r}_1). \tag{2.12}$$

The total electronic wave function can be written as a product of a function describing the spatial dependence (Ψ) and a function for the spin component ($|\uparrow\rangle$ and $|\downarrow\rangle$), which can be symmetric (triplet, $S = 1$) or antisymmetric (singlet, $S = 0$) under electrons exchange. Since electrons are fermions, the total wave functions has to be anti-symmetric under exchange of electrons, which gives us two possibilities, one for singlet state

$$|\Psi_p\rangle = |\Psi_s\rangle \otimes \frac{1}{\sqrt{2}} \left(|\uparrow\downarrow\rangle - |\downarrow\uparrow\rangle\right), \tag{2.13}$$

and one for triplet states

$$|\Psi_o\rangle = |\Psi_a\rangle \otimes \begin{cases} |\uparrow\uparrow\rangle \\ \frac{1}{\sqrt{2}} \left(|\uparrow\downarrow\rangle + |\downarrow\uparrow\rangle\right) \\ |\downarrow\downarrow\rangle \end{cases} \tag{2.14}$$

Where (electronic) space–symmetric wave functions are called *para* states (Ψ_p), while space–anti-symmetric wave functions are called *orto* states (Ψ_o). We are going to use the non-relativistic Hamiltonian and the dipole approximation for the description of interaction with the electromagnetic field, where transitions from one spin state to the another are forbidden, and we will always assume the molecule is in its initial ground state (a spin-singlet state). Therefore, only the wave functions that are anti-symmetric with the respect to the exchange of spatial coordinates will be considered in this work.

The operator associated to the projection of the total orbital angular momentum to the molecular axis ($\hat{J}_z$) also commutes with the Hamiltonian, $[\hat{\boldsymbol{H}}_0, \hat{J}_z] = 0$. The total angular momentum operator, is given by the sum of single electron angular momentum

operators,

$$\hat{\boldsymbol{J}} = \hat{\boldsymbol{J}}_1 + \hat{\boldsymbol{J}}_2, \tag{2.15}$$

and the projections to the molecular (z) axis is determined by M quantum number. In classifications of electronic eigenstates, different values $M = 0, 1, 2...$ are designated by capital Greek letters Σ, Π, Δ....

As in the case of H_2^+, the parity operator $\hat{\Pi}$ reflects the symmetry of the system

$$\hat{\Pi}\Psi(\boldsymbol{r}_1, \boldsymbol{r}_2) = (-1)^{\pi}\Psi(-\boldsymbol{r}_1, -\boldsymbol{r}_2), \tag{2.16}$$

where $\pi = 0$ corresponds to *gerade* (*even*) symmetry, and $\pi = 1$ corresponds to *ungerade* (*odd*) symmetry. In the expansion of wave function in (both, uncoupled $Y_{l_1}^{m_1}(\hat{\boldsymbol{r}}_1)Y_{l_2}^{m_2}(\hat{\boldsymbol{r}}_2)$ and coupled $\mathcal{Y}_{l_1,l_2}^{L,M}(\hat{\boldsymbol{r}}_1, \hat{\boldsymbol{r}}_2)$) spherical harmonics, contributions with $l_1 + l_2 = 0, 2, 4...$ will corresponds to *gerade* symmetry while $l_1 + l_2 = 1, 3, 5...$ will corresponds to *ungerade* symmetry. As already mentioned, for the two-electron wave function, the dipole operator in one photon transition, enforces transitions from *gerade* to *ungerade* symmetry state and vice versa.

2.3 Laser-molecule interaction

The interaction of a single charged particle (the charge of the electron is $-e$), with the electromagnetic field, is given by (gauge-dependent) Hamiltonian

$$\hat{\boldsymbol{H}} = \frac{\left(\hat{\boldsymbol{p}} + \frac{e}{c}\boldsymbol{A}(\hat{\boldsymbol{r}}, t)\right)^2}{2m} - e\Phi(\hat{\boldsymbol{r}}, t) \tag{2.17}$$

where electromagnetic field is described by vector potential $\boldsymbol{A}(\hat{\boldsymbol{r}}, t)$.

2.3.1 Semi-classical approximation

The electromagnetic field describing a finite laser pulse can be written using classical mechanics. Lasers have associated a large number of photons such that it can be assumed to be a continuous variable and the quantisation of the electromagnetic field is avoided. For coherent fields, the vector potential $\boldsymbol{A}(\hat{\boldsymbol{r}}, t)$ and scalar potential $\Phi(\hat{\boldsymbol{r}}, t)$ can be inserted in Hamiltonian 2.17 as real functions which are related to the physical

fields through Maxwell equations,

$$\begin{aligned} \boldsymbol{B} &= \boldsymbol{\nabla} \times \boldsymbol{A} \\ \boldsymbol{E} &= -\boldsymbol{\nabla}\Phi - \frac{1}{c}\frac{\partial \boldsymbol{A}}{\partial t}. \end{aligned} \tag{2.18}$$

We thus write the Hamiltonian in the so-called *semi-classical approximation*: employing a classical electromagnetic field, while all other interaction terms are treated fully quantum-mechanically.

The Hamiltonian (2.17) is gauge–dependent, but physical observables are not [33]. If we choose Coulomb gauge, where

$$\begin{aligned} \boldsymbol{\nabla} \cdot \boldsymbol{A} &= 0 \\ \Phi(\hat{\boldsymbol{r}}, t) &= 0, \end{aligned} \tag{2.19}$$

the Hamiltonian for a single particle in the presence of an external electromagnetic field becomes,

$$\hat{\boldsymbol{H}} = \frac{\hat{\boldsymbol{p}}^2}{2m} + \frac{e}{mc}\hat{\boldsymbol{p}}\boldsymbol{A}(\hat{\boldsymbol{r}}, t) + \frac{e^2}{2mc^2}\boldsymbol{A}(\hat{\boldsymbol{r}}, t)^2, \tag{2.20}$$

where the first term corresponds to the kinetic energy of the particle and the rest to the interaction with electromagnetic field. The laser-molecule interaction term $\hat{\boldsymbol{H}}_{em}$ is:

$$\hat{\boldsymbol{H}}_{em} = \frac{e}{mc}\hat{\boldsymbol{p}}\boldsymbol{A}(\hat{\boldsymbol{r}}, t) + \frac{e^2}{2mc^2}\boldsymbol{A}(\hat{\boldsymbol{r}}, t)^2. \tag{2.21}$$

2.3.2 Dipole approximation

For a monochromatic electromagnetic wave, the vector potential $\boldsymbol{A}(\hat{\boldsymbol{r}}, t)$ may be written as

$$\boldsymbol{A}(\hat{\boldsymbol{r}}, t) = \boldsymbol{A}(t)\frac{1}{2}\exp\left(i\boldsymbol{k}\hat{\boldsymbol{r}}\right) + c.c.. \tag{2.22}$$

The *dipole approximation* implies that only the first term of the expansion of the above-exponential function is kept,

$$\boldsymbol{A}(\hat{\boldsymbol{r}}, t) = \boldsymbol{A}(t)\frac{1}{2}\left(1 + i\boldsymbol{k}\hat{\boldsymbol{r}} + ...\right) + c.c. \approx \boldsymbol{A}(t). \tag{2.23}$$

The dipole approximation is justified in the long-wavelength limit, where wavelength of the field is much larger than characteristic distance of the target, on which the photon absorption occurs.

Velocity gauge

By employing the dipole approximation to (2.21) we get the Hamiltonian of the electron-field interaction in the so-called *velocity gauge*

$$\hat{\boldsymbol{H}}^{v}_{em} = \frac{e}{mc}\hat{\boldsymbol{p}}\boldsymbol{A}(t) + \frac{e^2}{2mc^2}\boldsymbol{A}(t)^2, \tag{2.24}$$

where spatial dependence of the field has been eliminated. We insert the laser-matter interaction term in the time-dependent Schrödinger equation:

$$i\hbar\frac{\partial\left|\Psi_v\right\rangle}{\partial t} = \left(\hat{\boldsymbol{H}}_{kin} + \hat{\boldsymbol{H}}^{v}_{em}\right)\left|\Psi_v\right\rangle, \tag{2.25}$$

where $\hat{\boldsymbol{H}}_{kin}$ is field-free part of the Hamiltonian, the quadratic term $\boldsymbol{A}(t)^2$ can be removed, by including a global phase factor in the wave function, while leaving any physical observable intact. The phase factor is given by

$$\exp\left(\frac{ie^2}{2\hbar mc^2}\int_{-\infty}^{t}\boldsymbol{A}^2(t')dt',\right) \tag{2.26}$$

resulting in irrelevant overall phase, and thus can be neglected. Finally we have expression for the Hamiltonian of electron-field interaction in the dipole approximation in the velocity gauge:

$$\hat{\boldsymbol{H}}^{v}_{em} = \frac{e}{mc}\hat{\boldsymbol{p}}\boldsymbol{A}(t). \tag{2.27}$$

Length gauge

A new wave function $\left|\Psi_l\right\rangle$ can be defined by applying unitary Göppert-Mayer transformation to the wave function in the velocity gauge:

$$\left|\Psi_l\right\rangle = \hat{\boldsymbol{T}}\left|\Psi_v\right\rangle = \exp\left(+\frac{ie}{\hbar c}\boldsymbol{A}(t)\hat{\boldsymbol{r}}\right)\left|\Psi_v\right\rangle, \tag{2.28}$$

and its inverse,

$$\left|\Psi_v\right\rangle = \hat{\boldsymbol{T}}^{\dagger}\left|\Psi_l\right\rangle = \exp\left(-\frac{ie}{\hbar c}\boldsymbol{A}(t)\hat{\boldsymbol{r}}\right)\left|\Psi_l\right\rangle. \tag{2.29}$$

Substituting (2.29) into (2.25) gives:

$$i\hbar\frac{\left|\partial\Psi_l\right\rangle}{\partial t} = \left(\frac{\hat{\boldsymbol{p}}^2}{2m} + e\hat{\boldsymbol{r}}\boldsymbol{E}(t)\right)\left|\Psi_l\right\rangle, \tag{2.30}$$

from where we can see the final form of the Hamiltonian for the electron-field interaction in the dipole approximation in the length gauge

$$\hat{\boldsymbol{H}}^{l}_{em} = e\hat{\boldsymbol{r}}\boldsymbol{E}(t). \tag{2.31}$$

Although the electron-field interaction term has different form in length and velocity gauge, one can be obtained from another by applying unitary transformation and all physical observables are independent on choice of gauge. However, in practice, length and velocity gauge show different behavior as an unavoidable consequence of the computational implementation, and may lead to different numerical outcome, which depends on the choice of basis set. In particular, one observes a strong gauge dependencies with respect to the choice of the angular momentum basis sets, due to different discretization errors. In this way, the comparison between the results obtained using different gauges offers a good test of numerical convergence.

Having the expression for the *single* particle-field interaction, we can write the expression for n-particle system in length gauge:

$$\hat{\boldsymbol{H}}^{l}_{em} = \sum_{i=1}^{n} q_i \hat{\boldsymbol{r}}_i \boldsymbol{E}(t), \tag{2.32}$$

and in velocity gauge:

$$\hat{\boldsymbol{H}}^{v}_{em} = \sum_{i=1}^{n} \frac{q_i}{m_i} \hat{\boldsymbol{p}}_i \boldsymbol{A}(t), \tag{2.33}$$

where q_i and m_i are charge and mass of i^{th} particle, and $\hat{\boldsymbol{r}}_i$ and $\hat{\boldsymbol{p}}_i$ are its position and momentum operators. Since we are working in center-of-nuclear-mass frame, where $\boldsymbol{R_1} + \boldsymbol{R_2} = 0$ and $\boldsymbol{P}_1 + \boldsymbol{P}_2 = 0$, contributions of interactions of nuclei with electromagnetic radiation are canceled to zero, resulting only in contribution from electrons-field interactions:

$$\hat{\boldsymbol{H}}^{l}_{em} = e\boldsymbol{E}(t) \left(\hat{\boldsymbol{r}}_1 + \hat{\boldsymbol{r}}_2\right), \tag{2.34}$$

and in velocity gauge:

$$\hat{\boldsymbol{H}}^{v}_{em} = \frac{e}{m}\boldsymbol{A}(t) \left(\hat{\boldsymbol{p}}_1 + \hat{\boldsymbol{p}}_2\right). \tag{2.35}$$

We will frequently refer to the $\boldsymbol{\mu}_l = (\hat{\boldsymbol{r}}_1 + \hat{\boldsymbol{r}}_2)$ and $\boldsymbol{\mu}_v = (\hat{\boldsymbol{p}}_1 + \hat{\boldsymbol{p}}_2)$ as *dipole operators*.

2.4 Atomic units

Atomic units are particularly convenient, and they are defined by:

$$m = e = \hbar = 4\pi\epsilon_0 = 1. \tag{2.36}$$

We will use atomic units through the rest of this work. For improved readability, sometimes constants that are equal to one in atomic units will be shown explicitly, e.g. when giving the energy $\hbar\omega$ of a photon. The only constant that doesn't simplify to simple expression and will always be written, is speed of light $c = 1/\alpha \approx 137 a.u.$, where α is fine structure constant. The table 2.1 contains conversion factors for some more common quantities in atomic units.

Table 2.1 Conversion of atomic units

1 Atomic units of	symbol	Value in SI units
charge	e	$1.602176487(40) \cdot 10^{-19} C$
mass	m	$9.10938215(45) \cdot 10^{-31} kg$
length	a_0	$0.52917720859(36) \cdot 10^{-10} m$
energy	E_h	$4.35974394(22) \cdot 10^{-18} J(27.211385 eV)$
time	$\hbar/E_h$	$2.418884326505(16) \cdot 10^{-17} s$

The theory presented here is very general and independent on choice of coordinates or physical problem under consideration. In the following chapter, we provide a detail description of our numerical implementation. We have chosen a Finite Element Method combined with a Discrete Variable Representation for the spatial coordinates which is particularly suitable and efficient for the description of continuum states. Moreover, we will avoid the explicit computation of the final scattering states associated to the Coulomb breakup process by employing an Exterior Complex Scaling method, successfully employed in atoms in recent works and that allows to treat problems such as two electrons in the continuum or the description of adiabatic processes that are not accessible with other existing methods as those based on spectral representations of the molecular target.

Chapter 3

FEM-DVR and ECS method

The complete description of multiphoton ionization processes in H_2^+ and H_2 implies the solution of the three- and four-body break up problem quantum mechanically, for which there is no a general analytic solution and, consequently, has to be numerically solved for given set of boundary conditions. As shown in a large number of existing theoretical works [26, 75, 83], addressing the problem of molecular photoionization, even in the simplest molecules, presents a computational challenge reaching the limits of currently available computers. Therefore, it is mandatory to develop an efficient numerical methods to achieve this task and even offer the possibility of extension to a larger systems.

In our approach, we split both electronic and nuclear coordinates, in a radial and an angular part employing a single center expansion, which improves the implementation at the cost of the larger number of angular momenta used. All radial dependencies are treated in *finite element method - discrete variable representation (FEM-DVR)* [48], previously used in [83, 58], which shows many advantages and flexibility [49]. On top of radial FEM-DVR we use *exterior complex scaling transformation* (ECS) which implicitly imposes the correct boundary conditions without need for a large radial boxes.

This chapter describes in detail our numerical implementation to perform accurate ab initio calculations to address the half-collision problem of the full Coulomb breakup of H_2^+ and H_2 upon multiple photon absorption. Note that, in contrast to existing methodologies [46], we work beyond the Born-Oppenheimer approximation, thus accounting for all degrees of freedom including the non-adiabatic couplings. We show expressions for implementation of H_2 system beyond the BO approximation, but to the conclusion of this work we have performed calculations in fixed-nuclei approximation only.

3.1 Hydrogen molecular ion

The total Hamiltonian that represents an isolated one-electron homonuclear molecule is given in equation 2.4. We place the molecular axis in the z-axis, and one can restrict the problem to $J = 0$ in equation 3.1, i.e. we ignore the rotational motion of the nuclei. This is a valid approximation as long as we are considering molecular processes induced by ultrashort radiation sources, where rotational effects occur at much longer time scales and can thus be ignored in the present description. In this scenario, the nuclear kinetic energy term can be written as:

$$\frac{\hat{\boldsymbol{P}}_R^{\,2}}{2\mu_n} = \frac{1}{2\mu R^2}\frac{\partial}{\partial R}\left(R^2\frac{\partial}{\partial R}\right) + \frac{\hat{J}^2}{R^2}, \tag{3.1}$$

so we eliminate expansion in internuclear angular coordinates and reduce internuclear coordinate vector to one-dimensional variable, R. Only the electronic coordinate contains angular dependence, while we have radial dependence for both, electronic and internuclear coordinates. We look for a general (time-independent) solution in terms of a series expansion of wave function in spherical harmonics functions for electron coordinate ($Y_l^m(\hat{\boldsymbol{r}})$), and in basis functions expansion for both electronic ($\phi_i(r)$) and internuclear ($\chi_j(R)$) radial coordinates (which are going to be discussed later). In this way we reduce the problem of finding the wave function to the problem of finding expansion coefficients $a_{j,i,l,m}$. We write the wave function as

$$\Psi\left(R,\boldsymbol{r}\right) \equiv \frac{1}{R\cdot r}\sum_{j=1}^{j_{max}}\sum_{i=1}^{i_{max}}\sum_{l=1}^{l_{max}}\sum_{m=-l}^{l} a_{j,i,l,m}Y_l^m(\hat{\boldsymbol{r}})\chi_j(R)\phi_i(r), \tag{3.2}$$

where R and r are radial internuclear and electronic coordinate, $Y_l^m(\hat{\boldsymbol{r}})$ is spherical harmonics function that depends on electronic angular coordinates (θ,ϕ) determined by unit vector $\hat{\boldsymbol{r}}$, $\chi_j(R)$ and $\phi_i(r)$ are radial basis functions that will be specified latter and $a_{j,i,l}$ are unknown expansion coefficient.

In equation 3.2, the limit $j_{max} = i_{max} = l_{max} = \infty$ corresponds to the exact solution, however, any numerical implementation unavoidably requires the basis sets expansions to be limited to a finite value. The solution must then be checked to be converged with respect to the truncation parameters to a desired precision. Although in the following expressions, the summation limits are omitted, they are obviously assumed to be truncated to a given value.

For the H_2^+ system, the results shown in the present manuscript are obtained for linearly polarized light interacting with the molecule that can be parallel or

perpendicularly oriented. We always assume the system in its initial ground state (σ symmetry). The final form of expansion of wave function we are going to use is

$$\Psi\left(R,\boldsymbol{r}\right)\equiv\frac{1}{R\cdot r}\sum_{j,i,l}a_{j,i,l}Y_{l}^{0}(\hat{\boldsymbol{r}})\chi_{j}(R)\phi_{i}(r), \tag{3.3}$$

where expansion is restricted to σ symmetry.

3.2 Hydrogen molecule

Additional electron in the system means we need to include additional electronic coordinate.The two-electron molecular wave function is expanded as follows:

$$\begin{aligned}\Psi\left(R,\boldsymbol{r}_{1},\boldsymbol{r}_{2}\right)=&\frac{1}{R\cdot r_{1}r_{2}}\sum_{\substack{i_{1},l_{1},i_{2},l_{2}\\ j,L,M}}a_{\substack{i_{1},l_{1},i_{2},l_{2}\\ j,L,M}}\chi_{j}(R)\cdot\\ &Y_{l_{1}}^{m_{1}}(\hat{\boldsymbol{r}}_{1})\phi_{i_{1}}(r_{1})\cdot Y_{l_{2}}^{m_{2}}(\hat{\boldsymbol{r}}_{2})\phi_{i_{2}}(r_{2}),\end{aligned} \tag{3.4}$$

where R is radial internuclear coordinate, r_1 defines radial position of the 'first' and r_2 of the 'second' electron. $Y_l^m(\hat{\boldsymbol{r}}_k)$, where $k=(1,2)$, are spherical harmonics functions which depend on electronic angular coordinates (θ_k,ϕ_k) determined by unit vectors $\hat{\boldsymbol{r}}_k$, $\chi_j(R)$ and $\phi_i(r_k)$ are radial basis functions (to be specified latter) and $a_{\substack{i_1,l_1,i_2,l_2\\ j,L,M}}$ are the expansion coefficients.

Instead of using simple spherical harmonics (Y_{lm}) we choose to expand the wave function in series of *coupled* spherical harmonics functions (see Appendix B), $\mathcal{Y}_{l_1,l_2}^{L,M}$, which allows us to better exploit the symmetry of the system.

$$\begin{aligned}\Psi\left(R,\boldsymbol{r}_{1},\boldsymbol{r}_{2}\right)=&\frac{1}{R\cdot r_{1}r_{2}}\sum_{\substack{i_{1},l_{1},i_{2},l_{2}\\ j,L,M}}a_{\substack{i_{1},l_{1},i_{2},l_{2}\\ j,L,M}}\chi_{j}(R)\cdot\\ &\phi_{i_{1}}(r_{1})\phi_{i_{2}}(r_{2})\cdot\mathcal{Y}_{l_{1},l_{2}}^{L,M}(\hat{\boldsymbol{r}}_{1},\hat{\boldsymbol{r}}_{2})\end{aligned} \tag{3.5}$$

As mentioned in Sec. 2.2, we are considering system initially to be in the **singlet** state and the interaction with external fields considered in this work can not change its sate. Therefore, the total wave function has to be always symmetric with respect to exchange of electrons position coordinates

$$\Psi\left(R,\boldsymbol{r}_{1},\boldsymbol{r}_{2}\right)=\Psi\left(R,\boldsymbol{r}_{2},\boldsymbol{r}_{1}\right). \tag{3.6}$$

Rather than having the total wave function with symmetric and antisymmetric part, we impose symmetricity directly on basis functions in the expansion, reducing size of the problem:

$$\Psi\left(R,\boldsymbol{r}_1,\boldsymbol{r}_2\right)=\sum_{\substack{i_1,l_1,i_2,l_2\\j,L,M}} a_{\substack{i_1,l_1,i_2,l_2\\j,L,M}}\chi_j(R)\cdot\psi_{\substack{i_1,l_1,i_2,l_2\\L,M}}\left(\boldsymbol{r}_1,\boldsymbol{r}_2\right), \tag{3.7}$$

where we define *explicitly symmetric basis functions* ψ as:

$$\psi_{\substack{i_1,l_1,i_2,l_2\\L,M}}\left(\boldsymbol{r}_1,\boldsymbol{r}_2\right)\equiv A_{\substack{i_1,l_1,i_2,l_2\\L,M}}\left(\phi_{i_1}(r_1)\phi_{i_2}(r_2)\mathcal{Y}^{L,M}_{l_1,l_2}(\hat{\boldsymbol{r}}_1,\hat{\boldsymbol{r}}_2)+\phi_{i_1}(r_2)\phi_{i_2}(r_1)\mathcal{Y}^{L,M}_{l_1,l_2}(\hat{\boldsymbol{r}}_2,\hat{\boldsymbol{r}}_1),\right) \tag{3.8}$$

to be symmetric with respect to exchange of electronic coordinates ($\psi\left(\boldsymbol{r}_1,\boldsymbol{r}_2\right)=\psi\left(\boldsymbol{r}_2,\boldsymbol{r}_1\right)$), and where $A_{\substack{i_1,l_1,i_2,l_2\\L,M}}$ is normalization factor defined by

$$A_{\substack{i_1,l_1,i_2,l_2\\L,M}}\equiv\begin{cases}\frac{1}{2} & \text{if } i_1=i_2 \text{ and } l_1=l_2\\ \frac{1}{\sqrt{2}} & \text{otherwise}\end{cases}, \tag{3.9}$$

in order to have a basis normalized to 1.

To make notation more simple we use bra-ket notation, where in coordinate representation, coupled spherical harmonics functions have the following form,

$$\langle\Omega_1,\Omega_2|l_1,l_2,L,M\rangle=\mathcal{Y}^{L,M}_{l_1,l_2}(\hat{\boldsymbol{r}}_1,\hat{\boldsymbol{r}}_2), \tag{3.10}$$

where $\Omega_1=(\theta_1,\phi_1)$ and $\Omega_2=(\theta_2,\phi_2)$ are angles of vector $\hat{\boldsymbol{r}}_1$ and $\hat{\boldsymbol{r}}_2$ in spherical coordinate system. In the same way we define ket-state representing *radial* dependence for electrons,

$$\langle r_1,r_2|i_1,i_2\rangle=\phi_{i_1}(r_1)\phi_{i_2}(r_2), \tag{3.11}$$

and *radial* dependence for protons

$$\langle R|j\rangle=\chi_j(R). \tag{3.12}$$

Combining angular and radial part to the wave function, we can write the electronic state as a direct product:

$$|i_1,i_2;l_1,l_2,L,M\rangle\equiv|l_1,l_2,L,M\rangle\otimes|i_1,i_2\rangle, \tag{3.13}$$

and, equivalently, the complete electronic-nuclear state as:

$$|j; i_1, i_2; l_1, l_2, L, M\rangle \equiv |j\rangle \otimes |i_1, i_2; l_1, l_2, L, M\rangle \,. \tag{3.14}$$

Introducing the bra-ket notation in (3.8), we can write

$$|\Psi_{\substack{i_1,l_1,i_2,l_2\\L,M}}\rangle = A_{\substack{i_1,l_1,i_2,l_2\\L,M}} \left[|i_1, i_2; l_1, l_2, L, M\rangle + (-1)^{l_1+l_2-L} |i_2, i_1; l_2, l_1, L, M\rangle\right], \tag{3.15}$$

where we have used the property of the coupled spherical harmonics:

$$\mathcal{Y}^{L,M}_{l_1,l_2}(\hat{\boldsymbol{r}}_2, \hat{\boldsymbol{r}}_1) = (-1)^{l_1+l_2-L} \mathcal{Y}^{L,M}_{l_2,l_1}(\hat{\boldsymbol{r}}_1, \hat{\boldsymbol{r}}_2). \tag{3.16}$$

Finally, we write the total molecular wave function as

$$|\Psi\left(R, \boldsymbol{r}_1, \boldsymbol{r}_2\right)\rangle = \sum_{\substack{i_1,l_1,i_2,l_2\\j,L,M}} a_{\substack{i_1,l_1,i_2,l_2\\j,L,M}} |\chi_j(R)\rangle \otimes |\psi_{\substack{i_1,l_1,i_2,l_2\\L,M}}\left(\boldsymbol{r}_1, \boldsymbol{r}_2\right)\rangle \tag{3.17}$$

In referring to the *fixed nuclei approximation*, which we will use with analysis purposes in the present work, we will assume that protons are fixed in space and we omit nuclear coordinate and j-index in expansion, writing:

$$|\Psi\left(\boldsymbol{r}_1, \boldsymbol{r}_2\right)\rangle = \sum_{\substack{i_1,l_1,i_2,l_2\\L,M}} a_{\substack{i_1,l_1,i_2,l_2\\L,M}} |\psi_{\substack{i_1,l_1,i_2,l_2\\L,M}}\left(\boldsymbol{r}_1, \boldsymbol{r}_2\right)\rangle \,. \tag{3.18}$$

In symmetrisation of the basis set, we removed anti-symmetric basis functions while keeping the size of our basis the same, consequently we introduced a linear dependencies between basis elements. Linearly dependent elements, equal up to a sign coming from $(-1)^{l_1+l_2+L}$ factor, we eliminate by limiting summation to $i_1 > i_2 \vee (i_1 = i_2 \wedge l_1 \geq l_2)$. In the following, unless otherwise stated, this condition is always implied in the $\sum_{\substack{i_1,l_1,i_2,l_2\\j,L,M}}$ and $\sum_{\substack{i_1,l_1,i_2,l_2\\L,M}}$.

3.3 Radial basis functions

The radial basis functions associated to the nuclear motion, $\chi_j(R)$, and to the electronic motion, $\phi_i(r)$, can be chosen from any complete set of square-integrable functions, i.e. L_2 space. In this work we use *finite element method - discrete variable representation (FEM-DVR)* functions for both, nuclear and electron basis function.

The FEM-DVR functions has become popular, [68] in computational chemistry, because of many advantages and flexibility of their use. The DVR functions connects analytic basis functions methods that discretize the wave function in space of square integrable functions, and numerical grid methods that discretize the wave function in coordinate space. The main advantage the DVR is that the potential matrix elements are diagonal and easily evaluated at the grid points, while the matrix elements of the kinetic energy operator have simple analytic expression. The DVR keeps many of the properties of finite difference methods, eliminating need to evaluate numerical derivatives of the function. In DVR the kinetic-energy matrix is generally full, leading to the larger bandwidth of the linear equations compared to finite difference methods. Merging attractive properties the *finite-element method* FEM and DVR: the sparse structure of matrices in FEM and the diagonal structure of the potential energy matrix in the DVR, allows one to combine them into a single powerful method.

An important difficulty in collision problems is the treatment of asymptotic boundary conditions, particularly complicated in collisions that involve three-body (or more) breakup where energy can be arbitrarily shared between the outgoing fragments, making implementation of the boundary conditions challenging. It has been shown [47] that the imposition of asymptotic boundary conditions can be avoided by utilizing an *exterior complex scaling transformation ECS* in the equation that describes the outgoing portion (scattered wave) of the continuum wave function. The scattered wave attenuates exponentially under such a transformation, like the regular wave function for a bound state.

We introduce free parameter R_0, which specify interaction region of the hyperspace, within which the solution of the transformed Schrödinger equation corresponds to the real solution of the physical problem under consideration and decreases exponentially outside of it. The dynamics of a physical process can be completely extracted from the interaction region where the coordinates are real (while exterior region has no direct physical meaning).

This method has been implemented for electron-hydrogen scattering [47] and photon-helium atom single and double ionization problem [60] and our aim is to apply it to the systems involving both electron-electron and electron-nucleon interaction and explore (still unsolved) Coulomb-explosion and dissociation channel in hydrogen molecule.

3.4 Finite element discrete variable representation

In the finite-elements method, the wave function is not expanded in terms of *global* basis functions. Rather, the real interval of interest $[0, R_{max}]$ is divided into a sub-intervals by a grid of N nodes $0 \leq r_1 < r_2 < ... < r_N = R_{max}$ (not necessarily equidistant), each sub-interval is further subdivided by n nodes. We define N as the number of finite elements and n as the DVR order. The grid of points created in this way are used to construct a set of linearly independent basis functions, which satisfy some useful properties as we discuss next.

We start by defining, *elementary finite-element basis functions* $f_{i,m}(r)$ that are defined to be identically zero outside a given interval (which we call DVR element)

$$f_{i,m}(r) = 0, r \notin [r_i, r_{i+1}], i = 1, ..., N, m = 1, ..., n. \tag{3.19}$$

We will assume that the function $f_{i,m}(r)$ has a well-defined value at each grid point, more specifically:

$$\begin{aligned} &f_{i,1}(r_i) = 1, \\ &f_{i,n}(r_{i+1}) = 1, \\ &f_{i,m}(r_i) = f_{i,m}(r_{i+1}) = 0, otherwise. \end{aligned} \tag{3.20}$$

The discrete variable representation uses a discretization procedure that associates one basis function to each grid point. This is realized by constructing a polynomial basis that is associated to a Gauss quadrature rule which is in turn associated to Gauss quadrature points. Therefore, each DVR element is subdivided by Gauss quadrature points. Because this quadrature excludes the end points in each interval, we will use instead the so-called Gauss-Lobatto quadrature where the end points are included. Accordingly each DVR element is subdivided by set of Gauss-Lobatto $x_m^i, m = 1, ..., n$ quadrature points and the corresponding quadrature weights are defined.

In Gauss-Lobatto quadrature, integral of a function $g(x)$ is evaluated by knowing values of the function in x_i point by the following formula

$$\int_{-1}^{1} g(x)dx \cong \sum_{m=1}^{n} g(x_m)w_m. \tag{3.21}$$

The points (x_i) and weights (w_i) are chosen to make 3.21 exact when $g(x)$ is polynomial of degree $\leq 2n + 1$. We scale x argument to be able to apply 3.21 to an arbitrary

interval

$$\int_{r_i}^{r_{i+1}} g(x)dx \cong \sum_{m=1}^{n} g(x_m^i)w_m^i, \tag{3.22}$$

where

$$w_m^i = \frac{r_{i+1} - r_i}{2} w_m, \tag{3.23}$$

$$x_m^i = \frac{1}{2}\left[(r_{i+1} + r_i)x_m + (r_{i+1} - r_i)\right] \tag{3.24}$$

In Gauss-Lobatto quadrature [39], two of the points are constrained to coincide with the endpoints, $x_1^i = r_i$ and $x_n^i = r_{i+1}$. The weights and remaining points are chosen to make 3.22 exact for polynomials of degree $\leq 2n-1$:

$$\int_{r_i}^{r_{i+1}} g(x)dx \cong g(r_i)w_1^i + \sum_{m=2}^{n-1} g(x_m^i)w_m^i + g(r_{i+1})w_n^i. \tag{3.25}$$

To construct a DVR based on Gauss-Lobatto quadrature, we choose the elementary basis functions to be Lagrange interpolating polynomials (or, as called in [44], Lobatto shape functions):

$$f_{i,m}(x) \equiv \begin{cases} \prod_{j\neq m} \frac{x - x_j^i}{x_m^i - x_j^i}, & r_i \leq x \leq r_{i+1} \\ 0, & \text{otherwise.} \end{cases} \tag{3.26}$$

The Lobatto shape functions have useful property

$$f_{i,m}(x_{m'}^{i'}) = \delta_{i,i'}\delta_{m,m'}. \tag{3.27}$$

Using this quadrature to approximate the computation of all required integrals, one can see that the functions are indeed orthogonal through the Gauss-Lobatto quadrature:

$$\begin{aligned} \int_0^\infty f_{i,m}(x)f_{i',m'}(x)dx &= \delta_{i,i'} \int_{r_i}^{r_{i+1}} f_{i,m}(x)f_{i,m'}(x)dx \\ &\cong \delta_{i,i'} \sum_{j=1}^{n} f_{i,m}(x_j^i)f_{i,m'}(x_j^i)w_j^i \\ &= \delta_{i,i'}\delta_{j,j'}w_j^i \end{aligned} \tag{3.28}$$

and, consequently, any local operator ($V(x)$) obtained in the FEM-DVR basis leads to a diagonal representation:

$$\int_0^\infty f_{i,m}(x)V(x)f_{i',m'}(x)dx \cong \delta_{i,i'}\delta_{j,j'}V(x_m^i)w_j^i. \tag{3.29}$$

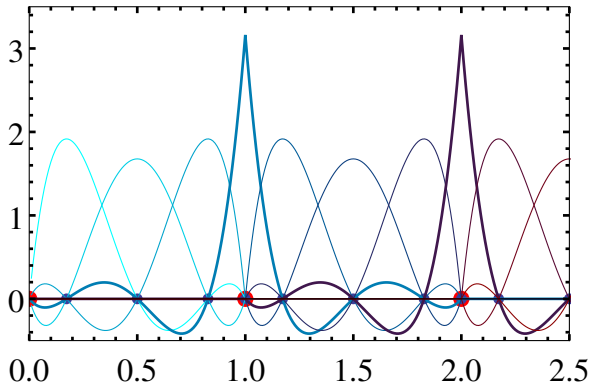

Fig. 3.1 FEM-DVR basis functions example for DVR order $n = 3$. Red dots: FEM boundaries, blue dots: Gauss-Lobatto quadrature points, lines represent basis functions, "bridge" functions are plotted with bold line.

This is one of the main advantages of the FEM-DVR basis sets, since the matrix representation of the Hamiltonian, yields diagonal terms in the spatial coordinates for every potential interaction term, which largely simplifies large-scale numerical implementations.

To ensure continuity of the wave function at the interval boundaries, we combine the two Lobatto shape functions $f_{i,n}$ and $f_{i+1,1}$, which are both unity at r_{i+1}, into a single "bridge" function that we here denote as χ_{i1} that connects two neighboring elements.

$$\chi_{i1}(x) = f_{i,n}(x) + f_{i+1,1}(x) \tag{3.30}$$

$$\chi_{im}(x) = f_{i,m}(x), \qquad m = 2, ..., n-1. \tag{3.31}$$

The above-defined basis functions are thus orthogonal, but they are not normalized. Therefore, in order to have a set of orthonormalized functions we should apply the re-normalization procedure defined as:

$$\chi_{i1}(x) = \frac{f_{i,n}(x) + f_{i+1,1}(x)}{\sqrt{w_n^i + w_n^{i+1}}} \tag{3.32}$$

$$\chi_{im}(x) = \frac{f_{i,m}(x)}{\sqrt{w_m^i}}, \qquad m = 2, ..., n-1, \tag{3.33}$$

which is the final form of the FEM-DVR basis functions that we are going to use for radial dependence, as shown in Fig. 3.1.

A wave function that is expanded in terms of basis functions defined in Eq. 3.32 and 3.33 will be continuous across the borders of finite element, but might have discontinuous derivatives and potentially infinite second derivative. Fortunately, it has been shown that it is possible to correctly express the second derivative, which define kinetic energy operator, in FEM-DVR basis set [71]. The general 1D (radial) function, with discontinues derivative at the FEM boundary x_0, can be written as sum of two continuous functions $f(x)$ and $g(x)$:

$$\frac{d\phi(x)}{dx} = f(x)\theta(x - x_0) + g(x)\theta(x_0 - x), \tag{3.34}$$

where θ is Heaviside step function, defined as:

$$\theta(x) \equiv \begin{cases} 0 & x < 0 \\ 1 & x > 0. \end{cases} \tag{3.35}$$

The second derivative of such a function is obtained from 3.34 as:

$$\frac{d^2\phi(x)}{dx^2} = f'(x)\theta(x - x_0) + g'(x)\theta(x_0 - x) + (f(x) - g(x))\delta(x - x_0). \tag{3.36}$$

We expand $\phi(x)$ in FEM-DVR basis as

$$\phi(x) = \sum_{i,m} c_{i,m}\chi_{i,m}(x), \tag{3.37}$$

and by inserting it in 3.36 the expectation value of the (radial) kinetic energy ($T = -\frac{1}{2}\frac{d^2}{dx^2}$) can be expressed as [68]:

$$\begin{aligned} \langle\phi(x)|T|\phi(x)\rangle = -\frac{1}{2}\int_0^\infty \phi(x)\frac{d^2}{x^2}\phi(x)\,dx = \\ -\frac{1}{2}\lim_{\epsilon\to 0}\sum_i \int_{r_i+\epsilon}^{r_{i+1}-\epsilon} \phi(x)\sum_m c_{i,m}\frac{d^2}{dx^2}\chi_{i,m}(x)\,dx \\ -\frac{1}{2}\int_0^\infty dx\,\phi(x)\sum_{i,m} c_{i,m}\delta(x - r_i)\left[\frac{d}{dx}\chi_{i,m}(r_i + 0) - \frac{d}{dx}\chi_{i,m}(r_i - 0)\right] \\ = \frac{1}{2}\sum_i \int_{r_i}^{r_{i+1}} dx\,\left(\frac{d}{dx}\phi(x)\right)^2 \end{aligned} \tag{3.38}$$

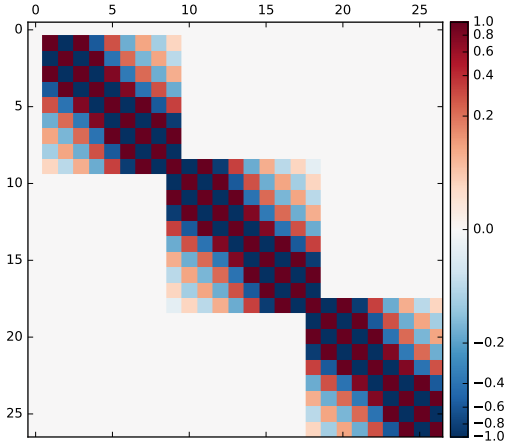

Fig. 3.2 FEM-DVR sparse kinetic-energy matrix, normalized to 1. DVR order $n = 10$, number of finite-elements $N = 3$. Each index of matrix element corresponds to the one FEM-DVR grid point.

where we used partial integration in which δ function terms cancel the surface terms that. Thus the kinetic-energy matrix elements in a FEM-DVR are evaluated as

$$T^{i,i'}_{m,m'} = \frac{1}{2}\left(\delta_{i,i'} + \delta_{i,i'\pm 1}\right) \int_0^\infty dx \frac{d}{dx}\chi_{i,m}(x)\frac{d}{dx}\chi_{i',m'}(x) \tag{3.39}$$

Although, matrix elements of the kinetic-energy operator are not diagonal in the DVR, they are given by simple analytic formulas when evaluated by using the Gauss quadrature rule. The required elements are simply evaluated in terms of the first derivatives of the Lobatto shape functions at the quadrature points, which are given by [44]

$$\frac{d}{dx} f_{i,m}(x^i_{m'}) = \begin{cases} \frac{1}{x^i_m - x^i_{m'}} \prod_{k\neq m,m'} \frac{x^i_{m'} - x^i_k}{x^i_m - x^i_k}, & m \neq m' \\ \frac{1}{2w^i_m}\left(\delta_{m,n} - \delta_{m,1}\right), & m = m'. \end{cases} \tag{3.40}$$

The matrix representation of the 1D kinetic energy term and its sparse structure is shown on example in figure 3.2, where we can see diagonal blocks corresponding to the finite-elements. Two consecutive blocks have one common row, coming from "bridge" function that they share. The sparse nature of the kinetic energy matrix enables significant reduction of required computational resources.

In the rest of this work indices i and m of FEM-DVR basis functions are "combined" into one index (usually called i for radial dependence of electrons and j for radial dependence of nuclei) which correspond to FEM-DVR grid point.

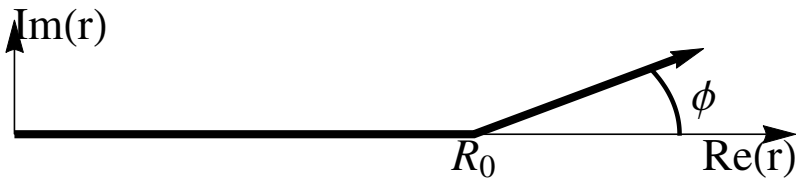

Fig. 3.3 Exterior complex scaling scheme.

3.5 Exterior complex scaling

Solving the photoabsorption half-collision problem involves applying the correct boundary conditions. However, they involve a complicated asymptotic form of the exact solution of the three-body Coulomb breakup problem [2, 35] (for four-body problem not known), which has proved to be extremely difficult to apply explicitly in a numerical calculations. The method of exterior complex scaling (ECS) was developed specifically to avoid this difficulty of explicit imposition of boundary conditions by implicit imposition of a pure outgoing-wave boundary conditions by a means of coordinate transformation. ECS enforces the outgoing-wave boundary conditions on scattering wave functions by extending a real coordinates further in a complex plane while keeping physical observable intact.

Exterior complex scaling is type of coordinates transformation [76] $r \mapsto R(r)$,

$$R(r) = \begin{cases} r, & r < R_0 \\ R_0 + (r - R_0)e^{i\phi}, & r \geq R_0, \end{cases} \tag{3.41}$$

where the real coordinate is at some point R_0 rotated into complex plane by an angle ϕ, (Fig. 3.3). Under this transformation, any function F that behaves like a pure outgoing wave at large distances,i.e.,

$$F(r) \sim Ae^{ikr}, \qquad r \to \infty. \tag{3.42}$$

will decrease exponentially. ECS can therefore be used in quantum-scattering applications to avoid explicit enforcement of asymptotic boundary conditions by applying the transformation to the equation that determines the outgoing part of the full wave function.

The ECS transformation is applied to the finite element boundaries $[r_i]$, ensuring that the exterior scaling radius R_0 coincides with one of the nodes, r_i. This defines a segmented contour of points that are real out to R_0 and then fall on a complex ray.

The DVR quadrature points and weights can then be determined for each segment of the contour; the points and weights belonging to elements $i > I$ will of course be complex:

$$\chi_{i1}(x) = \frac{f_{i,n}(R(x)) + f_{i+1,1}(R(x))}{\sqrt{e^{i\phi}(w_n^i + w_n^{i+1})}} \qquad i > I, \tag{3.43}$$

$$\chi_{im}(x) = \frac{f_{i,m}(R(x))}{\sqrt{e^{i\phi}w_m^i}}, \qquad m = 2, ..., n-1, i \geq I, m \neq 1. \tag{3.44}$$

In particular, the complex bridge function centered at $R_0 = R_I$,

$$\chi_{I1}(x) = \frac{f_{I,n}(R(x)) + f_{I+1,1}(R(x))}{\sqrt{w_n^I + e^{i\phi}w_n^{I+1}}} \tag{3.45}$$

guarantees continuity of the scattered wave at the exterior scaling radius.

3.6 Boundary conditions

The numerical representation of the photoionization event requires the implementation of the boundary conditions that defines a half-collision problem. We are thus considering a collision problem where the flux of incoming particles is associated to photon-absorption and the outgoing flux is given by the breakup fragments. Within the dipole approximation and assuming a classical representation of the electromagnetic field, the light is thus uniform through space, avoiding the imposition of specific boundary conditions for incoming particles and reducing the problem to a *half-collision* problem.

In general, we are solving equations in *reduced* coordinates, where $\Psi(r) = ru(r)$ and where $u(r)$ has finite value at $r = 0$. Therefore it is necessary to fulfill

$$\Psi(r = 0) = 0. \tag{3.46}$$

This is easily imposed by omitting the only basis function that has nonzero value in $r = 0$, i.e. $f_{1,1}$.

The second boundary condition comes from the fact that in the asymptotic region $r \to \infty$ should have the form of outgoing wave.

$$\Psi(r \to \infty) \sim Ae^{ikr}. \tag{3.47}$$

Under ECS transformation, any solution with behavior of outgoing wave will be exponential attenuated in ECS region. By making sure that size of ECS region is large enough, this boundary condition is effectively transformed in requirement that solution of the problem is zero at the end of ECS region. In practice this condition is easily incorporated by omitting the only basis function with nonzero value at the end of ECS region, i.e. $f_{N,n}$.

3.7 Matrix elements

In this section we provide the expressions for each term of the molecular Hamiltonians, equations 2.4 and 2.8, in above-described basis sets, i.e. with a single-center angular momentum expansion combined with the FEM-DVR for the radial part of the wave function.

The two-electron wave function for the hydrogen molecule is expanded in coupled spherical harmonics with a explicitly symetrized basis. (defined by equation 3.15):

$$|\underset{L,M}{\Psi_{i_1,l_1,i_2,l_2}}\rangle_s = \underset{L,M}{A_{i_1,l_1,i_2,l_2}} \left[|i_1,i_2;l_1,l_2,L,M\rangle + (-1)^{l_1+l_2-L}\,|i_2,i_1;l_2,l_1,L,M\rangle\right], \quad (3.48)$$

where subscript $_s$ indicates symmetrized basis. To evaluate matrix elements of any general operator ($\hat{\boldsymbol{O}}$) we should compute:

$$\begin{aligned}
{}_s\langle\underset{L',M'}{\Psi_{i_1',l_1',i_2',l_2'}}|\hat{\boldsymbol{O}}|\underset{L,M}{\Psi_{i_1,l_1,i_2,l_2}}\rangle_s = \\
&\langle i_1',i_2';l_1',l_2',L',M'|\hat{\boldsymbol{O}}|i_1,i_2;l_1,l_2,L,M\rangle + \\
&\langle i_1',i_2';l_1',l_2',L',M'|\hat{\boldsymbol{O}}|i_2,i_1;l_2,l_1,L,M\rangle\,(-1)^{l_1+l_2-L} + \\
&\langle i_2',i_1';l_2',l_1',L',M'|\hat{\boldsymbol{O}}|i_1,i_2;l_1,l_2,L,M\rangle\,(-1)^{l_1'+l_2'-L'} + \\
&\langle i_2',i_1';l_2',l_1',L',M'|\hat{\boldsymbol{O}}|i_2,i_1;l_1,l_2,L,M\rangle\,(-1)^{l_1+l_2-L+l_1'+l_2'-L'},
\end{aligned} \quad (3.49)$$

where i_1 and i_2 are indices of basis functions describing radial coordinates of 'first' and 'second' electron respectively, indices l_1, l_2, L and M are indices of coupled harmonics, describing angular dependence of electronic coordinates. We will derive the general form of the first term ($\langle i_1',i_2';l_1',l_2',L',M'|\hat{\boldsymbol{O}}|i_1,i_2;l_1,l_2,L,M\rangle$) of an operator in this basis and all the other therms can be obtained simply by permuting indices, as in equation 3.49. The coupled basis is related with uncoupled by B.4 or B.5, therefore we will show expressions in uncoupled basis. We can see that terms 'first' and 'second'

electron loses its meaning, since the matrix elements, as well as the wave function, are indifferent with respect to exchange of electronic coordinates.

3.7.1 Kinetic energy

The kinetic energy operator, either for electrons or nuclei ($\hat{\boldsymbol{P}}$, $\hat{\boldsymbol{p}}_1$ and $\hat{\boldsymbol{p}}_2$), is a single particle operator. Therefore, it can be independently obtained for the different electronic and nuclear coordinates defined by different FEM-DVR basis. The kinetic energy operator, ∇^2, can be explicitly written as:

$$\nabla^2 = \frac{1}{r^2}\frac{\partial}{\partial r}\left(r^2\frac{\partial}{\partial r}\right) + \frac{\hat{l}^2}{r^2}. \tag{3.50}$$

Acting on a single electron wave function (in reduced coordinates $\Psi(r) \to r\Psi(r)$), we get

$$\begin{aligned}\nabla^2 |r,l,m\rangle &= \left(\frac{d^2}{dr^2} - \frac{\hat{l}^2}{r^2}\right)|r,l,m\rangle \\ &= \left(\frac{d^2}{dr^2} - \frac{l(l+1)}{r^2}\right)|r,l,m\rangle\,.\end{aligned} \tag{3.51}$$

The matrix form of the operator written in the FEM-DVR basis set thus gives:

$$\begin{aligned}\langle i',l',m'|\nabla^2|i,l,m\rangle &= \langle i',l',m'|\frac{d^2}{dr^2} - \frac{l(l+1)}{r^2}|i,l,m\rangle \\ &= \delta_{l',l}\delta_{m',m}\left(T_{i',i} + \delta_{i',i}\frac{l(l+1)}{{r_i}^2}\right),\end{aligned} \tag{3.52}$$

where we obtain a Kronecker-δ function in the angular components, thus leads to a diagonal representation in the angular components, while it has a non-diagonal structure in the FEM-DVR points, as illustrated in the figure 3.2. The evaluation of the radial ($T_{i',i}$) matrix elements is given by equations 3.39 and 3.40 (here we use singe index i to represent both i and m). As already explained, the evaluation of the local operators ($1/r$) are pure diagonal in the FEM-DVR basis (equation 3.29).

While the evaluation of the electronic kinetic energy operator leads to the block-diagonal structure (is proportional to $\delta_{l',l}$), the nuclear counterpart is restricted to the $J = 0$ term, i.e., we neglect the rotational effects for the nuclei, which further simplifies the kinetic energy term for the nuclei. In the one-electron molecular target, H_2^+, this

term becomes:

$$K^{H_2^+,nuc}_{\substack{j',i',l',m'\\ j,i,l,m}} \equiv -\frac{1}{2\mu_n}\langle j',i',l',m'|\nabla^2|j,i,l,m\rangle = -\frac{1}{2\mu_n}\delta_{i,i'}\delta_{l,l'}\delta_{m,m'}T^{nuc}_{j',j}. \tag{3.53}$$

As we will see later, it is not necessary to use the *same FEM-DVR basis* for electronic and nuclear coordinates, therefore we indicated that second derivative $T^{nuc}_{j',j}$ operator is evaluated in *inter-nuclear* FEM-DVR basis. For the two-electron diatomic molecule, H_2, we obtain an equivalent expression:

$$\begin{aligned} K^{H_2,nuc}_{\substack{j',i'_1,l'_1,m'_1,i'_2,l'_2,m'_2\\ j,i_1,l_1,m_1,i_2,l_2,m_2}} &= -\frac{1}{2\mu_n}\langle j',i'_1,l'_1,m'_1,i'_2,l'_2,m'_2|\nabla^2|j,i_1,l_1,m_1,i_2,l_2,m_2\rangle \\ &= -\frac{1}{2\mu_n}\delta_{i_1,i'_1}\delta_{l_1,l'_1}\delta_{m_1,m'_1}\delta_{i_2,i'_2}\delta_{l_2,l'_2}\delta_{m_2,m'_2}T^{nuc}_{j',j}, \end{aligned} \tag{3.54}$$

where we explicitly include the indices corresponding to both electrons.

3.7.2 Electronic repulsion

The electron-electron $1/|\boldsymbol{r}_2-\boldsymbol{r}_1|$ and electron-nuclei interaction terms $(1/|\boldsymbol{r}_i-\boldsymbol{R}|)$ prevents the separability of the Hamiltonian in electronic and nuclear degrees of freedom. For the evaluation of the electron-electron repulsion and electron-nuclei attraction terms we employ the same approach. The electronic repulsion term,

$$U_{\substack{j',i'_1,l'_1,m'_1,i'_2,l'_2,m'_2\\ j,i_1,l_1,m_1,i_2,l_2,m_2}} = \langle j',i'_1,l'_1,m'_1,i'_2,l'_2,m'_2|\frac{1}{|\boldsymbol{r}_2-\boldsymbol{r}_1|}|j,i_1,l_1,m_1,i_2,l_2,m_2\rangle \tag{3.55}$$

is evaluated in the FEM-DVR basis. As it is well known, the inverse of the distance between electrons, $1/|\boldsymbol{r}_2-\boldsymbol{r}_1|$ can be expressed [33] as expansion in spherical harmonics:

$$\frac{1}{|\boldsymbol{r}_2-\boldsymbol{r}_1|} = 4\pi\sum_{\lambda=0}^{\infty}\sum_{\mu=-\lambda}^{\lambda}\frac{1}{2\lambda+1}\frac{r_<^\lambda}{r_>^{\lambda+1}}Y^*_{\lambda\mu}(\hat{\boldsymbol{r}}_1)Y_{\lambda\mu}(\hat{\boldsymbol{r}}_2), \tag{3.56}$$

where $r_>$ is greater one (and $r_<$ smaller) of r_1 and r_2:

$$\begin{aligned} r_> &\equiv \max(r_1,r_2) \\ r_< &\equiv \min(r_1,r_2). \end{aligned} \tag{3.57}$$

Which allows us to write the resulting matrix elements in separated products of the angular and the spatial components:

$$\begin{aligned} U^{j',i'_1,l'_1,m'_1,i'_2,l'_2,m'_2}_{j,i_1,l_1,m_1,i_2,l_2,m_2} =& \delta_{j,j'} \sum_{\lambda=0}^{\infty} \sum_{\mu=-\lambda}^{\lambda} \frac{4\pi}{2\lambda+1} I^{(\lambda)}_{i'_1,i'_2,i_1,i_2} \\ & \cdot \langle l'_1, m'_1, l'_2, m'_2 | Y^*_{\lambda\mu}(\hat{\boldsymbol{r}}_1) Y_{\lambda\mu}(\hat{\boldsymbol{r}}_2) | l_1, m_1, l_2, m_2 \rangle \,, \end{aligned} \tag{3.58}$$

where $I^{(\lambda)}_{i'_1,i'_2,i_1,i_2}$ is radial integral

$$I^{(\lambda)}_{i'_1,i'_2,i_1,i_2} = \langle i'_1, i'_2 | \frac{r^{\lambda}_{<}}{r^{\lambda+1}_{>}} | i_1, i_2 \rangle \,. \tag{3.59}$$

The angular integrals can be we written explicitly as

$$\begin{aligned} & \langle l'_1, m'_1, l'_2, m'_2 | Y^{*\mu}_{\lambda}(\hat{\boldsymbol{r}}_1) Y^{\mu}_{\lambda}(\hat{\boldsymbol{r}}_2) | l_1, m_1, l_2, m_2 \rangle \\ & = (-1)^{\mu} \left\langle l'_1 m'_1 | Y^{-\mu}_{\lambda}(\hat{\boldsymbol{r}}_1) | l'_1 m'_1 \right\rangle \langle l_2 m_2 | Y^{\mu}_{\lambda}(\hat{\boldsymbol{r}}_2) | l_2 m_2 \rangle \\ & = (-1)^{\mu} \times \\ & (-1)^{m'_1} \sqrt{\frac{(2l_1+1)(2\lambda+1)(2l'_1+1)}{4\pi}} \begin{pmatrix} l'_1 & \lambda & l_1 \\ -m'_1 & -\mu & m_1 \end{pmatrix} \begin{pmatrix} l'_1 & \lambda & l_1 \\ 0 & 0 & 0 \end{pmatrix} \\ & (-1)^{m'_2} \sqrt{\frac{(2l_2+1)(2\lambda+1)(2l'_2+1)}{4\pi}} \begin{pmatrix} l'_2 & \lambda & l_2 \\ -m'_2 & \mu & m_2 \end{pmatrix} \begin{pmatrix} l'_2 & \lambda & l_2 \\ 0 & 0 & 0 \end{pmatrix}, \end{aligned} \tag{3.60}$$

where $\begin{pmatrix} l_1 & l_2 & l_3 \\ m_1 & m_2 & m_3 \end{pmatrix}$ is Wigner 3j-symbol, described in Appendix B.

The radial integral is evaluated in the finite region of space where the basis sets is defined, in the interval $[0, r_{max}]$ as:

$$\begin{aligned} I^{(\lambda)}_{i'_1,i'_2,i_1,i_2} &= \langle \chi_{i'_1}(r_1) \chi_{i'_2}(r_2) | \frac{r^{\lambda}_{<}}{r^{\lambda+1}_{>}} | \chi_{i_1}(r_1) \chi_{i_2}(r_2) \rangle \\ &= \int_0^{r_{max}} \int_0^{r_{max}} \chi_{i'_1}(r_1) \chi_{i'_2}(r_2) \frac{r^{\lambda}_{<}}{r^{\lambda+1}_{>}} \chi_{i_1}(r_1) \chi_{i_2}(r_2) \, dr_1 \, dr_2, \end{aligned} \tag{3.61}$$

where $\chi_{i_1}(r_1)$ and $\chi_{i_2}(r_2)$ are FEM-DVR basis functions describing motion of the 'first' and 'second' electron respectively. This is the exact same expression as the one employed for a two-electron atomic target [49].

Gauss–Lobatto quadrature is not compelling for the integrations in equation 3.61, as it effectively expands the derivative discontinuity in the potential $\frac{r^{\lambda}_{<}}{r^{\lambda+1}_{>}}$ in a polynomial

(FEM-DVR) basis. Therefore replacing this potential with its values at the grid points is a poor approximation to the integral. However we can restore the effectiveness of the Gauss quadrature if instead we apply the FEM-DVR to solving Poisson's equation for the potential due to the charge distribution corresponding to a product of two of the FEM-DVR basis functions [49].

To make notation cleaner, we will define ρ_A and ρ_B as

$$\begin{aligned} \rho_A(r_1) &\equiv \chi_{i_1'}(r_1)\chi_{i_1}(r_1) \\ \rho_B(r_2) &\equiv \chi_{i_2'}(r_2)\chi_{i_2}(r_2). \end{aligned} \tag{3.62}$$

We define the function $y^{(\lambda)}(r)$ as

$$\begin{aligned} y^{(\lambda)}_{i_1',i_1}(r) \equiv & r\int_0^{r_{max}} dr' \rho_A(r') \frac{r_<^\lambda}{r_>^{\lambda+1}} \\ = & \int_0^r \rho_A(t) \left(\frac{t}{r}\right)^\lambda dt + \int_r^{r_{max}} \rho_A(t) \left(\frac{r}{t}\right)^{\lambda+1} dt, \end{aligned} \tag{3.63}$$

so that the original integral 3.61 can be written as one-dimensional integral:

$$I^{(\lambda)}_{i_1',i_2',i_1,i_2} = \int_0^{r_{max}} \rho_B(r) \frac{y^{(\lambda)}_{i_1',i_1}(r)}{r} dr \tag{3.64}$$

By taking the second derivative of 3.63, we show that $y^{(\lambda)}_{i_1',i_1}(r)$ satisfies the radial form of Poisson's equation [49],

$$\left(\frac{d^2}{dr^2} - \frac{\lambda(\lambda+1)}{r^2}\right) y^{(\lambda)}_{i_1',i_1}(r) = -\frac{2\lambda+1}{r}\rho_A(r). \tag{3.65}$$

From definition of $y^{(\lambda)}_{i_1',i_1}(r)$ we have the boundary conditions

$$y^{(\lambda)}(r=0) = 0 \tag{3.66a}$$

$$\begin{aligned} y^{(\lambda)}_{i_1',i_1}(r_{max}) = & \int_0^{r_{max}} \rho_A(t) \left(\frac{t}{r_{max}}\right)^\lambda dt \\ = & \delta_{i_1',i_1} \frac{r_{i_1}^\lambda}{r_{max}^\lambda}. \end{aligned} \tag{3.66b}$$

The last equation is evaluated in FEM-DVR basis. In order to solve differential equation 3.65, we expand (homogeneous) solution $y^{(\lambda)}_{i'_1,i_1}(r)$ in the *same* FEM-DVR basis,

$$y^{(\lambda,H)}_{i'_1,i_1}(r) = \sum_m^N C^{(\lambda,H)}_{i'_1,i_1,m}\chi_m(r). \tag{3.67}$$

This solution satisfies the wrong boundary conditions, i.e. $y(0) = y(r_{max}) = 0$. In order to get solution with the correct boundary conditions, we add non–homogeneous solution (with the correct boundary conditions) to the homogeneous solution,

$$y^{(\lambda)}_{i'_1,i_1}(r) = y^{(\lambda,H)}_{i'_1,i_1}(r) + y^{(\lambda,NH)}_{i'_1,i_1}(r). \tag{3.68}$$

General solution of non–homogeneous part of equation 3.65 is $y(r) = C_1 r^{\lambda+1} + C_2 r^{-\lambda}$, with unknown constants C_1 and C_2. Form the first boundary condition 3.66a we find $C_2 = 0$, and from the second 3.66b, $C_1 = \delta_{i'_1,i_1} r^{\lambda}_{i_1}/r^{2\lambda+1}_{max}$. Now we have non–homogeneous $y^{(\lambda,NH)}_{i'_1,i_1}(r)$ solution with the correct boundary conditions:

$$y^{(\lambda,NH)}_{i'_1,i_1}(r) = \delta_{i'_1,i_1}\frac{r^{\lambda}_{i_1}}{r^{2\lambda+1}_{max}} r^{\lambda+1} \tag{3.69}$$

We substitute the expansion in equation 3.65, multiply the whole equation by $\chi_{m'}(r)$ and integrate from $[0, r_{max}]$

$$\begin{aligned}\int_0^{r_{max}} \sum_m^N C^{(\lambda,H)}_{i'_1,i_1,m}\chi_{m'}(r)\left(\frac{d^2}{dr^2} - \frac{\lambda(\lambda+1)}{r^2}\right)\chi_m(r)\,dr = \\ -\int_0^{r_{max}} \chi_{m'}(r)\frac{2\lambda+1}{r}\chi_{i'_1}(r)\chi_{i_1}(r)\,dr.\end{aligned} \tag{3.70}$$

We define

$$T^{(\lambda)}_{m',m} = -\int_0^{r_{max}} \chi_{m'}(r)\left(\frac{d^2}{dr^2} - \frac{\lambda(\lambda+1)}{r^2}\right)\chi_m(r)\,dr, \tag{3.71}$$

which is exactly the kinetic energy operator. So we can write (within FEM-DVR basis)

$$\sum_m^N C^{(\lambda,H)}_{i'_1,i_1,m} T^{(\lambda)}_{m',m} = \delta_{i'_1,i_1}\delta_{i_1,m'}\frac{2\lambda+1}{r_{i_1}\sqrt{w_{i_1}}} \tag{3.72}$$

The inverse of kinetic energy matrix: $\left[T^{(\lambda)}\right]^{-1}$, for which

$$\sum_{m'}^{N} \left[T^{(\lambda)}\right]^{-1}_{m'',m'} T^{(\lambda)}_{m',m} = \delta_{m,m''} \tag{3.73}$$

holds, is multiplied by the whole equation and summation over m' indices is performed,

$$\begin{aligned}
\sum_{m'}^{N}\sum_{m}^{N} C^{(\lambda,H)}_{i'_1,i_1,m} \left[T^{(\lambda)}\right]^{-1}_{m'',m'} T^{(\lambda)}_{m',m} &= \sum_{m'}^{N} \left[T^{(\lambda)}\right]^{-1}_{m'',m'} \delta_{i'_1,i_1}\delta_{i_1,m'} \frac{2\lambda+1}{r_{i_1}\sqrt{w_{i_1}}} \\
\sum_{m}^{N} C^{(\lambda,H)}_{i'_1,i_1,m}\delta_{m,m''} &= \left[T^{(\lambda)}\right]^{-1}_{m'',i_1} \delta_{i'_1,i_1} \frac{2\lambda+1}{r_{i_1}\sqrt{w_{i_1}}} \\
C^{(\lambda,H)}_{i'_1,i_1,m''} &= \delta_{i'_1,i_1}\,(2\lambda+1)\,\frac{\left[T^{(\lambda)}\right]^{-1}_{m'',i_1}}{r_{i_1}\sqrt{w_{i_1}}},
\end{aligned} \tag{3.74}$$

which gives the solution for expansion coefficients.

Now we can write the solution with the correct boundary conditions by inserting the last equation in 3.74 into 3.67, and then substituting 3.67 and 3.69 in 3.68, leads:

$$y^{(\lambda)}_{i'_1,i_1}(r) = \delta_{i'_1,i_1}\,(2\lambda+1)\sum_{m}^{N}\chi_m(r)\frac{\left[T^{(\lambda)}\right]^{-1}_{m,i_1}}{r_{i_1}\sqrt{w_{i_1}}} + \delta_{i'_1,i_1}\frac{r^{\lambda}_{i_1}}{r^{2\lambda+1}_{max}} r^{\lambda+1}, \tag{3.75}$$

and we can substitute it back into the original expression for the two-electron integral, equation 3.64, to obtain

$$I^{(\lambda)}_{i'_1,i'_2,i_1,i_2} = \delta_{i'_2,i_2}\delta_{i'_2,i_2}\left(\frac{(2\lambda+1)\left[T^{(\lambda)}\right]^{-1}_{i_2,i_1}}{r_{i_2}\sqrt{w_{i_2}}r_{i_1}\sqrt{w_{i_1}}} + \frac{r^{\lambda}_{i_1}r^{\lambda}_{i_2}}{r^{2\lambda+1}_{max}}\right) \tag{3.76}$$

The expression in equation 3.76 is the final result for the two-electron radial integrals in the FEM-DVR basis. It has the remarkable property of being diagonal in the indices corresponding to the FEM-DVR grid points. It involves only the inverses of the kinetic energy matrices (times 2) in one dimension corresponding to each value, which need only to be calculated once, it also maintains the accuracy of the original Gauss–Lobatto quadrature upon which the FEM-DVR approach is based.

3.7.3 Electron-nuclear interaction

In contrast to electron-electron, which was already well explained for atomic systems [49], the electron-nuclear interaction term requires some modification of existing approach.

For H_2 system, in a symmetric basis 3.15, all the terms depending only on coordinates of the first electron will have exactly the same expression for the coordinate of the second electron. We can write

$$\begin{aligned}\langle j', i_1', l_1', m_1', i_2', l_2', m_2'|f(\boldsymbol{r}_1)|j, i_1, l_1, m_1, i_2, l_2, m_2\rangle = \\ \langle j', i_1', l_1', m_1', i_2', l_2', m_2'|f(\boldsymbol{r}_2)|j, i_1, l_1, m_1, i_2, l_2, m_2\rangle\,.\end{aligned} \tag{3.77}$$

Because of this property we can evaluate the terms: kinetic energy of electron 1 ($\boldsymbol{\nabla}^2_{r_1}$) and electron-nucleon interaction with electron 1 ($1/|\frac{1}{2}\boldsymbol{R}\pm\boldsymbol{r}_1|$), and multiply it by factor 2 to get the contribution from the other electron. Therefore we will derive expression for $1/|\frac{1}{2}\boldsymbol{R}\pm\boldsymbol{r}_1|$ term only.

$$V^{H_2}(\boldsymbol{r}_1) = -\frac{1}{|\frac{1}{2}\boldsymbol{R}\pm\boldsymbol{r}_1|} \tag{3.78}$$

Regardless the number of electrons of the molecular system, the electron-nuclear interaction term follows the expression (written now for the H_2^+ system):

$$\begin{aligned}\langle j', i_1', l_1', m_1', i_2', l_2', m_2'|V^{H_2}(\boldsymbol{r}_1)|j, i_1, l_1, m_1, i_2, l_2, m_2\rangle = \\ \delta_{j',j}\delta_{i_2',i_2}\delta_{l_2',l_2}\delta_{m_2',m_2}\,\langle i_1', l_1', m_1'|V^{H_2^+}(\boldsymbol{r}_1)|i_1, l_1, m_1\rangle\,,\end{aligned} \tag{3.79}$$

so in the rest of this section we will focus on evaluation of $1/|\frac{1}{2}\boldsymbol{R}\pm\boldsymbol{r}|$ for H_2^+ system.

$$\begin{aligned}V_{\substack{j',i',l',m'\\ j,i,l,m}} &\equiv -\langle j', i', l', m'|\frac{1}{|\frac{1}{2}\boldsymbol{R}\pm\boldsymbol{r}|}|j, i, l, m\rangle \\ &\equiv -\langle j', i', l', m'|\frac{1}{|\frac{1}{2}\boldsymbol{R}+\boldsymbol{r}|}+\frac{1}{|\frac{1}{2}\boldsymbol{R}-\boldsymbol{r}|}|j, i, l, m\rangle\,.\end{aligned} \tag{3.80}$$

As for the electron-electron interaction term given in 3.56, we write the interaction term in series of spherical harmonics which now depend on both $\hat{\boldsymbol{r}}$ and $\hat{\boldsymbol{R}}$:

$$\frac{1}{|\boldsymbol{r}\pm\frac{1}{2}\boldsymbol{R}|} = 4\pi\sum_{\lambda=0}^{\infty}\sum_{\mu=-\lambda}^{\lambda}\frac{1}{2\lambda+1}\frac{r_<^\lambda}{r_>^{\lambda+1}}Y_{\lambda\mu}(\hat{\boldsymbol{r}})Y^*_{\lambda\mu}(\pm\hat{\boldsymbol{R}}), \tag{3.81}$$

where $\frac{r_<^\lambda}{r_>^{\lambda+1}}$ stands for,

$$\frac{r_<^\lambda}{r_>^{\lambda+1}} \equiv \begin{cases} \frac{r^\lambda}{\left(\frac{1}{2}R\right)^{\lambda+1}}, & r < \frac{1}{2}R \\ \frac{\left(\frac{1}{2}R\right)^\lambda}{r^{\lambda+1}}, & r \geq \frac{1}{2}R, \end{cases} \tag{3.82}$$

and terms in 3.80 can be written as:

$$\begin{aligned} V^{(\pm)}_{\substack{j',i',l',m' \\ j,i,l,m}} &= -\sum_{\lambda=0}^{\infty}\sum_{\mu=-\lambda}^{\lambda} \frac{4\pi}{2\lambda+1} I^{(\lambda)}_{j',i',j,i} \left\langle j',i',l',m'|Y_{\lambda\mu}(\hat{\boldsymbol{r}})|j,i,l,m\right\rangle Y^*_{\lambda\mu}(\pm\hat{\boldsymbol{R}}) \\ &= -\sum_{\lambda=0}^{\infty}\sum_{\mu=-\lambda}^{\lambda} \frac{4\pi}{2\lambda+1} I^{(\lambda)}_{j',i',j,i} Y^*_{\lambda\mu}(\pm\hat{\boldsymbol{R}}) \\ &\quad (-1)^{m'}\sqrt{\frac{(2l'+1)(2\lambda+1)(2l+1)}{4\pi}} \begin{pmatrix} l' & \lambda & l \\ -m' & \mu & m \end{pmatrix} \begin{pmatrix} l' & \lambda & l \\ 0 & 0 & 0 \end{pmatrix}, \end{aligned} \tag{3.83}$$

where $I^{(\lambda)}_{j',i',j,i}$ is the radial integral for electron-nucleon interaction that is going to be derived here. The molecule is aligned along z-coordinate axis ($\hat{\boldsymbol{R}} = \hat{\boldsymbol{z}}$), where the spherical harmonics $Y^*_{\lambda\mu}$ can be evaluated as

$$\begin{aligned} Y^*_{\lambda\mu}(+\hat{\boldsymbol{R}}) &= Y^*_{\lambda\mu}(+\hat{\boldsymbol{z}}) = \delta_{\mu,0}\sqrt{\frac{2\lambda+1}{4\pi}} \\ Y^*_{\lambda\mu}(-\hat{\boldsymbol{R}}) &= Y^*_{\lambda\mu}(-\hat{\boldsymbol{z}}) = \delta_{\mu,0}\sqrt{\frac{2\lambda+1}{4\pi}}(-1)^\lambda, \end{aligned} \tag{3.84}$$

which limits the sum over μ in 3.83 to $\mu = 0$ contributions. By adding $V^{(+)}$ and $V^{(-)}$ to get 3.81, odd-λ contributions cancel, while even double:

$$V_{\substack{j',i',l',m' \\ j,i,l,m}} = (-1)^{m'+1} \sum_{\lambda=0,2,4\ldots} 2I^{(\lambda)}_{j',i',j,i}\sqrt{(2l'+1)(2l+1)} \begin{pmatrix} l' & \lambda & l \\ -m' & \mu & m \end{pmatrix} \begin{pmatrix} l' & \lambda & l \\ 0 & 0 & 0 \end{pmatrix}. \tag{3.85}$$

For $\mu = 0$ case and from 3-j selection rules, as described in B.7, we know that $V_{\substack{j',i',l',m' \\ j,i,l,m}}$ is different from 0 only if $m = m'$.

The radial integral $I^{(\lambda)}_{j',i',j,i}$ can be written explicitly as:

$$\begin{aligned} I^{(\lambda)}_{j',i',j,i} &= \langle j', i'| \frac{r_<^\lambda}{r_>^{\lambda+1}} |j, i\rangle \\ &= \langle \varphi_{j'}(R/2)\chi_{i'}(r)| \frac{r_<^\lambda}{r_>^{\lambda+1}} |\varphi_j(R/2)\chi_i(r)\rangle \\ &= \int_0^{r_{max}} \int_0^{R_{max}} \varphi_{j'}(R/2)\chi_{i'}(r) \frac{r_<^\lambda}{r_>^{\lambda+1}} \varphi_j(R/2)\chi_i(r)\, dR/2\, dr. \end{aligned} \tag{3.86}$$

The Gauss–Lobatto quadrature, of order n, is exact for integration of polynomials of order $m \leq 2n-1$, on the other hand function $\frac{r_<^\lambda}{r_>^{\lambda+1}}$ has derivative discontinuity that cannot be approximated by low order polynomials. The integral 3.86 can be simply evaluated in FEM-DVR, ignoring numerical error due to the discontinuity in the potential $\frac{r_<^\lambda}{r_>^{\lambda+1}}$. This can lead to the significant errors and instabilities in a calculation. Therefore, we instead apply the procedure employed in the previous section and transform the integral in equation 3.86 into the Poisson's differential equation. Figure 3.4 shows the potential energy curves computed using a direct numerical evaluation of the term $\frac{r_<^\lambda}{r_>^{\lambda+1}}$ in the FEM-DVR basis and the result of describing the electron-nuclear term using the Poisson's differential equation. We observe that, for identical FEM-DVR parameters, the direct numerical evaluation yields to numerical instabilities (red line in figure 3.4), while the evaluation of equation 3.86 allows for a numerically stable result. In order to avoid instabilities, the direct numerical evaluation would require a denser grid, significantly (and unnecessary) increasing the computational effort.

Although, it is in general possible to use the same basis functions for the electronic and nuclear motion, which would simplify the implementation, it would result in unnecessary large basis set and dense FEM-DVR grid. Instead, we chose to have two independent basis sets: one for nuclear and one for electronic motion. We have changed the label for basis function that describe electronic motion to φ, to be able to distinguish them from nuclear basis functions (χ). Following the same procedure as for electron-electron interaction we define function $y^{(\lambda)}_{jj'}(r)$

$$\begin{aligned} {y_{jj'}}^{(\lambda)}(r) =& r \int_0^{R_{max}} \chi_j(R)\chi_{j'}(R) \frac{r_<^\lambda}{r_>^{\lambda+1}}\, dR = \\ =& \int_0^r \chi_j(R)\chi_{j'}(R) \left(\frac{R}{r}\right)^\lambda dR + \int_r^{R_{max}} \chi_j(R)\chi_{j'}(R) \left(\frac{r}{R}\right)^{\lambda+1} dR, \end{aligned} \tag{3.87}$$

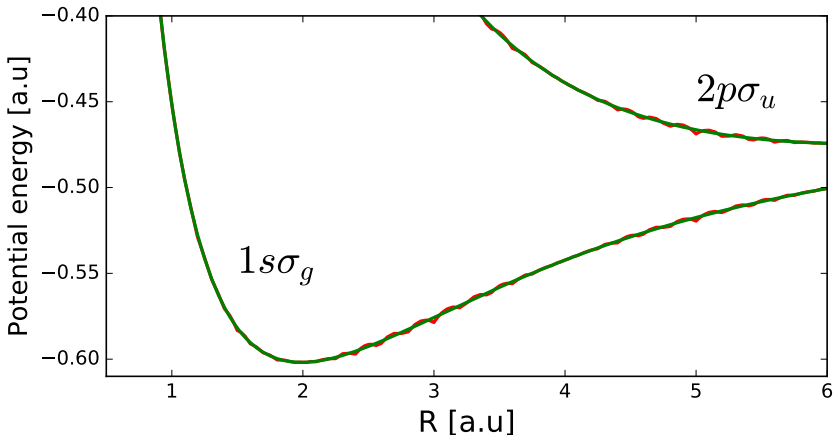

Fig. 3.4 Comparison of potential energy curves for H_2^+ system, calculated by the Poisson's differential equation (green) and the direct evaluation of $\frac{r_<^\lambda}{r_>^{\lambda+1}}$ in FEM-DVR basis (red), using the same parameters in both cases: DVR order= 15, $l_{max} = 10$.

here we did the coordinate transformation, $R/2 \to R$. The integral 3.86 becomes

$$I^{(\lambda)}_{j',i',j,i} = \int_0^{r_{max}} \varphi_i(r)\varphi_{i'}(r)\frac{{y_{jj'}}^{(\lambda)}(r)}{r}\,dr \tag{3.88}$$

By taking the second derivative of ${y_{jj'}}^{(\lambda)}(r)$, we can see that is satisfies the following equation. [1] (Poisson) differential equation.

$$\left(\frac{d^2}{dr^2} - \frac{\lambda(\lambda+1)}{r^2}\right){y_{jj'}}^{(\lambda)}(r) = -\frac{2\lambda+1}{r}\chi_j(r)\chi_{j'}(r). \tag{3.89}$$

The problem that immediately arises, is dependence of the function ${y_{jj'}}^{(\lambda)}(r)$ on the r_1 electronic coordinate, while functions $\chi_j(r)$ are defined on R internuclear (grid) coordinate but evaluated in electronic (grid) coordinate r. We will assume that these functions are defined on same interval. Our aim is to solve equation 3.89 with proper boundary conditions. From definition 3.87 we can see that ${y_{jj'}}^{(\lambda)}(r)$ satisfies the

[1] In contrast to original form, we have two functions φ and χ.

following boundary conditions

$$y^{(\lambda)}(r=0) = 0 \tag{3.90a}$$

$$y_{jj'}{}^{(\lambda)}(r_{max}) = \frac{1}{{r_{max}}^{\lambda}} \int_0^{R_{max}} \chi_j(R)\chi_{j'}(R) R^{\lambda}\, dR \tag{3.90b}$$

$$= \delta_{jj'} \frac{{R_j}^{\lambda}}{r_{max}^{\lambda}}.$$

We have assumed that $r_{max} > R_{max}$ and that we are interested in evaluating this integral in region where $r < R_{max}$. Expanding (homogeneous) solution of equation (3.89) in series of $\varphi_m(r)$ (electronic basis) functions, we get:

$$y_{jj'}{}^{(\lambda,H)}(r) = \sum_{m=0}^{N} C_{jj'm}{}^{(\lambda,H)} \varphi_m(r). \tag{3.91}$$

Again, this solution does not fulfill the proper boundary conditions. To get the solution with the correct boundary conditions, we add non–homogeneous solution with the correct boundary conditions to the homogeneous solution:

$$y_{jj'}{}^{(\lambda)}(r) = y_{jj'}{}^{(\lambda,H)}(r) + y_{jj'}{}^{(\lambda,NH)}(r). \tag{3.92}$$

From the general, non–homogeneous, solution of Poisson's equation $y(r) = C_1 r^{\lambda+1} + C_2 r^{-\lambda}$, and from the first boundary condition (3.90a), we find $C_2 = 0$, while from the second (3.90b), $C_1 = \delta_{j,j'} {R_j}^{\lambda} / {r_{max}}^{2\lambda+1}$. Now we have the non–homogeneous solution with the correct boundary conditions:

$$y_{jj'}{}^{(\lambda,NH)}(r) = \delta_{j,j'} \frac{{R_j}^{\lambda}}{{r_{max}}^{2\lambda+1}} r^{\lambda+1}. \tag{3.93}$$

To determine unknown coefficients in 3.91 we substitute the expansion in Poisson's equation 3.89, multiply the equations from the left with $\varphi_n(r)$ (electronic basis) function, and integrate. We get the following equation,

$$\sum_{m=0}^{N} C_{jj'm}{}^{(\lambda,H)} T^{(\lambda)}_{m',m} = \int_0^{\infty} dr \varphi_{m'}(r) \frac{2\lambda+1}{r} \chi_j(r)\chi_{j'}(r). \tag{3.94}$$

On the right hand side we have product of basis function defined on internuclear (φ) and electronic (χ), FEM-DVR grid, which means that they are not mutually orthogonal,

and simple relation as in 3.72 do not apply. To evaluate integral on the right hand side, we have two possibilities: either we can evaluate φ on electronic or χ on internuclear FEM-DVR grid points. We chose the second one, because in the problems that we are going to consider, internuclear grid is much more dense and the integral more accurately calculated. We define,

$$\begin{aligned} B_{jj'm'} &\equiv \int_0^{\infty} \varphi_{m'}(r)\frac{1}{r}\chi_j(r)\chi_{j'}(r)\,dr \\ &\cong \int_0^{r_{max}} \varphi_{m'}(r)\frac{1}{r}\chi_j(r)\chi_{j'}(r)\,dr \\ &\cong \delta_{j,j'}\frac{\varphi_{m'}(R_j)}{R_j\sqrt{w_m^{(r)}}} \equiv \delta_{j,j'}G_{jj'm'}, \end{aligned} \tag{3.95}$$

where $\varphi_{m'}(R_j)$ is transformation matrix between electronic and internuclear FEM-DVR basis. In general it is not rectangular matrix, and it is not proportional to $\delta_{m',j}$. Following the derivation from equation 3.74, we get formula for expansion coefficients,

$$\begin{aligned} \sum_{m=0}^{N} {C_{jj'm}}^{(\lambda,H)} T^{(\lambda)}_{m',m} &= -\,(2\lambda+1)\,B_{jj'm'} \\ \sum_{m'=0}^{N}\sum_{m=0}^{N} {C_{jj'm}}^{(\lambda,H)} \left[T^{(\lambda)}\right]^{-1}_{m'',m'} T^{(\lambda)}_{m',m} &= (2\lambda+1)\sum_{m'=0}^{N} \left[T^{(\lambda)}\right]^{-1}_{m'',m'} B_{jj'm'} \\ \sum_{m=0}^{N} {C_{jj'm}}^{(\lambda,H)} \delta_{m'',m} &= -\,(2\lambda+1)\sum_{m'=0}^{N} \left[T^{(\lambda)}\right]^{-1}_{m'',m'} B_{jj'm'} \\ {C_{jj'm''}}^{(\lambda,H)} &= (2\lambda+1)\sum_{m'=0}^{N} \left[T^{(\lambda)}\right]^{-1}_{m'',m'} B_{jj'm'}, \end{aligned} \tag{3.96}$$

where $\left[T^{(\lambda)}\right]^{-1}$ inverse of the internuclear kinetic energy operator. By inserting the coefficient ${C_{jj'm''}}^{(\lambda,H)}$ into the expansion 3.91, we get:

$${y_{jj'}}^{(\lambda,H)}(r) = (2\lambda+1)\sum_{m,m'=0}^{N} \left[T^{(\lambda)}\right]^{-1}_{m,m'} B_{jj'm'}\varphi_m(r). \tag{3.97}$$

Adding ${y_{jj'}}^{(\lambda,H)}$ and ${y_{jj'}}^{(\lambda,NH)}$ and inserting in 3.88, we get the final expression for the radial integral of electron-nucleon interaction

$$I^{(\lambda)}_{j',i',j,i} = \delta_{i,i'}\delta_{j,j'}\left((2\lambda+1)\sum_{m'=0}^{N}\left[T^{(\lambda)}\right]^{-1}_{i,m'}\frac{\varphi_{m'}(R_j)}{R_j r_i\sqrt{w^{(r)}_{m'}w^{(r)}_i}} + \frac{{R_j}^{\lambda}r_i^{\lambda}}{{r_{max}}^{2\lambda+1}}\right). \tag{3.98}$$

We can see that this operator, just like the electron-electron repulsion term, is diagonal in both electronic and internuclear basis.

Note that the previous formula is also applicable to the molecular system with a fixed internuclear coordinate (R_0, i.e. within the fixed nuclei approximation), by replacing the basis functions $\chi(r)$ with $\delta(r - R_0)$, in the definition of $B_{jj'm'}$ (3.95), which makes $I^{(\lambda)}_{i',i}$ independent of internuclear basis indices (j and j').

3.7.4 The dipole operator $\hat{\boldsymbol{\mu}}$

The dipole operator can be written in its spatial components:

$$\hat{\boldsymbol{\mu}} = \hat{\boldsymbol{z}}\mu_z + \hat{\boldsymbol{x}}\mu_x + \hat{\boldsymbol{y}}\mu_y, \tag{3.99}$$

where in general, for linearly polarized light and molecule aligned along z-axis, $\mu_x = \mu_y$. The dipole operator is a single-electron operator, and for two-electron system it is the sum of the contributions for each electron. Expressed in a symmetrized basis, the dipole operator can be written for one electron and and then scaled with the total number of electrons. Therefore, we will focus on expression for dipole operator in the single electron (molecular) system while generalization to two electron system is straightforward. We define the matrix elements of the dipole operator as

$$\underset{j,i,l,m}{\hat{\boldsymbol{\mu}}_{j',i',l',m'}} \equiv \langle j', i', l', m'|\hat{\boldsymbol{\mu}}|j, i, l, m\rangle\,, \tag{3.100}$$

where j corresponds to the index of internuclear radial basis function, i corresponds to the index of electronic radial basis function and l and m the angular quantum numbers associated to the spherical harmonics for the electrons.

Length gauge

Firstly, we consider the electric field linearly polarized, with the polarization vector defined parallel to the molecular axis (z-axis). The dipole operator can be written as a

product of spherical harmonics function and radial coordinate as:

$$\hat{\mu}_z = \hat{\boldsymbol{\mu}}\hat{\boldsymbol{z}} = \boldsymbol{r}\hat{\boldsymbol{z}} = r\cos(\theta) = r\sqrt{\frac{4\pi}{3}}Y_1^0(\hat{\boldsymbol{r}}). \tag{3.101}$$

The matrix element (non-symmetrized) that defines the transition between two states is given by:

$$\begin{aligned}
[\hat{\mu}_z]_{\substack{j',i',l',m'\\ j,i,l,m}} =& \langle j',i',l',m'|r\sqrt{\frac{4\pi}{3}}Y_1^0(\hat{\boldsymbol{r}})|j,i,l,m\rangle \\
=& \delta_{j',j}\delta_{i',i}r_i\,\langle l',m'|\sqrt{\frac{4\pi}{3}}Y_1^0(\hat{\boldsymbol{r}})|l,m\rangle \\
=& \delta_{j',j}\delta_{i',i}r_i(-1)^{m'}\sqrt{(2l'+1)(2l+1)}\begin{pmatrix} l' & 1 & l \\ -m' & 0 & m\end{pmatrix}\begin{pmatrix} l' & 1 & l \\ 0 & 0 & 0\end{pmatrix}.
\end{aligned} \tag{3.102}$$

From 3-j selection rules (see B.7) we see that conditions $m' = m$, must be satisfied. And moreover, $l' + l + 1$ must be an even integer (alternative formulation is $|l' - l| = 1$), which means dipole transition changes state of the system from *gerade* to *ungerade* and vice, a well-known dipole selection rule.

For an electric field, linearly polarized and with polarization vector perpendicular to the molecular axis, the dipole operator is product of radial coordinate and linear combination of two spherical harmonics:

$$\hat{\mu}_x = \hat{\boldsymbol{\mu}}\hat{\boldsymbol{x}} = \boldsymbol{r}\hat{\boldsymbol{x}} = r\sin(\theta)\cos(\phi) = r\sqrt{\frac{2\pi}{3}}\left(Y_1^{-1}(\hat{\boldsymbol{r}}) - Y_1^1(\hat{\boldsymbol{r}})\right), \tag{3.103}$$

and the corresponding matrix element (not symmetrized) follows,

$$\begin{aligned}
[\hat{\mu}_x]_{\substack{j',i',l',m'\\ j,i,l,m}} =& \delta_{j',j}\delta_{i',i}r_i(-1)^{m'}\sqrt{\frac{(2l'+1)(2l+1)}{2}} \\
&\times\left[\begin{pmatrix} l' & 1 & l \\ -m' & -1 & m\end{pmatrix} - \begin{pmatrix} l' & 1 & l \\ -m' & 1 & m\end{pmatrix}\right]\begin{pmatrix} l' & 1 & l \\ 0 & 0 & 0\end{pmatrix}.
\end{aligned} \tag{3.104}$$

In this case, selection rules for the dipole transition, derived from 3-j selection rules, require that $m' - m = \pm 1$, while they remain the same for l quantum number.

Velocity gauge

For an electric field linearly polarized in a direction parallel to the molecular axis (z), the dipole operator in velocity gauge reads

$$\hat{\mu}_z = \hat{\boldsymbol{\mu}}\hat{\boldsymbol{z}} = \boldsymbol{\nabla}\hat{\boldsymbol{z}} = \frac{d}{dz}, \tag{3.105}$$

which can be expressed as a commutator

$$\frac{d}{dz} = [\Delta, z] = [\Delta, r\cos(\theta)]\,, \tag{3.106}$$

where $\Delta = \nabla^2$ is Laplacian operator. Laplacian in spherical coordinates has the following form

$$\Delta = \frac{\partial^2}{\partial r^2} + \frac{1}{r}\frac{\partial}{\partial r} - \frac{\boldsymbol{L}^2}{r^2}. \tag{3.107}$$

The action of the dipole operator on l^{th} spherical (not reduced) radial function (R^l/r):

$$\begin{aligned}
\frac{d}{dz}\frac{R^l}{r} &= [\Delta, r\cos(\theta)]\,\frac{R^l}{r} \\
&= \Delta\left(\cos(\theta)R^l\right) - r\cos(\theta)\Delta\left(\frac{R^l}{r}\right) \\
&= \frac{2}{r}\left(\cos(\theta)\frac{\partial}{\partial r} + \frac{-\boldsymbol{L}^2\cos(\theta) + \cos(\theta)\boldsymbol{L}^2}{2r}\right)R^l \\
&= \frac{2}{r}\sqrt{\frac{4\pi}{3}}\left(Y_1^0(\hat{\boldsymbol{r}})\frac{\partial}{\partial r} + \frac{-\boldsymbol{L}^2 Y_1^0(\hat{\boldsymbol{r}}) + Y_1^0(\hat{\boldsymbol{r}})\boldsymbol{L}^2}{2r}\right)R^l,
\end{aligned} \tag{3.108}$$

and the corresponding (not symmetrized) matrix element is

$$\begin{aligned}
[\hat{\mu}_z]_{\substack{j',i',l',m' \\ j,i,l,m}} &= \langle j', i', l', m'|\frac{d}{dz}|j, i, l, m\rangle \\
&= 2\sqrt{\frac{4\pi}{3}}\delta_{j',j}\,\langle l', m'|\left[\frac{\partial}{\partial r}\right]_{i',i} Y_1^0(\hat{\boldsymbol{r}}) + \delta_{i,i'}\frac{-\boldsymbol{L}^2 Y_1^0(\hat{\boldsymbol{r}}) + Y_1^0(\hat{\boldsymbol{r}})\boldsymbol{L}^2}{2r_i}|l, m\rangle \\
&= 2\delta_{j',j}\left(\left[\frac{\partial}{\partial r}\right]_{i',i} + \delta_{i,i'}\frac{-l'(l'+1) + l(l+1)}{2r_i}\right) \\
&\quad \times (-1)^{m'}\sqrt{(2l'+1)(2l+1)}\begin{pmatrix} l' & 1 & l \\ -m' & 0 & m \end{pmatrix}\begin{pmatrix} l' & 1 & l \\ 0 & 0 & 0 \end{pmatrix}
\end{aligned} \tag{3.109}$$

Where $[d/dr]_{i',i}$ are matrix elements of derivative operator in a given *radial* electronic FEM-DVR basis.

For he perpendicular polarization, we take the polarization direction to be in x direction. We express the dipole operator as commutator of Laplacian and x-component of the dipole operator in spherical coordinates:

$$\hat{\mu}_x = \hat{\boldsymbol{\mu}}\hat{\boldsymbol{x}} = \boldsymbol{\nabla}\hat{\boldsymbol{x}} = \frac{d}{dx}, \tag{3.110}$$

$$\frac{d}{dx} = [\Delta, x] = [\Delta, r\sin(\theta)\cos(\phi)]\,, \tag{3.111}$$

we repeat the same procedure as for $\hat{\mu}_x$, by replacing $\cos(\theta) \to \sin(\theta)\cos(\phi)$, or $\sqrt{\frac{4\pi}{3}}Y_1^0(\hat{\boldsymbol{r}}) \to \sqrt{\frac{4\pi}{3}}\frac{1}{\sqrt{2}}\left(Y_1^{-1}(\hat{\boldsymbol{r}}) - Y_1^1(\hat{\boldsymbol{r}})\right)$, which gives:

$$\begin{aligned}
[\hat{\mu}_x]_{\substack{j',i',l',m'\\ j,i,l,m}} &= \langle j', i', l', m'|\frac{d}{dx}|j, i, l, m\rangle \\
&= 2\delta_{j',j}\left(\left[\frac{\partial}{\partial r}\right]_{i',i} + \delta_{i,i'}\frac{-l'(l'+1)+l(l+1)}{2r_i}\right) \\
&\quad\times\sqrt{\frac{4\pi}{3}}\,\langle l', m'|\frac{1}{\sqrt{2}}\left(Y_1^{-1}(\hat{\boldsymbol{r}}) - Y_1^1(\hat{\boldsymbol{r}})\right)|l, m\rangle \\
&= 2\delta_{j',j}\left(\left[\frac{\partial}{\partial r}\right]_{i',i} + \delta_{i,i'}\frac{-l'(l'+1)+l(l+1)}{2r_i}\right)(-1)^{m'}\sqrt{(2l'+1)(2l+1)} \\
&\quad\times\frac{1}{\sqrt{2}}\left[\begin{pmatrix} l' & 1 & l \\ -m' & -1 & m\end{pmatrix} - \begin{pmatrix} l' & 1 & l \\ -m' & 1 & m\end{pmatrix}\right]\begin{pmatrix} l' & 1 & l \\ 0 & 0 & 0\end{pmatrix},
\end{aligned} \tag{3.112}$$

and we have the expression for the dipole operator, obeying the same selection rules as in length gauge.

We have presented the details of numerical representation of the wave function, Hamiltonian and interactions with electromagnetic radiation for H_2^+ and H_2 systems, where all internal interactions and all degrees of freedom are taken into account. We use single center expansion of wave functions, where all angular dependencies are represented by spherical harmonic functions while radial dependencies of both electronic and nuclear motion are described by two independent sets of FEM-DVR functions using exterior complex scaling (ECS). We have extended the formalism for description of electron-nuclei interaction in atoms to two-center molecular case. In the following chapter we present formalism for scattering theory to treat molecular fragmentation of H_2^+ and H_2 upon photo-absorption.

Chapter 4

Molecular photoionization

Our goal is to investigate molecular ionization and excitation induced in by intense and ultrashort radiation sources. Photoionization of molecular systems. Most theoretical approaches reported so far explored H_2 in the fixed nuclei approximation (FNA), among which only a few works have considered both electronic and nuclear motion, while ignoring the effects of the electronic structure, eigenfunctions and oscillator strengths on the internuclear distance [79, 52]. Even within the FNA, some of these implementations has to be considered as groundbreaking, since they report the first successful attempts to interpret one-photon double ionization [24, 16, 83] and some of them even two-photon double ionization of $H2$ [55, 32, 25]. The BO approximation was implemented for the first time in [82] to describe double ionization after one-photon absorption. Still, the two-photon (multiphoton) four-body Coulomb break-up remains unsolved in full dimensionality, i.e., the effects of nuclear motion are still unexplored and the accuracy of the existing results within the FNA are yet to be confirmed, in particular multiphoton double ionization of molecules and dissociation into neutrals. Furthermore, the methods mentioned have not been able to address effects in which electronic and nuclear motion take place in the same timescale, e.g., autoionization, which is the mirror of electron correlation.

Even in the simplest atomic targets (helium), very few existing theoretical approaches have been able to provide an accurate description of the double ionization problem [20, 61]. In fact, only in the last decade, novel approaches, also using FEM-DVR implementations solving the time-dependent Schrödinger equation, were able to close a long-lasting debate on the two-photon double ionization problem in helium for which very few experimental data were available. Moreover, depending on the nature of the radiation sources employed, these processes can take place within a perturbative regime, with a relatively low intense light and involving the absorption of

few photons, or with more intense sources that may lead, for instance, to non-linear processes, which then requires the solution of the time-dependent Schrödinger equation. Time-independent approaches, based on the lowest-order perturbation theory, have been successfully employed in existing works studying excitation or single ionization of hydrogen molecules in FNA [83], as long as moderate intensities are employed such that the external perturbation can be consider much smaller then internal interactions in the system.

In the this section, we introduce the general expressions for time-dependent and independent LOPT, while in the next chapter we will present the problem-specific derivations. We will first provide the framework for a time-independent approach, valid for few photon absorption induced by moderately intense sources. Later, we will provide the nonperturbative TDSE method, not limited to moderately intense external fields.

4.1 Time independent LOPT approach

In physical problems involving very long laser pulses with narrow spectral bandwidth, of moderate intensities, time-independent lowest-order perturbation theory (LOPT) [30] is a good approximation. We will employ this approach to explore molecular photoionization upon one XUV photon absorption. Multiphoton processes, in the absence of non-linear effects, can also be described within a time-independent approach, as long as the LOPT is applied as the nth-order for a n-photon absorption. We first describe the method employed within the single photon absorption in a time-independent framework, to be later compared with the corresponding time-dependent treatment. The problems that can be treated within time-independent approaches usually imply a smaller size of the problem and lower computational effort. However, the use of monochromatic light, equivalent of very long pulses, prevent the extraction of dynamical properties of the system under study, although still provides significant information (total and differential in energy and angles of the ejected particles) on the photoionization event.

We will assume the molecular system in its ground state. The interaction with the light is written within the dipole approximation. The final wave function of the system after the light-molecule interaction, and imposing the proper outgoing boundary conditions can be written as the sum of the unperturbed function (Φ_0) and the scattered contribution ($\Psi_{sc}^{(+)}$):

$$\Psi^{(+)} = \Psi_{sc}^{(+)} + \Phi_0. \tag{4.1}$$

The amplitude associated to the single (or double) ionization event is associated with the purely outgoing wave function $\Psi_{sc}^{(+)}$, which is solution of the driven Schrödinger equation—the so-called "first order wave function", obtained when we treat the radiation field in the first order of time-independent perturbation theory. The LOPT equation (also referred as *time independent driven equation*) that describes photoionization from the ground state Φ_0 into a given final state $\Psi_{sc}^{(+)}$ is given by:

$$(E_0 + \omega - H)\,\Psi_{sc}^{(+)} = \hat{\boldsymbol{\mu}}\Phi_0, \tag{4.2}$$

where Φ_0 is the initial state of the system, E_0 is the energy of the initial state, ω is the photon energy and $\hat{\boldsymbol{\mu}}$ dipole operator describing interaction with the field. Within ECS formalism, there is no need for explicit imposition of outgoing boundary condition, they are automatically imposed by using coordinates transformed by ECS.

4.1.1 Optical theorem

The total photo-absorption cross section can be calculated by using well known optical theorem [26]

$$\sigma^{(ot,len)} = -\frac{4\pi}{c}\omega\,\mathrm{Im}\left(\langle\Psi_{sc}^{(+)}|\hat{\boldsymbol{\mu}}^{(len)}\Phi_0\rangle\right) \tag{4.3}$$

$$\sigma^{(ot,vel)} = -\frac{4\pi}{c}\frac{1}{\omega}\,\mathrm{Im}\left(\langle\Psi_{sc}^{(+)}|\hat{\boldsymbol{\mu}}^{(vel)}\Phi_0\rangle\right), \tag{4.4}$$

in length and velocity gauge, respectively. Calculated in this way the total cross section contains all possible channels in the photo-absorption, i.e. total and partial breakup: excitation, ionization and dissociation of the system. The use of the optical theorem thus prevents one to distinguish the contributions from single or double ionization or excitation, as well as retrieving the observables differential in angles or energy for the ejected fragments. An alternative to extract the distinct open channels is the computation of the flux but associating each channel to a different spatial region as we discuss next.

4.1.2 Quantum-mechanical flux

Another, rather direct, method to compute the total photo-absorption cross section (σ) is the definition of a quantum-mechanical flux, given as the ratio between the outgoing

(j_{out}) and incoming (j_{in}) quantum-mechanical fluxes of particles:

$$\sigma = \frac{j_{out}}{j_{in}} \tag{4.5}$$

In this case, cross sections can be resolved in the energies associated to the outgoing fragments as long as one removes the contribution from the bound states to the total final wave function. Those must be removed by projecting out all of the target bound-state contributions [48]. The probability current, defined by

$$\boldsymbol{J} = \frac{1}{2m}\left(\Psi^*_{sc}\boldsymbol{\nabla}\Psi_{sc} - \Psi_{sc}\boldsymbol{\nabla}\Psi^*_{sc}\right), \tag{4.6}$$

where m is the mass of the single particle (we ignore irrelevant phase factor $(-i)$), can be easily calculated for single electron and generalized to two-electron systems. In this work, we generalize the probability current to the system of non-identical particles, i.e. electron-nuclear system. Electron-nuclear system is defined by 6 coordinates (3 for each particle). Rather than having two particles in 3D coordinate system, we conceptualize one particle in 6D coordinate system, for which we define corresponding 6D probability current. We define 6D gradient operator, by absorbing mass factors of electron $(1/(2m))$ and photons $(1/(2M))$ into definition of gradient operator:

$$\boldsymbol{\nabla} \equiv \begin{pmatrix} \frac{1}{2m}\boldsymbol{\nabla}_r \\ \frac{1}{2M}\boldsymbol{\nabla}_R \end{pmatrix}, \tag{4.7}$$

and calculate the probability current in the same way as for single particle

$$\boldsymbol{J} = \left(\Psi^*_{sc}\boldsymbol{\nabla}\Psi_{sc} - \Psi_{sc}\boldsymbol{\nabla}\Psi^*_{sc}\right). \tag{4.8}$$

In order to calculate quantum-mechanical flux (j) we need to calculate integral over some hyper-surface in a 6D coordinates system,

$$j = \oint_S \boldsymbol{J} d\boldsymbol{a}, \tag{4.9}$$

where $d\boldsymbol{a} \equiv da \cdot \hat{\boldsymbol{n}}$, da is differential of hyper-surface area and $\hat{\boldsymbol{n}}$ is unit hyper-vector normal to the hyper-surface area. In theory, the hyper-surface, in N-dimensional space, can be any connected (N-1)-dimensional subspace enclosing the system of interest, giving choice-independent results. Because of practical reasons (angular expansion in spherical harmonics) we always choose hyper-surface which contains all angular coordinates and a curve in radial particle-particle subspace. The radial integration

curve is always in real-coordinate region, where the scattering function has physical meaning.

In our half-collision problem the incoming wave, defined implicitly by a flux of photons, is space-time constant which we have to evaluate in order to properly calculate the cross section in equation 4.5. The flux of outgoing particles is given by 4.9. In velocity gauge, a quantized photon in a box of volume V gives an interaction operator of $\frac{1}{c}\sqrt{\frac{2\pi c^2}{V\omega}}\hat{p}_z$ (see [23], Eq. 1.175). Going from velocity to length gauge for the cross section multiplies this by ω, giving $\sqrt{\frac{2\pi\omega}{V}}\hat{z}$. The incoming flux density for photon normalized like this is $j_{in} = \frac{c}{V}$ ([23], Eq. 1.195). Accordingly, for an interaction simply given by $\hat{z}$ (as we do in using $\mu\left|\Phi_0\right\rangle$ on the right hand side), we have implicitly multiplied the photon amplitude by $\sqrt{\frac{V}{2\pi\omega}}$, and the flux density is accordingly multiplied by the square of this, giving $j_{in} = \frac{c}{2\pi\omega}$. We thus get the expression for the total photo-ionization cross section $\sigma = \frac{j_{out}}{j_{in}} = \frac{2\pi\omega}{c} j_{out}$,

$$\sigma^{flux,len} = \frac{2\pi}{c}\omega \oint_S \boldsymbol{J}^{len} d\boldsymbol{a} \tag{4.10}$$

$$\sigma^{flux,vel} = \frac{2\pi}{c}\frac{1}{\omega} \oint_S \boldsymbol{J}^{len} d\boldsymbol{a}, \tag{4.11}$$

note the difference in the prefactor, compared to optical theorem.

4.2 Time dependent Schrödinger equation

The starting point for the time dependent treatment is solution of time dependent Schrödinger equation 4.12. We consider system initially in a single stationary state (more specifically, in its ground state) that is subjected to a time-dependent laser pulse initiated at $t = 0$. The wave function evolves under the time-dependent Schrödinger equation

$$i\frac{\partial}{\partial t}\Psi(t) = \hat{\boldsymbol{H}}(t)\Psi(t) \tag{4.12}$$

Once the pulse has finished at $t = t_{final}$ the outgoing fragments are still interacting with each other and for $t \geq t_{final}$ the wave packet describing the system propagates under the influence of the time-independent Hamiltonian $\hat{\boldsymbol{H}}$ of Eq. (4.12). After sufficiently long time the system relaxes in eigenstates of time-independent Hamiltonian, so we can use use the eigenfunctions of asymptotic Hamiltonian to extract the transition probability to a given final state.

The time dependence of $\Psi(t)$ for $t \geq t_{final}$ is then given explicitly as [60]

$$\Psi(t) = e^{-i\hat{\boldsymbol{H}}(t-t_{final})}\Psi(t_{final}) \tag{4.13}$$

We define a scattered wave (Ψ_{sc}) for the specific spectral component of final total energy E as the Fourier transform of the wave packet propagated in time from t_{final} to infinity. Now we take the Fourier transform of both sides of Eq. 4.13, at the same time defining the scattered wave as

$$\begin{aligned}\Psi_{sc} &\equiv -ie^{-iEt_{final}} \int_{t_{fin}}^{\infty} dt\, e^{i(E+i\epsilon)t}\Psi(t) \\ &= -ie^{-iEt_{final}} \int_{t_{fin}}^{\infty} dt\, e^{i(E+i\epsilon)t} e^{-i\hat{\boldsymbol{H}}(t-t_{final})}\Psi(t_{final})\end{aligned} \tag{4.14}$$

Making the change of variable $t \to t - t_{final}$, we obtain

$$\begin{aligned}\Psi_{sc} &= -i \int_{0}^{\infty} dt\, e^{i(E+i\epsilon-\hat{\boldsymbol{H}})t}\Psi(t_{final}) \\ &= \frac{1}{E + i\epsilon - \hat{\boldsymbol{H}}}\Psi(t_{final}),\end{aligned} \tag{4.15}$$

or, equivalently,

$$(E - \hat{\boldsymbol{H}})\Psi_{sc} = \Psi(t_{final}). \tag{4.16}$$

Ψ_{sc} satisfies the time-independent-driven equation (similar to 4.2), which in ECS treatment has purely outgoing behavior, from which all the physical information will be extracted.

4.2.1 Quantum-mechanical flux

The total photo-absorption probability for the specific total energy of the system E, can be also extracted from the definition of the quantum-mechanical flux of the scattered wave by placing Ψ_{sc}^{E} (calculated from TDSE and driven equation 4.16) in place of Ψ_{sc} in 4.8, defining quantum-mechanical probability current

$$\boldsymbol{J}^{(E)} = \left(\Psi_{sc}^{(E)*}\boldsymbol{\nabla}\Psi_{sc}^{(E)} - \Psi_{sc}^{(E)}\boldsymbol{\nabla}\Psi_{sc}^{(E)*}\right), \tag{4.17}$$

while the flux (j) is defined in the same way as in Eq. 4.9.

In order to independently extract single and double (one- and two-photon) ionization cross sections from the transition amplitudes previously obtained by solving the TDSE

equation, we use the expressions from [60], where we have to take into account shape function, i.e. Fourier transform of the vector potential ($\tilde{F}$) for one-photon absorption, by defining

$$\widetilde{j} = \frac{j}{|\tilde{F}|^2}. \tag{4.18}$$

We get expression for the single-photon absorption within the pulse bandwidth:

$$\sigma^{flux,len} = \frac{2\pi}{c}\omega\widetilde{j}^{len} \tag{4.19}$$

$$\sigma^{flux,vel} = \frac{2\pi}{c}\frac{1}{\omega}\widetilde{j}^{vel}, \tag{4.20}$$

where $\widetilde{j}^{len}$ and $\widetilde{j}^{vel}$ are obtained from 4.18 in length and velocity gauge, c is speed of light and $\omega = E_{final} - E_0$ is the energy of absorbed photon.

4.2.2 Surface integral technique

The scattering wave function Ψ_{sc}, defined in equation 4.16 for a given total energy of the system, contains the contributions of all the open channels. In contrast with the atomic case [20, 61], there is no previous theoretical works in molecular targets that provide a procedure to separate the contributions from each break-up channels, and more specifically, the full Coulomb breakup event. In the following, we discuss our implementation to fulfill this goal.

If we know the final unperturbed state Φ^f of the system, appropriate to the process under consideration, we can express the transition amplitude as [48]

$$f = \langle \Phi^f | E - \hat{\boldsymbol{H}} | \Psi^{(-)} \rangle \,, \tag{4.21}$$

where $\Psi^{(-)}$ is incoming wave, for example, in the case of ionization of a one-electron target with no angular momentum, Φ^f would be the product of two free functions.

Besides numerical instabilities, caused by overlap integrals between the free functions and discrete channel terms in the scattered wave that become δ functions for infinite volumes, in direct calculations of 4.21 [50], the Φ^f is not known for general multi-particle breakup processes (though it is known for the simplest system, the Hydrogen atom). Because of that, we use a *testing functions* that are eigenstates of the asymptotic Hamiltonian, which contains only single electron interaction terms.

The working equation that replaces 4.21 is

$$f = \langle \Phi_{(t)} | E - T - V_1 | \Psi_{sc}^{(-)} \rangle \,, \tag{4.22}$$

$\Phi_{(t)}$ is the testing function and $T + V_1$ is single particle operator, in which, T is kinetic energy operator and V_1 is single electron potential (usually Coulomb potential).

For example, double ionization transition amplitude of Helium atom, is described by

$$f(\boldsymbol{k}_1, \boldsymbol{k}_2) = \langle \Phi_{\boldsymbol{k}_1} \Phi_{\boldsymbol{k}_2} | \hat{\boldsymbol{H}} - E | \Psi_{sc}^{(-)} \rangle \,, \tag{4.23}$$

where $\Phi_{\boldsymbol{k}_1}$ and $\Phi_{\boldsymbol{k}_2}$ are momentum-normalized wave functions describing free electrons, in the presence of charge Z, which satisfy the Coulomb wave equation

$$\left(-\frac{1}{2}\nabla^2 + \frac{Z}{r} \right) \Phi_{\boldsymbol{k}} = \frac{k^2}{2} \Phi_{\boldsymbol{k}}. \tag{4.24}$$

In this case, it is correct to take a testing function with the outgoing boundary condition ($\Phi_{\boldsymbol{k}}^{(-)}$), which are orthogonal to the bound states of Helium atom.

The method can be further improved by expressing transition amplitude, given as volume integral in eq. 4.22, as a surface integral by using Green's theorem. We get:

$$f = \oint_S \left(\Phi_{(t)}^* \boldsymbol{\nabla} \Psi_{sc}^{(+)} - \Psi_{sc}^{(+)} \boldsymbol{\nabla} \Phi_{(t)}^* \right) d\boldsymbol{a}, \tag{4.25}$$

as explained in Appendix A.

4.2.3 Testing functions for molecular Coulomb breakup

For a n-electron atomic target, one can employ an uncorrelated product of Coulomb functions as the testing functions in equation 4.21. In the asymptotic limit, when the atomic potential has vanished, only the Coulomb terms are acting, therefore these functions are eigenfunctions of the Hamiltonian in the asymptotic limit where electrons are well separated and electron-electron interaction can be neglected. However, the Coulomb functions are not good approximation to the final state of molecular target, due to the its non-central potential. Therefore, we use the method that incorporates non-Coulomb contribution to the testing function, as described in [82]. In this section we will consider H_2^+ system, while generalization to H_2 is straightforward, if we ignore electron-electron interaction in the final state, by writing it as a product of uncorrelated single electron functions.

We construct the testing function as a product of electronic and internuclear testing functions within BO approximation. Within BO approximation, the constructed electronic functions have to be properly normalized before multiplication with the internuclear part, by including density of electronic states, as explained in [43]. For

nuclear testing function we take simple Coulomb functions that describes interaction of two nuclei.

In the asymptotic limit, the scattering wave ($\Phi^{(+)}(\mathbf{k},\mathbf{r})$) function for an electron can be described as sum of Coulomb wave function and *non-Coulomb* part. Written for a single internuclear distance:

$$\Phi^{(+)}(\mathbf{k},\mathbf{r}) = \chi(\mathbf{k},\mathbf{r}) + \Phi_c^{(+)}(\mathbf{k},\mathbf{r}), \tag{4.26}$$

where $\Phi_c^{(+)}$ is Coulomb function of electron which "feels" $Z = 2$ charge of nuclei, k refers to wave vector of outgoing electron and $\chi(\mathbf{k},\mathbf{r})$ is non-Coulomb contribution. We are using ECS, therefore correct boundary conditions will be automatically imposed. The non-Coulomb part $\chi(\mathbf{k},\mathbf{r})$, can be found as a solution of

$$\left(\frac{k^2}{2} - h\right)\chi(\mathbf{k},\mathbf{r}) = V\Phi_c^{(+)}(\mathbf{k},\mathbf{r}), \tag{4.27}$$

where h is one-electron Hamiltonian and

$$V = \left(\frac{2}{r} - \frac{1}{\left|\mathbf{r} - \frac{1}{2}\mathbf{R}\right|} - \frac{1}{\left|\mathbf{r} + \frac{1}{2}\mathbf{R}\right|}\right). \tag{4.28}$$

In our implementation, the final state can be expanded in spherical harmonics

$$\Phi^{(+)}(\mathbf{k},\mathbf{r}) = \sum_{l_k,l,m} \varphi_{l_k,l,m} Y^*_{l_k,m}(\hat{\mathbf{k}}) Y_{l,m}(\hat{\mathbf{r}}) \tag{4.29}$$

Coulomb wave function can be expanded in spherical harmonics as well:

$$\Phi_c^{(+)}(\mathbf{k},\mathbf{r}) = \sum_{l_k,l,m} \delta_{l_k,l}\phi_l^{(c)}(k;r) Y^*_{l_k,m}(\hat{\mathbf{k}}) Y_{l,m}(\hat{\mathbf{r}}) \tag{4.30}$$

Where $\phi_l^{(c)}(k;r)$ is radial Coulomb function with the prefactor $\frac{i^l e^{i\eta_l(k)}}{kr}$ contained within the function. We can also expand $\chi(\mathbf{k},\mathbf{r})$ function in the same manner.

$$\chi(\mathbf{k},\mathbf{r}) = \sum_{l_k,l,m} G^{(m)}_{l_k,l}(r) Y^*_{l_k,m}(\hat{\mathbf{k}}) Y_{l,m}(\hat{\mathbf{r}}) \tag{4.31}$$

Introducing the above expression in the time-independent equation defined in 4.27 we obtain:

$$(E_k - h) \sum_{l_k,l,m} G^{(m)}_{l_k,l}(r) Y^*_{l_k,m}(\hat{\mathbf{k}}) Y_{l,m}(\hat{\mathbf{r}}) = V \sum_{l_k,l,m} \delta_{l_k,l} \phi^{(k;c)}_l(r) Y^*_{l_k,m}(\hat{\mathbf{k}}) Y_{l,m}(\hat{\mathbf{r}}). \tag{4.32}$$

If we select a single component (l_k, m) in (4.32)

$$(E_k - h) \sum_{l,m} G^{(m)}_{l_k,l}(r) Y_{l,m}(\hat{\mathbf{r}}) = V \phi^{(c)}_{l_k,m}(k;r) Y_{l_k,m}(\hat{\mathbf{r}}), \tag{4.33}$$

we get

$$\sum_l \left(\delta_{l',l} E_k - h^{(m)}_{l',l} \right) G^{(m)}_{l_k,l}(r) = V^{(m)}_{l',l_k} \phi^{(c)}_{l_k}(k;r). \tag{4.34}$$

From 4.34 we can see that m is good quantum number, and that we can solve equation for each value of m separately. Solving 4.34, we get the radial part of final state as a sum of solution of non-Coulomb part and Coulomb function:

$$\varphi_{l_k,l,m}(r) = G^{(m)}_{l_k,l}(r) + \phi^{(c)}_{l_k}(k;r). \tag{4.35}$$

The final expression for the transition amplitude is

$$f(k_n, \mathbf{k}_e) = \left\langle \Phi_c(R) \Phi^{(+)}(\mathbf{k}, \mathbf{r}) | E - T - V_1 | \Phi_{sc} \right\rangle, \tag{4.36}$$

where $\Phi_c(R)$ is coulomb function describing motion of nuclei in a field of $Z = 1$ charge.

If we are interested in a transition to a final state with a specific energy but any possible outgoing direction, we need to integrate transition probability over all possible directions $(\mathbf{k})$ of outgoing electron, with $|\mathbf{k}|$ fixed by value of final energy:

$$\begin{aligned}
P(E_{k_n}, E_{k_e}) &\equiv |f(E_{k_n}, E_{k_e})|^2 && (4.37)\\
&= \int_{|\mathbf{k}_e|^2 = 2E_{k_e}} d\mathbf{k}_e \cdot |f(k_n, \mathbf{k}_e)|^2 && (4.38)\\
&= 2\pi \int_0^\pi d\Omega_{k_e} \sum_{l_{k_e}, l_{k'_e}, m, m'} Y^*_{l_{k_e},m} Y_{l_{k'_e},m'} f_{l_{k_e},m}(k_n, k_e) f^*_{l_{k'_e},m'}(k_n, k_e)\\
&= \sum_{l_{k_e},m} \left| f_{l_{k_e},m}(k_n, k_e) \right|^2.
\end{aligned}$$

Where

$$f_{l_k,m}(k_n,k) = \langle \Phi_c(R)\varphi_{l_k,l,m}(r)Y_{l,m}(\hat{\mathbf{r}})|E-T-V_1|\Phi_{sc}\rangle\,, \tag{4.39}$$

is a single spherical (wave-vector) component of transition amplitude for dissociative ionization of the system. Integral in 4.39 is evaluated by converting volume into surface integral, as in 4.25.

The total cross section for breakup can be calculated from the transition probability $P(E_n, E_e)$. If we are interested in the transition to any final state with the total energy E_{tot}, the transition probability reads:

$$\begin{aligned} |P_t(E_{tot})|^2 &= \int_0^{E_{tot}} |C(E_{tot}-E,E)|^2\, dE \\ &= \sum_i |P(E_{tot}-E_i,E_i)|^2\, \delta E_i. \end{aligned} \tag{4.40}$$

4.3 Dissociative excitation

The probability of exciting the molecular target can be extracted by a direct projection into the molecular eigenstates. We remark that this is only as an alternative method to extract the dissociative excitation in a straightforward manner, taking into account that the eigenstates are known and can be easily computed to compare with existing data obtained using spectral methods.

For dissociative excitation probability we calculate the ‘electronic‘ bound states within the Born-Oppenheimer (BO) approximation. Within BO approximation the Hamiltonian is separated in kinetic energy part (T) (which depends on internuclear coordinate R only) and remaining ‘electronic‘ Hamiltonian (H_{el}) in which internuclear coordinate R is treated parametrically,

$$H_{BO}\left(\boldsymbol{r},R\right) = T\left(R\right) + {H_{el}}^{R}\left(\boldsymbol{r}\right). \tag{4.41}$$

The wave function can be separated as

$$\Psi_{n,\nu_n}\left(\boldsymbol{r},R\right) = \frac{\chi_{n,\nu_n}\left(R\right)}{R}{\psi_n}^{R}\left(\boldsymbol{r}\right), \tag{4.42}$$

where ${\psi_n}^{R}\left(\boldsymbol{r}\right)$ is eigenfunction of electronic Hamiltonian ${H_{el}}^{R}$, and $\chi_{n,\nu_n}\left(R\right)$ of corresponding internuclear Hamiltonian $T\left(R\right) + \varepsilon_n(R)$. Index n corresponds to eigenstates

of electronic Hamiltonian, while indices ν_n designate eigenstates of internuclear Hamiltonian for each electronic state n.

First we calculate BO potential energy ($\varepsilon_n(R)$) curves by solving

$$\left[{H_{el}}^R(\boldsymbol{r}) - \varepsilon_n(R)\right] {\psi_n}^R(\boldsymbol{r}) = 0 \tag{4.43}$$

And then vibrational wave functions

$$\left[T(R) + \varepsilon_n(R) - E_{n,\nu_n}\right] \chi_{n,\nu_n}(R) = 0 \tag{4.44}$$

To calculate dissociative excitation probability $P(E_{n,\nu_n})$ we project final wave function $\Phi(t_{fin})$ on the BO bound state $\Psi_{n,\nu_n}(\boldsymbol{r}, R)$:

$$P(E_{n,\nu_n}) = \left|\langle \Psi_{n,\nu_n}(\boldsymbol{r}, R) | \Phi(t_{fin}) \rangle\right|^2. \tag{4.45}$$

The application of the methodology to investigate a real physical problem is not a trivial task and requires extensive numerical tests to assess the stability and convergence of the results. In fact, as it is well known, the accuracy of the numerical implementation and the computational effort required strongly depends on the problem under study. In the next sections, we provide the more relevant numerical tests, including the appropriate comparisons with theoretical data obtained with existing approaches when available.

Chapter 5

H_2^+ - computational details and implementation

In the following, we provide a detailed analysis of the advantages, limitations, accuracy and numerical implementation for the extraction methods described in the previous section. We employ a full-dimensional method, beyond BO approximation, that treats electronic and nuclear motion on equal footing. First, we discuss the most relevant details of the implementation to compute the eigenstates, specifically, convergence issues associated to the solution of the eigenvalue problem to retrieve the initial state of the molecular target in our FEM-DVR implementation. In a second step, we demonstrate the validity of our method to compute photoionization cross sections in the H_2^+ system, by comparison with recent existing works, using both time-dependent and time-independent approaches. We pay particular attention to the convergence tests and level of accuracy obtained when using the Optical theorem or the flux method (sections 4.1.1 and 4.1.2) to extract total photoionization cross sections. In the third place, we present a detailed study on the solution of the TDSE and the capabilities of our implementation to solve multiphoton ionization and excitation processes in one-electron diatomic molecular targets. Finally, we test the accuracy of the method by comparison with multiphoton single ionization problems in H_2^+. Our most recent implementation on H_2 is compared with the scarce available data for single ionization in full dimensionality or the two-photon double ionization data within the fixed nuclei approximation. The technical details regarding the basis sets employed in the applications here shown are also provided.

5.1 Calculation parameters

We are working in a full dimensional approach where electronic and nuclear coordinates are not separable, however, one can use the BO approximation, with the only goal of separately check the convergence and accuracy of each term. For this reason, we here solve equation 4.43. First, we investigate the convergence of our numerical treatment to describe the single-electron components of the Hamiltonian, i.e., we compute the potential energy curves of the H_2^+ system resulting from the solution of equation 4.43. We thus obtain $E(R)$, parametrically depending on R, and first explore the behavior for different values of maximum angular momenta in the expansion, i.e. the largest value of l for the spherical harmonics expansion. Figure 5.1 shows convergence on two parameters. We can see (Fig. 5.1 plot on the left) that the size of the internuclear box R_{max} doesn't change potential energy curve, it rather adds new points on the curve. We point out that this behavior would not be achieved in the case where we use same radial basis (FEM-DVR) functions for electronic and internuclear part (see Section 3.7.3), and constrain grid points with $R_i = 2r_i$. On the right hand side of Fig. 5.1, we see convergence in l_{max} parameter. Potential energy curve is well described for lower internuclear distance even with relatively small number of angular configurations. Because for atomic targets l is in fact a good quantum number, as we approach the united atoms limit, i.e. the more atomic-like system, convergence is achieved with a smaller angular momenta. As we increase R, more and more angular configurations are needed to properly describe system that doesn't have spherical symmetry. In problems, investigated in this work, in H_2^+ system, we have checked that there is no significant change of results when we increase $l_{max} = 10$ to $l_{max} = 12$.

We have also used the behavior of the electronic energies to check the convergence with the density of FEM_DVR points that defines the radial coordinates. The radial components are mostly determined by two parameters in the FEM-DVR basis set: the DVR-order and the size of the FEM elements fully detailed in section 3.4. Usually, we take a more dense grid in the Quality of (FEM-DVR) grid determines how well electron-nucleon interaction term is represented numerically and which is the highest continuum state that we can accurately represented in a given basis. Usually we take more dense grid in the region where the electrons and protons interact, while in the rest of the radial space we take less dense uniform FEM-DVR grid. For the photoionization problems we have explored here, we have used a DVR order of of 15 and separation of elements between $5a.u.$ and $10a.u.$. Obviously, these parameters should be carefully examined for photoionization problems involving high photoelectron energies.

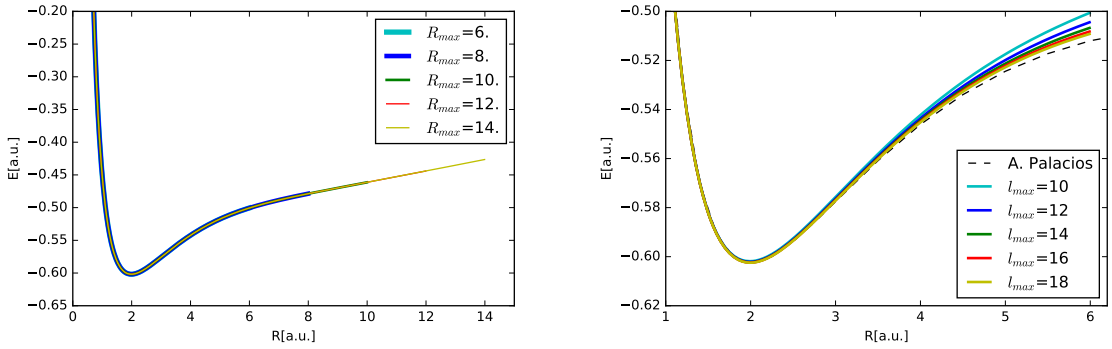

Fig. 5.1 Left: behavior of potential energy curve calculated within electronic boxes of different size R_{max}, for $1s\sigma_g$ electronic state. Right: convergence potential energy curve in l_{max}

.

5.2 Bound states

Once tested that the electronic terms can be reproduced with the desired accuracy, we now solve the full dimensional eigenvalue problem (equation 2.5). The total wave function now explicitly depends on the non-separable electronic and nuclear coordinates. We construct the full dimensional Hamiltonian, equation 2.1 of the H_2^+ ion in the absence of an external perturbation. We solve the eigenvalue problem in equation 2.5 by diagonalizing the full-dimensional Hamiltonian represented in real coordinates. We thus retrieve the energies and wave functions for the lowest energy states of the system, i.e. the bound vibrational states associated to the ground electronic state (vibronic).

If should be pointed out, when comparing with the conventional Born-Oppenheimer (BO) approximation results that, energies obtained in this way will correspond to the energies obtained as a solution of *vibrational* part of Hamiltonian in BO approximation. In the same way, the wave functions correspond to the *full* wave functions in BO approximation (i.e. product of corresponding electronic and vibrational wave function). Since we get the full spectrum of the system, the lowest eigenvalues will correspond to the vibrational energies of the lowest potential energy curve ($1s\sigma_g$) of BO approximation.

Figures 5.2 and 5.3, show the angular components of the wave functions, $\Psi_0^{(l)}(R,r)$, (where the full wave function is expanded as $\Psi_0(R,\boldsymbol{r}) = \sum_{l=1}^{l_{max}} \Psi_0^{(l)}(R,r)Y_{l,0}(\hat{\boldsymbol{r}})$) for the two lowest states for *gerade* (with $l = 0, 2, 4...$) and *ungerade* (with $l = 1, 3, 5...$) symmetry, respectively. As expected, magnitude of each component is decreasing with l, ensuring fast convergence in expansion in spherical harmonics. The lowest states (in each symmetry) doesn't have node (zero in $r - R$ plane), while first excited states have one node in R coordinate, which corresponds to nodes in vibrational eigen-functions in

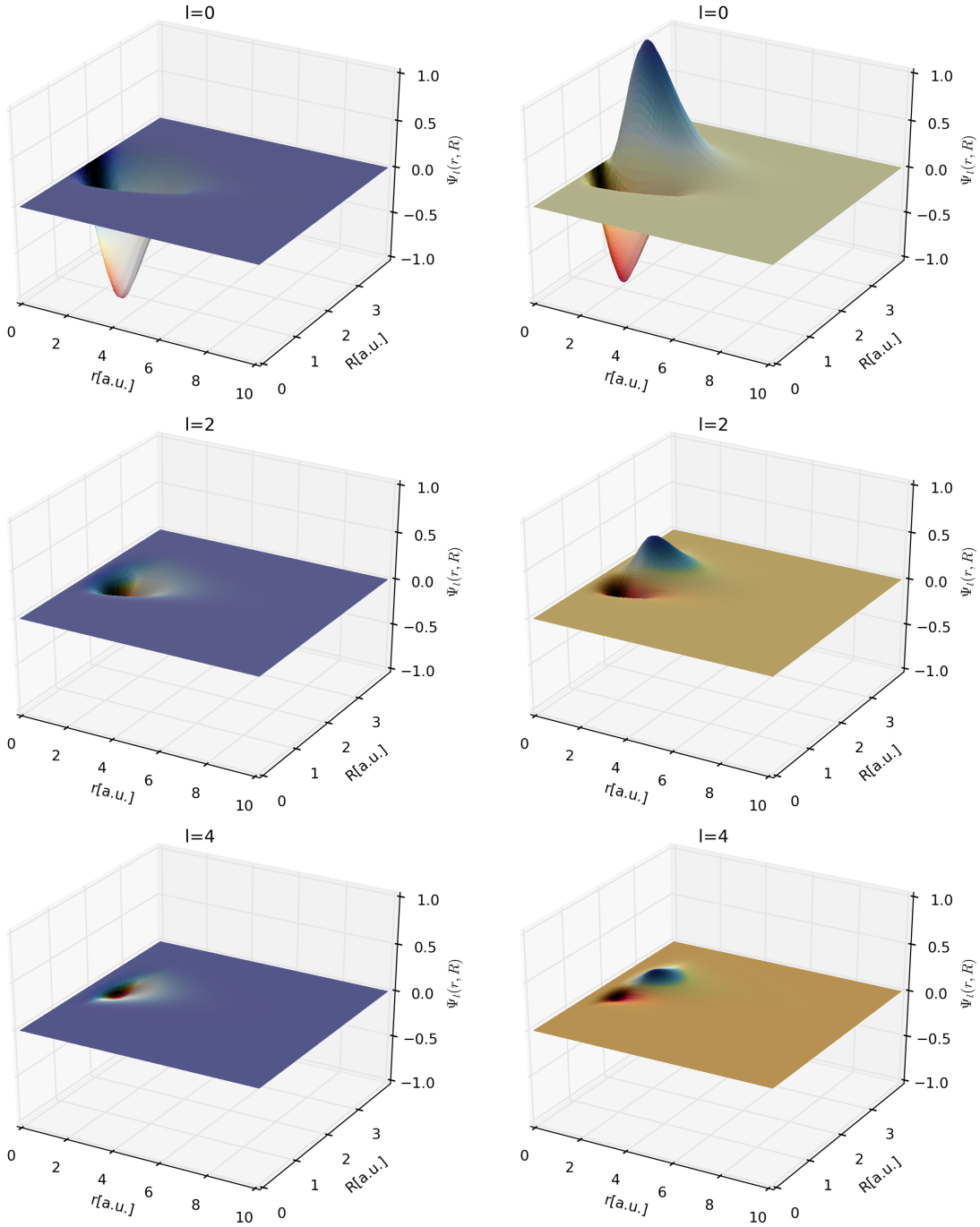

Fig. 5.2 Spherical components of the wave function for bound states of *gerade* symmetry. Left column: the lowest (ground) state ($n = 1$). Right column: the first excited state ($n = 2$).

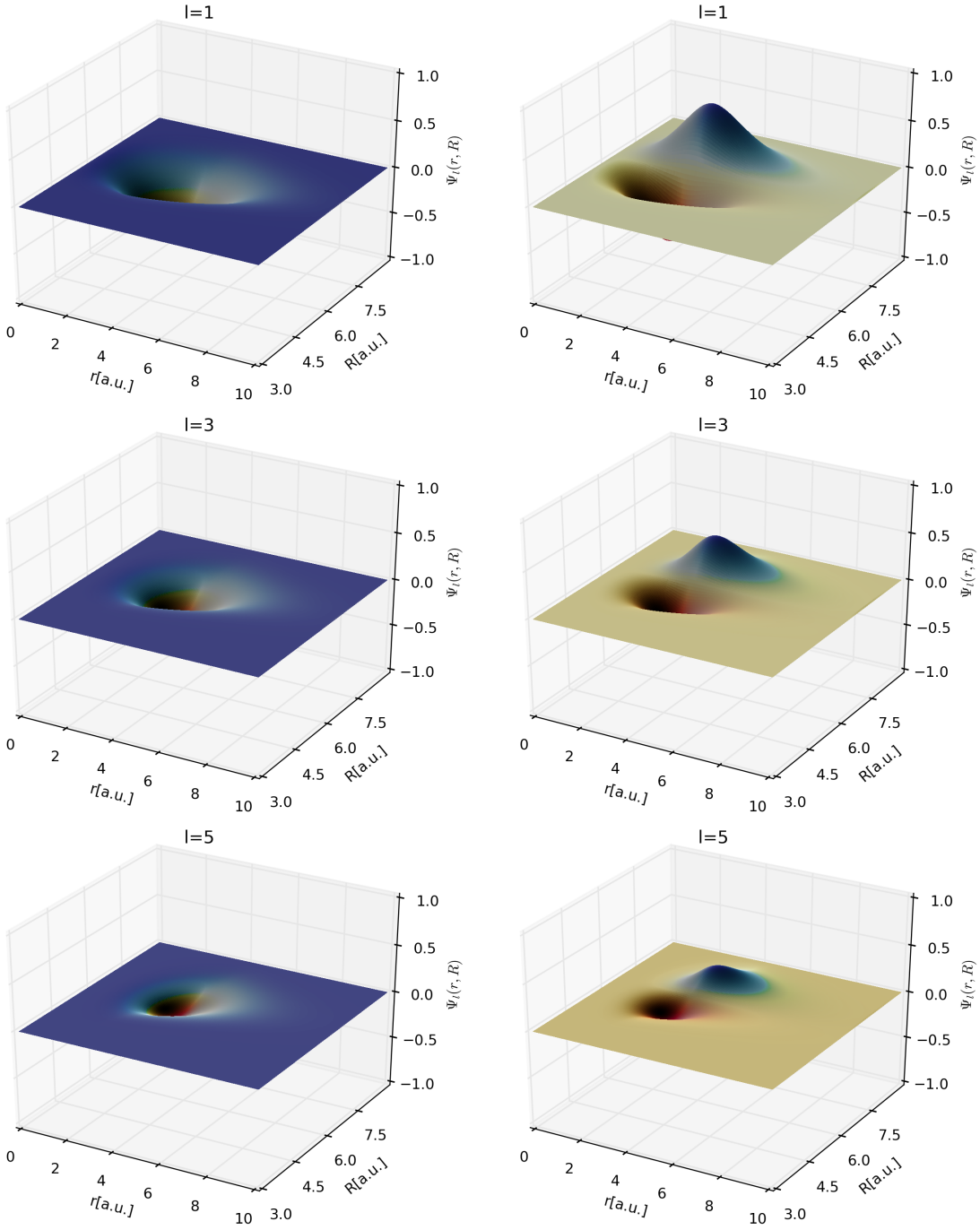

Fig. 5.3 Spherical components of the wave function for bound states of *ungerade* symmetry. Left column: the lowest state ($n = 1$). Right column: the excited state ($n = 2$).

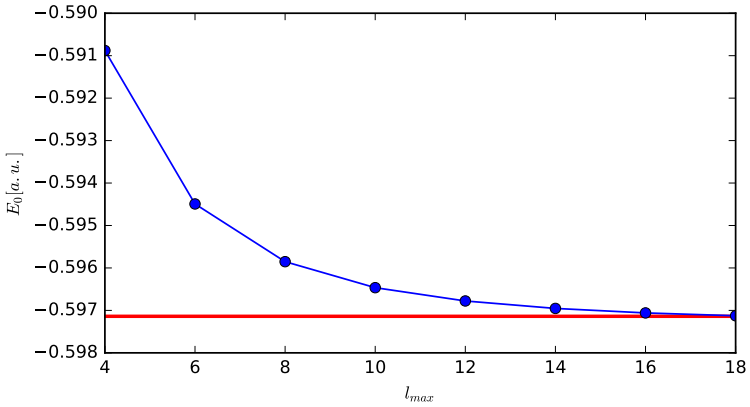

Fig. 5.4 Convergence of ground state energy of H_2^+ system with respect to l_{max} parameter (blue line) and precise value from literature [28] (red line).

BO approximation. In fig. 5.2, left side, we can see plots of the ground state functions, with correct maximum at $R = 2a.u.$, as expected from BO approximation.

The desired precision in calculation can be reached by sufficiently increasing truncation parameters. Our focus is the correct description of photo-breakup processes, that will inevitably involve some of the lowest bound states. The calculated ground state energy for $l_{max} = 18$ is $E_0 = -0.59715$, while very precise value from [28] gives $E_0 = -0.597139$. Figure 5.4 shows convergence of ground state energy with respect to l_{max} parameter, in most of the calculations in this work, value $l_{max} = 10$ gives satisfactory precision.

For results presented in this work we have used distributed-memory computers and Message Passing Interface (MPI) protocols in FORTRAN codes. Additionally we use *PETSc* [6] and *SLEPSc* [27] parallel libraries for solving large scale sparse linear system and eigenproblem on parallel computers.

5.3 Time-independent perturbation theory

5.3.1 Optical theorem

The simplest molecular photoionization event to be address in full-dimensionality is the ionization of the one-electron diatomic system, H_2^+, by one-photon absorption. In this context, one can use the optical theorem (section 4.1.1) to calculate the total photo-absorption cross section. Besides ground state wave function for this calculation we need Hamiltonian operator and dipole operator, which describes time-independent perturbation, i.e. interaction with the electromagnetic field (Eq. 4.2). For simplicity,

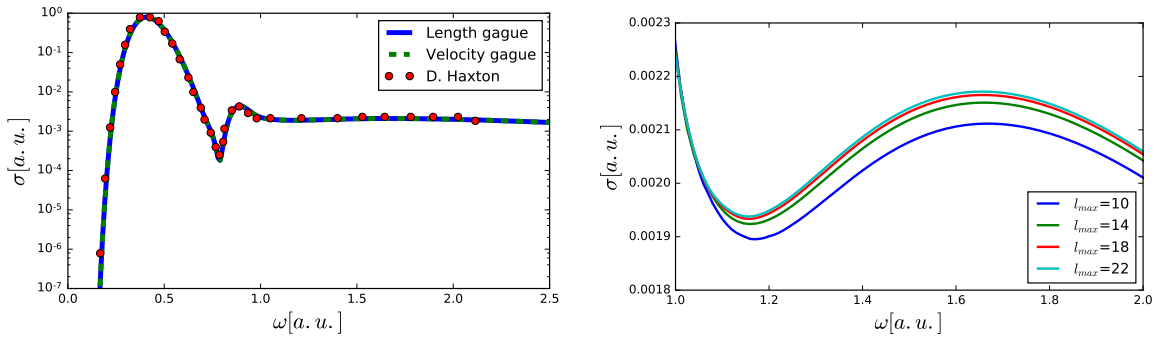

Fig. 5.5 The total cross section for single-photo-absorption for H_2^+ system calculated by optical theorem (sec. 4.1.1) method. Light is linearly polarized and polarization vector parallel to the molecular axis. Left: comparison with digitized data from [26] (red circles). Right: convergence with l_{max} parameter in velocity gauge.

we choose light to be linearly polarized and polarization vector parallel to the molecular axis.

In figure 5.5, we include the results obtained in velocity and length gauge. As explained in section 4.1.1, the gauge convergence is a very good check that ensures the completeness of the basis set for a given problem. On the right panel in figure 5.5, we check the convergence with the maximum angular momenta included. Note that we need much larger values that those to converge the ground state (see figure 5.4).

In contrast to ground state calculations, ECS formalism is necessary in order to impose correct boundary conditions to the final sates of the system. We use this calculations as a benchmark to test correctness of Hamiltonian and how truncation of the basis affect precision of calculation. In particular, how well continuum sates of the system is represented in given basis. Highly oscillatory, higher energy sates, will not be possible to represent in not very dense radial basis, which is manifested as nonphysical oscillations in total cross section for larger photon energies.

5.3.2 Quantum-mechanical flux

We now establish the validity of the quantum-mechanical flux method to compute the total photo-absorption cross section (section 4.1.2). There have been previous implementations of time-independent quantum-mechanical flux method [48, 47], but, to our knowledge, it has not been applied to the systems of two different particles in full dimensionality.

In contrast to the optical theorem, the time-independent quantum-mechanical flux, by selecting specific components of probability current vector, offers possibility

of distinguishing contributions to the total cross section from each particle. Also, this method provides convenient test for implementation of surface integrals, that are extensively used in the rest of this work. We will show later, that it can be used in time-dependent methods as well.

We use 4.2 to calculate scattering wave $\Psi_{sc}^{(+)}$ functions for each photon energy ω, but rather than projecting it to $\hat{\boldsymbol{\mu}}\Phi_0$, we calculate generalized probability current by using 4.8.

We define generalized vector space spanned by all coordinates of all independent particles, more formally: a vector ($\boldsymbol{v}$) in generalized vector space is a direct sum of vectors $\boldsymbol{r}_i$ that describe particles in coordinate space.

$$\boldsymbol{v} \equiv \boldsymbol{r}_1 \oplus \boldsymbol{r}_2 \oplus \boldsymbol{r}_3 ... \tag{5.1}$$

The generalized probability current describing n-particles, in full dimensionality, is a vector in $3n$ dimensional hyperspace, and a closed hyper-surface will be $3n-1$ dimensional manifold. It has a one vector component for each independent particle of the system, in the case H_2^+ molecule:

$$\boldsymbol{J} = J_R\hat{\boldsymbol{R}} + J_r\hat{\boldsymbol{r}}, \tag{5.2}$$

where $\hat{\boldsymbol{R}}$ and $\hat{\boldsymbol{r}}$ are (generalized) unit vectors representing nuclei and electron respectively, and J_R and J_r are scalar components. We must make clear that in this context, $\hat{\boldsymbol{R}}$ and $\hat{\boldsymbol{r}}$ are units vectors in a more general vector space spanned by $\hat{\boldsymbol{R}}$ and $\hat{\boldsymbol{r}}$, rather than just being unit vectors in pure coordinate space, i.e. $(\hat{\boldsymbol{R}}, \hat{\boldsymbol{0}}) \equiv (R, \theta_R, \phi_R, 0, 0, 0)$ and $(\hat{\boldsymbol{0}}, \hat{\boldsymbol{r}}) \equiv (0, 0, 0, r, \theta_r, \phi_r)$. A vector in this general vector space, specifies positions of all particles simultaneously, and since $\hat{\boldsymbol{R}}$ and $\hat{\boldsymbol{r}}$ describe independent particles they must be linearly independent vectors in general vector space. The same as generalized probability current, we have the generalized gradient operator (4.7), defined as:

$$\boldsymbol{\nabla} \equiv \boldsymbol{\nabla}_R + \boldsymbol{\nabla}_r, \tag{5.3}$$

where

$$\boldsymbol{\nabla}_R \equiv \frac{1}{2M}\boldsymbol{\nabla}_R \tag{5.4}$$

$$\boldsymbol{\nabla}_r \equiv \frac{1}{2m}\boldsymbol{\nabla}_r, \tag{5.5}$$

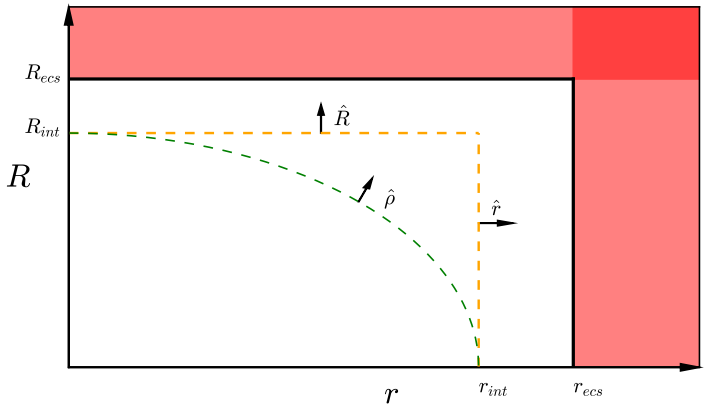

Fig. 5.6 ECS region and integration contours in radial coordinate subspace. Red area: ECS region, white area: real coordinate-region, orange dashed line: rectangular integration contour, green dashed line: parabolic integration contour.

are gradient operators in $\hat{\boldsymbol{R}}$ and $\hat{\boldsymbol{r}}$ subspaces ,respectively, and M and m are masses of particles. Since we are working in coordinates defined by 2.2, M should correspond to reduced nuclear mass. From definition of probability current:

$$\begin{aligned} \boldsymbol{J} &= (\Psi^*_{sc}\boldsymbol{\nabla}\Psi_{sc} - \Psi_{sc}\boldsymbol{\nabla}\Psi^*_{sc}) \\ &= (\Psi^*_{sc}(\boldsymbol{\nabla}_R + \boldsymbol{\nabla}_r)\Psi_{sc} - \Psi_{sc}(\boldsymbol{\nabla}_R + \boldsymbol{\nabla}_r)\Psi^*_{sc}) \,, \end{aligned} \tag{5.6}$$

and 5.2, we can see that components of probability current for nuclei is

$$J_R\hat{\boldsymbol{R}} = (\Psi^*_{sc}\boldsymbol{\nabla}_R\Psi_{sc} - \Psi_{sc}\boldsymbol{\nabla}_R\Psi^*_{sc}) \,, \tag{5.7}$$

and for electron

$$J_r\hat{\boldsymbol{r}} = (\Psi^*_{sc}\boldsymbol{\nabla}_r\Psi_{sc} - \Psi_{sc}\boldsymbol{\nabla}_r\Psi^*_{sc}) \tag{5.8}$$

From the probability current ($\boldsymbol{J}$), we obtain the quantum-mechanical flux (j), by calculating surface integral in 4.9 over a closed hyper-surface in real (non-ECS) region. For the integration of the generalized probability current over a closed hyper-surface, we choose a surface which contains all angular subspaces and one-dimensional subspace of $r - R$ radial subspace. In other words, we integrate over all angular coordinates and an integration curve in $r - R$ plane. The reason for this choice of integration hyper-surface is both, practical and physical: the angular part of wave functions is expanded in ortonormal (spherical harmonics) basis functions, and we have more control on physical

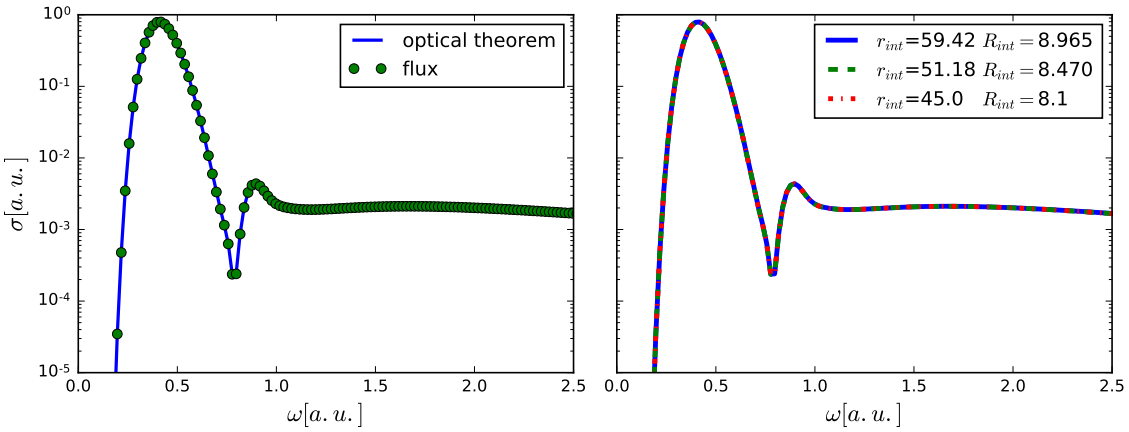

Fig. 5.7 Total cross section calculated by time-independent quantum-mechanical flux. Left: comparison with optical theorem. Right: calculated on different rectangular integration curves (Fig. 5.6, orange line).

system contained within closed hyper-surface by varying size of space enclosed by the surface.

Previous implementation of FEM-ECS method [82, 51], implemented for two electron systems, are using circular integration curve in $r_1 - r_2$ plane, defined by $\rho^2 = r_1^2 + r_2^2$, where r_1, r_2 are radial coordinates of electrons and ρ integration radius. In surface integrals, the results are independent on variation of ρ for large enough values, which provides good convergence test.

For two-different-particle systems, each one described by its radial coordinate, we must use a more general elliptical integration curve defined by $1 = \frac{R^2}{R_{int}^2} + \frac{r^2}{r_{int}^2}$, as illustrated in figure 5.6 by green line. In surface integral, we must find a vector normal to the integration curve, which is more challenging with respect to the circular case. Integration over an elliptical curve requires the explicit evaluation of the FEM-DVR basis functions (and its derivatives) in points that are not FEM-DVR grid points, and therefore in a large problems are computationally expensive. Instead, we choose to exploit properties of FEM-DVR basis and choose rectangular curve that lay on FEM-DVR grid points (as in [40]) (orange curve in Fig. 5.6) defined by two integration lines $L1$ and $L2$:

$$\begin{aligned} L1 &: r \in [0, r_{int}],\ R = R_{int},\ \hat{\boldsymbol{n}} = \hat{\boldsymbol{R}} \\ L2 &: R \in [0, R_{int}],\ r = r_{int},\ \hat{\boldsymbol{n}} = \hat{\boldsymbol{r}}, \end{aligned} \tag{5.9}$$

where $\hat{\boldsymbol{n}}$ is unit vector normal to the curve in $R - r$ plane. In this way, there is no need for explicit evaluation of basis functions, as expansion coefficient provide values

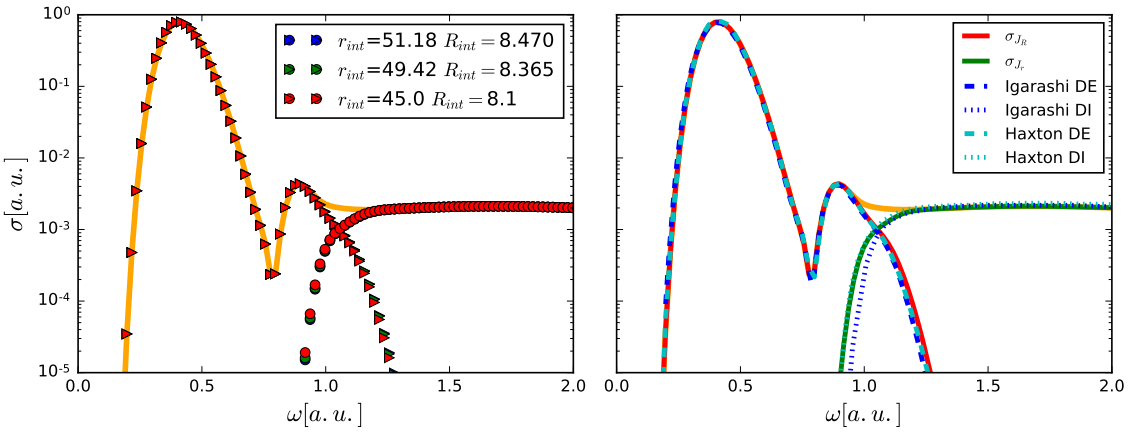

Fig. 5.8 Total cross section (orange full line) calculated by time-independent quantum-mechanical flux, separated in dissociative ionization (DI) and dissociative excitation (DE). Left: different colors represent dependence of DE and DI on choice of integration curve, DE (triangles) coming from J_R component and DI coming from J_r contribution of probability current. Right: comparison with data digitized from reference [31] (blue lines) and [26] (cyan line).

on grid points, we have derivative operator provided and we can use Gauss-Lobatto quadrature directly. Additional advantage of this choice of integration curve is that (because of ortonormality of $\hat{\boldsymbol{R}}$ and $\hat{\boldsymbol{r}}$) surface integral of $J_R\hat{\boldsymbol{R}}$ is nonzero on $L1$ only, and surface integral of $J_r\hat{\boldsymbol{r}}$ is nonzero on $L2$ only.

We find very good agreement (up to numerical precision) between results calculated on elliptical and on rectangular integration curve, therefore, we continue to use rectangular integration curve. Figure 5.7 on left, demonstrates the perfect agreement between the optical theorem and the time-independent quantum-mechanical flux method. The right panel of figure 5.7 shows the convergence of the results with the values of R_{int} and r_{int}, where electrons and nuclei are represented. As it is shown, for the one-photon absorption processes leading to single ionization results are converged for $45a.u.$ and $8.1a.u.$ box sizes for electrons and nuclei, respectively.

The separation of probability current 5.2 gives us a way to distinguish contributions probabilities carried by each particle. The probability current component, associated to motion of nuclei, $J_R\hat{\boldsymbol{R}}$, we identify as dissociative excitation (DE) and, associated to motion electron $J_r\hat{\boldsymbol{r}}$, as dissociative ionization (DI) contributions to the total cross section. In figure 5.8, on the left, we can see how each contribution depends on the choice of integration curve. There are intervals of photon energies where the contribution of a given component clearly dominates. Moreover, the agreement with

the total cross section is prefect and essentially independent on choice of integration curve, however in the region where both components are important, we can see that the cross section is more dependent on choice of integration curve. In figure 5.8 on the right we can see, comparison with the data from [31] and [26], where we can see better agreement with [26] where the similar quantum-mechanical flux method is used. Results obtained for time-independent calculations, describing, monochromatic transition, can be reproduced in time-dependent methods by using very long pulses, which have very narrow spectral distributions, and are close to monochromatic case.

5.4 Time-dependent Schrödinger equation

The previous results are obtained using the lowest-order for the time-independent perturbation theory, which is valid for single photon absorption total cross section and, as we have seen for the flux method, yields accurate results for the dissociative and non-dissociative components. While the optical theorem, by definition, restrict the approach to single photon absorption in a perturbative regime, the use of the flux method for the extraction of ionization and dissociation amplitudes remains valid in the context of time-dependent treatments. The approach can thus be further generalized by iterating equation 4.2, as described in [30], and obtain the scattering wave function for *two photon* absorption. If we are interested in *dynamics* of the system, triggered by external electromagnetic field, we should appeal to the solution of the time-dependent Schrödinger equation (TDSE) to describe the time-evolution of the molecular target in the presence of an external electromagnetic field. For the H2+ system, with linear polarization and parallel orientation with respect to the molecular axis of electromagnetic field, we can write TDSE as

$$i\frac{\partial}{\partial t}\Psi(R,\boldsymbol{r},t) = \hat{\boldsymbol{H}}(t)\Psi(t), \tag{5.10}$$

where the wave function $\Psi(R,\boldsymbol{r},t)$ describes positions of both protons and electron during time, and Hamiltonian $\hat{\boldsymbol{H}}(t)$ consists of time-independent field-free part $\hat{\boldsymbol{H}}_0$ and time-dependent part $\hat{\boldsymbol{H}}_{em}$, given by 2.31 and 2.27. We assume that system is initially in ground sate ${}^2\Sigma_g^+(1s\sigma_g)$, i.e. $\Psi(R,\boldsymbol{r},t=0) = \Psi_0(R,\boldsymbol{r})$ and has energy E_0, as described in section 5.2.

In the presence of electromagnetic field, the time-dependent part of Hamiltonian, which is product of electric field (vector potential in velocity gauge) and dipole operator (equations 2.34 and 2.35), repeatedly acts on the wave function during the time

propagation, preventing system from relaxing in stationary state. Selection rules for dipole transition allows only transition from *gerade* to *ungerade* symmetry (and vice versa). This means that in directly solving TDSE, we get contributions from absorption of any number of photons, but still, we can distinguish contributions of absorption of *odd* number of photons (leading to transitions between states with different parity symmetry), and absorption of *even* number of photons (leading to transitions between states with the same parity symmetry).

Specific physical process are investigated by using different electromagnetic fields. The electromagnetic field is characterized by electric field or vector potential function, characterized by pulse parameters like, shape of the pulse, frequency, chirp, pulse duration ... In the present work, we will employ finite pulsed radiation described with Gaussian or Sine-squared functions to account for the finite duration of the pulse [64]. The specifics of the pulses are given in their respective sections.

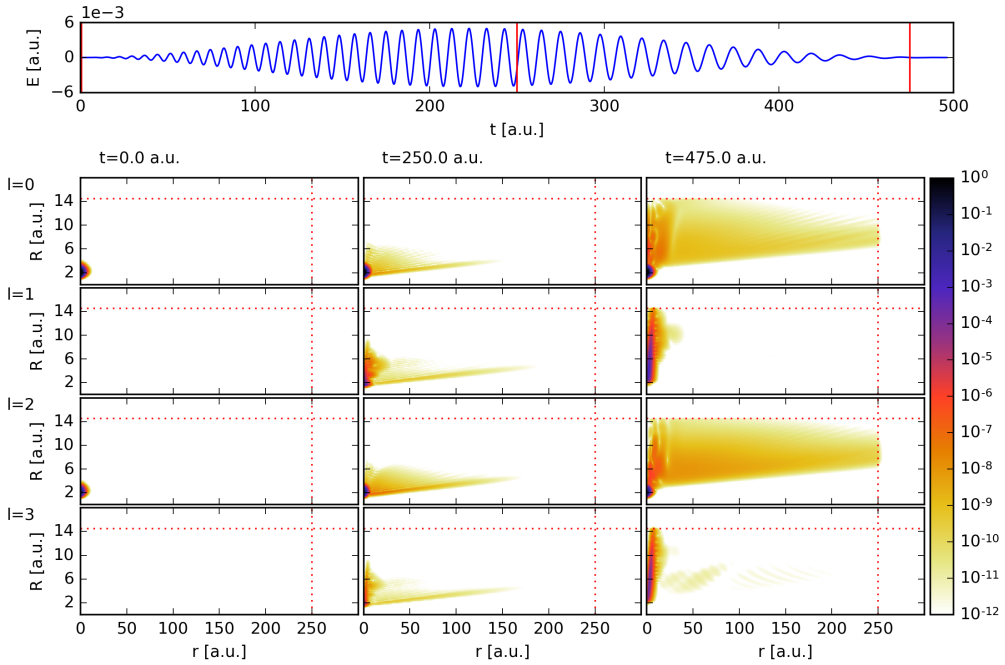

Fig. 5.9 Example of evolution of the system during pulse propagation. Top panel: Electric field of pulse interacting with the system. Bottom: Each column represents wave function (absolute value squared) at different time, while each row represents different angular component (l) in expansion in spherical harmonics ($Y_l^m(\boldsymbol{r})$).

In figure 5.9 we plot different angular components of the numerical molecular wave function for the H_2^+ system under the influence of the finite pulse plotted in the upper panel. In brief, we use a sine-squared envelope in time, for a pulse with a central

frequency of $\omega_0 = 0.6 a.u.$, total duration of $496 a.u.$ (i.e.$12 fs$) and linear chirp rate $-0.0000416667\omega_0 as$. Such radiation parameters may lead to one-photon dissociation or few-photon ionization of the system. We have plotted the wave function components for the lowest angular momenta, taking into account that most of the probability remains in $l = 0, 2, ...$ which is the largest contribution to the ground state of the system. As the pulse interacts with the system, we observe that the system evolves in both R and r coordinates simultaneously. We can already identify DE as process taking place mostly in R direction, and DI in r direction. Presence of electromagnetic field allows population of ungerade symmetry, as can be seen from middle column. By using long enough electromagnetic field, the system is eventually reaching ECS region, and probability gets absorbed in both R and r direction, as shown in third column. Because we aim to extract the ionization process, the absorption of part of the wave function is not desirable, we use the ECS merely as a tool to impose the correct boundary conditions. However, one has to ensure that there is no absorption for the parts of the wave function that account for the process of interest.

In solving TDSE we employ several numerical methods: Runge-Kutta ordinary differential equations solver schemes of order 3 (adaptive-time steps) and order 4 (nonadaptive-time steps) [6], as well as Cranck-Nicholson propagator [60]. The obtained results are always tested for independence on employed numerical method.

5.4.1 Quantum-mechanical flux

Solving the TDSE during the finite pulse propagation, we obtain a final wave function $\Psi(t_{final})$, which contains all necessary information about all processes occurred during interaction with an electromagnetic field. To be able to extract the information about a specific process in which all particle leave as free particle (Coulomb explosion) we use equation 4.16 to calculate Ψ_{sc}, which is one spectral component, of wave function $(\Psi(t_{final}))$, implicitly propagated to $t \to \infty$, see section 4.2.1. From Ψ_{sc} we calculate quantum-mechanical flux by using 4.17, in the similar way as in time-independent case, we calculate the total cross section by using 4.20. Not that in this case we have to take into account the system-independent "shape function" in equation 4.18, which is, for single photon absorption, equal to the spectral function (absolute value to the square of Fourier transform of vector potential), as explained in [60].

In figure 5.10, on the left, we show single-photon total cross section for pulses with $\sin^2$ envelope and duration of pulses $T = 1 fs$. We have performed 5 calculations, i.e. we have solve the TDSE for 5 different pulses centered at different frequencies. As explained in [60], one can extract information about the photoionization processes for

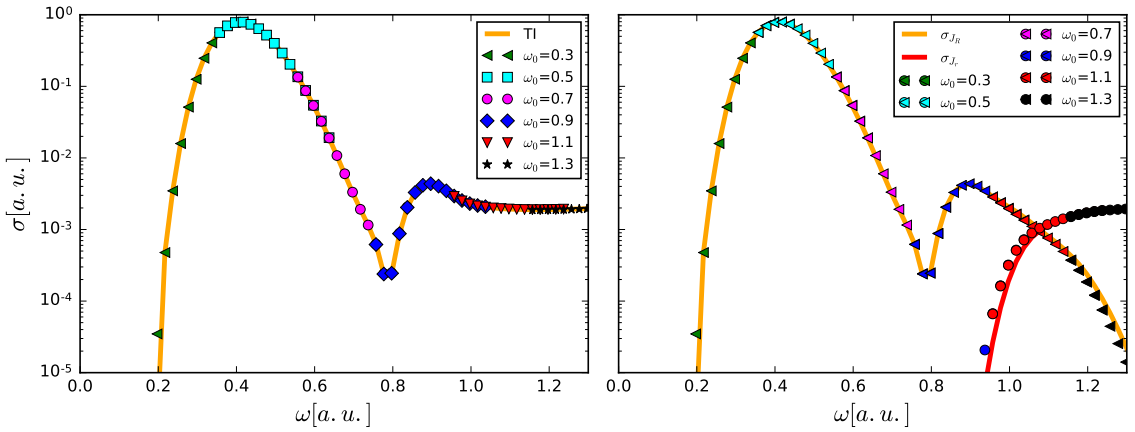

Fig. 5.10 Cross section from the time dependent quantum-mechanical flux method. The used pulses have $\sin^2$ envelope, intensity $I = 10^12W/cm^2$, and duration of $T = 1fs$. Left: the total cross section, calculated with a pulses with different central frequency ω_0 (in a.u.). Right: the cross section separated in dissociative ionization (triangles) and dissociative ionization (circles), for different central frequencies of the pulse, as indicated with different colors in legend.

those photon energies contained within the bandwidth of the pulse, therefore, with a reduced computational effort and from a single TDSE calculation, one can extract photoionization probabilities (cross sections) for a wide range of energies, as wide as the pulse energy bandwidth. The energy interval for each pulse is represented by a different color in figure 5.10. The bandwidth of the pulse $\Delta = \omega 2\pi/T$, determined by central frequency and pulse duration, define photon energy (ω) region $\omega_0 - \Delta\omega < \omega < \omega_0 + \Delta\omega$ where cross section can be extracted from. In the same figure, on the right, we show how, in time-dependent case (in the same way as in time-independent case), we can separate contributions to the total cross section in DE and DI by calculating $J_R\hat{\boldsymbol{R}}$ and $J_r\hat{\boldsymbol{r}}$ vector components of probability current vector, which is in good agreement with the results calculated in time-independent quantum-mechanical flux method. In this example, apart from central frequencies we have used the same pulses, but results are independent of a choice of pulse, and the total cross section can be calculated for any pulse.

5.4.2 Surface integral technique

The methods presented so far are just a benchmark for the method of central interest in this work: the *surface integral* technique. The surface integral technique provides the formal expressions to distinguish the contribution of the different channels (dissociation,

single and double ionization) and, thus, enables the calculation of total and partial breakup cross sections, resolved in energy of outgoing fragments, as well as the angular distributions of fragments. So far, this technique has been successfully implemented in single and double electron atoms, and in this work we demonstrate its extension to he simplest molecular system, H_2^+.

At the end of pulse the wave function $\Psi(t_{final})$ accounts for all correlation between all constituents, i.e. electron-nucleon and nucleon-nucleon correlation in H_2^+ system (example in figure 5.9), and with correlation introduced by a laser pulse still presented. By further (implicitly) propagating the wave function, with field-free Hamiltonian $\hat{\boldsymbol{H}}_0$, part of the wave functions that corresponds to total or partial breakup keeps spreading trough space, separating from a component corresponding to (localized) bound sates, and relaxing in eigenstates of $\hat{\boldsymbol{H}}_0$. These states (describing breakup) are orthogonal to (in general known) analytical solution (final states) for breakup problem and provide a way of extraction of breakup amplitudes by direct projection of the wave function to the final states. In atomic case of He atom (as in [20]), if the system is sufficiently propagated, for electron-electron correlation to be negligible, the double ionization amplitude can be extracted by projection of the final wave function $\Psi(t_{final})$ to the uncorrelated Coulomb final states, i.e. product of Coulomb functions for electrons in the attractive potential of $Z = 2$ charge. This can be further improved by propagating the system to $t \to \infty$, as done in the present method.

The great improvement of the method has been achieved by introduction of surface integral, where general transition amplitude 4.36, by using Green's theorem can be converted to surface integral, equation 4.25. In this way, the integration is performed only on a surface taken to be at large distances from origin. This allows us to use final states that are not *exact*, but rather good approximation to the final states, along integration surface. We call them the *testing functions*.

Our attempts have confirmed that (like in the in an atomic case) the electron-electron correlations can be neglected in the testing function, while electron-nucleon correlation in a molecular system cannot be neglected as noted in [82]. This is accounted by calculations of non-Coulomb contributions to the testing function, in equation 4.35. The non-Coulomb contributions is felt by the electrons even on large distances from moving nuclei, giving the electronic part of the total final state : $\Phi^{(+)}(\mathbf{k}$. We demonstrate that for the description of nuclear motion of the final state, the simple Coulomb function ($\Phi_c(R)$), in the repulsive potential of $Z = 1$ charge, for two proton system is good choice. So the total testing function ($\Phi_{k_n,\mathbf{k}_e}(R,\mathbf{r})$) can be written as

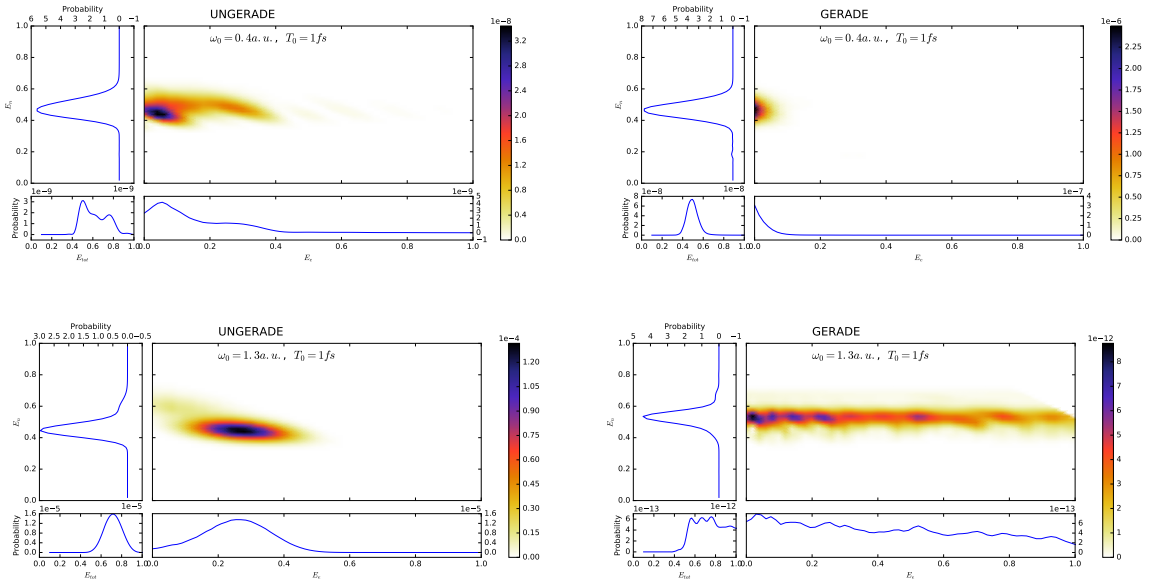

Fig. 5.11 Correlated kinetic-energy distributions for Coulomb explosion of H_2^+, calculated by TDSE and surface integral method. Used pulses with $\sin^2$ envelope, duration of pulses $T = 1fs$, central frequencies $\omega_0 = 0.4a.u.$ (up) and $\omega_0 = 1.3a.u.$ (down). Left: ungerade contribution, right: gerade contribution.

product of electronic part $\Phi^{(+)}(\mathbf{k})$ and internuclear $\Phi_c(R)$

$$\Phi_{k_n,\mathbf{k}_e}(R,\mathbf{r}) = \Phi_c(R;k_n)\Phi^{(+)}(\mathbf{r};\mathbf{k}). \tag{5.11}$$

The surface integral technique gives the complex amplitude ($f(k_n,\mathbf{k}_e)$) of transition probability ($P = |f(k_n,\mathbf{k}_e)|^2$) for finding the system in the final state defined by nuclear momentum k_n and electronic momentum $\mathbf{k}_e$ of ejected particles. If we are interested in transition to the final state of nuclear energy E_{k_n}, and electronic energy E_{k_e}, independent of ejection direction, we integrate transition probability over all possible ejection angles of electron (for protons the direction is fixed in z-direction), which gives the expression for energy probability distribution for Coulomb breakup:

$$P(E_{k_n},E_{k_e}) = \sum_{l_{k_e},m} \left| f_{l_{k_e},m}(k_n,k_e) \right|^2 . \tag{5.12}$$

In Fig. 5.11 we show energy probability distribution for two $\sin^2$ pulses, of $T = 1fs$ duration, and central frequencies $\omega_0 = 0.4a.u.$ (up) and $\omega_0 = 1.3a.u.$ (down). The expansion of the wave function in spherical harmonics, allows direct separation into gerade and ungerade components, and consequently separates one- from two-photon

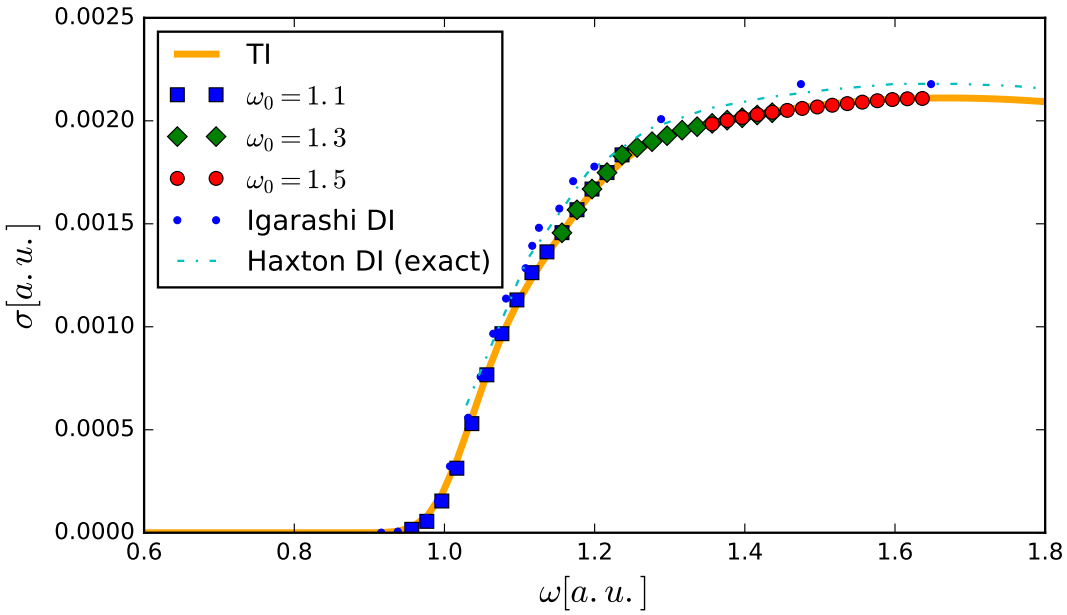

Fig. 5.12 Single photon dissociative ionization (DI) cross section by time dependent surface integral method, used pulses with $\sin^2$ envelope, duration of pulse $T = 1fs$ and central frequencies $\omega_0 = 1.1a.u.$ (blue squares), $\omega_0 = 1.3a.u.$ (green diamonds) and $\omega_0 = 1.5a.u.$ (red circles). Comparison with DI calculated by time independent quantum-mechanical flux method (orange full line), and data digitized form from references [31] (blue dots) and [26] (cyan line).

Coulomb breakup. For $\omega_0 = 0.4a.u.$ pulse, single-photon (ungerade) contribution, is almost two orders of magnitude lower than single-photon (gerade) component, which is in agreement with 5.8, where we can see that at photon energies $0.4a.u.$ Coulomb explosion is not energetically allowed. However, three-photon Coulomb explosion is also energetically accessible. For $\omega_0 = 1.3a.u.$ pulse we can see that single-photon absorption, is dominant mechanism in Coulomb explosion, not allowing absorption of the second photon.

From energy probability distribution, we can extract the total dissociative ionization (DI) cross section by integration of $P(E_{k_n}, E_{k_e})$ over energy conservation lines, defined by the total final energy of the system, $E_{tot} = E_{k_n} + E_{k_e}$, i.e. :

$$P(E_{tot}) \equiv \int_0^{E_{tot}} P(E_{k_n}, E_{tot} - E_{k_e}) dE_{k_n}. \tag{5.13}$$

This gives the total transition probability for DI, which by using the shape function [60] gives the single-photon cross section. The calculation of two-photon DI cross section

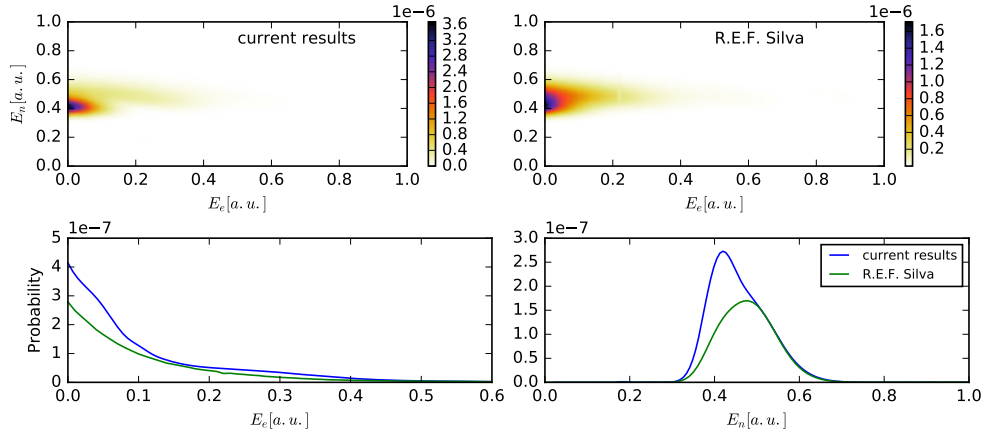

Fig. 5.13 Correlated kinetic-energy distributions ($P(E_n, E_e)$) (top), comparison with [75] (R.E.F. Silva). Used pulse: with $\sin^2$ envelope, duration of pulse $T = 0.5fs$ and central frequencies $\omega_0 = 0.6a.u.$. Comparison of correlated kinetic-energy (down), integrated by E_n (left), E_e (center) and energy conservation lines (left).

is also possible. In Fig. 5.12 we show, how in time dependent treatment treatment with surface integral technique, the total DI cross section is calculated by using pulses with different central frequencies. Each pulse gives the results for DI within its single-photon bandwidth (like in the time dependent quantum-mechanical flux method), which is in very good agreement with the previously presented time-dependent and time-independent methods.

In Figs. 5.13, 5.14, 5.15 and 5.16 we show comparison of energy probability distribution ($P(E_{k_n}, E_{k_e})$) (top,left) with [75] (top,right), for a pulses with $\sin^2$ envelope, central frequencies of $\omega_0 = 0.6$ and $\omega_0 = 0.8a.u.$ and different pulse durations. We can see good agreement between results obtained by two completely different methods. In bottom panel of each figure we can see comparison of energy probability distribution integrated over nuclear kinetic energy (left) and electron kinetic energy (right), where the agreement is more apparent.

From the complex transition amplitude ($f(k_n, \mathbf{k}_e)$) we can calculate angular distribution of outgoing electron. Electron momentum vector $\mathbf{k}_e$ defines the ejection angle θ, while in the current geometry $\phi = 0$. We define angular distribution as probability of ejection of electron into specific direction θ, integrated over all possible energies of electron,

$$P(E_{k_n}, \theta) = \left| \int_0^{E_{tot}} f(k_n, \mathbf{k}_e) dE_{k_e} \right|^2 . \tag{5.14}$$

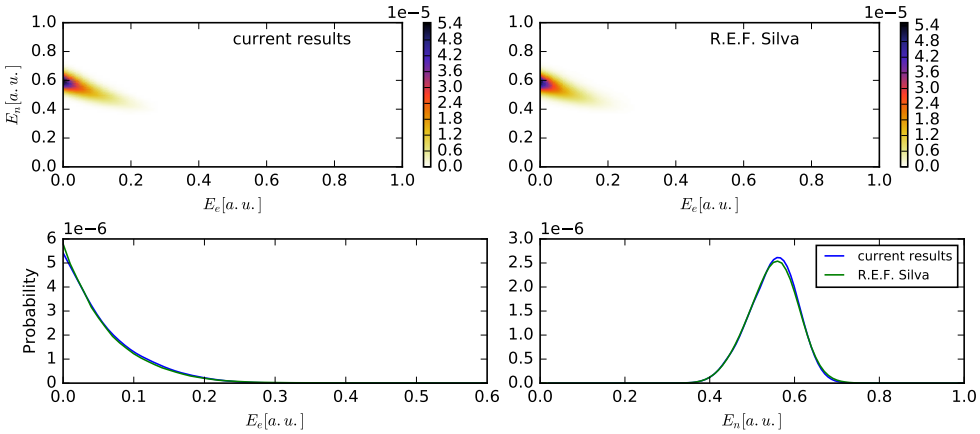

Fig. 5.14 Same as Fig. 5.13 but with $T = 2.5fs$, $\omega_0 = 0.6a.u.$.

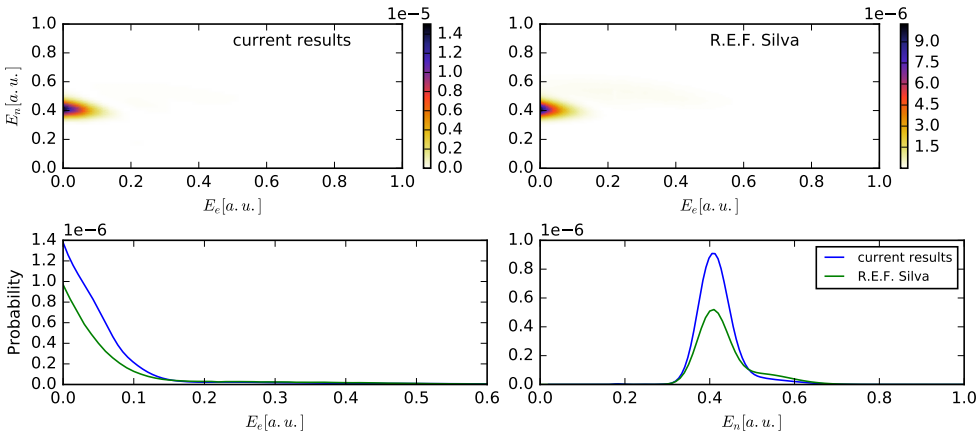

Fig. 5.15 Same as Fig. 5.13 but with $T = 0.76fs$, $\omega_0 = 0.8a.u.$.

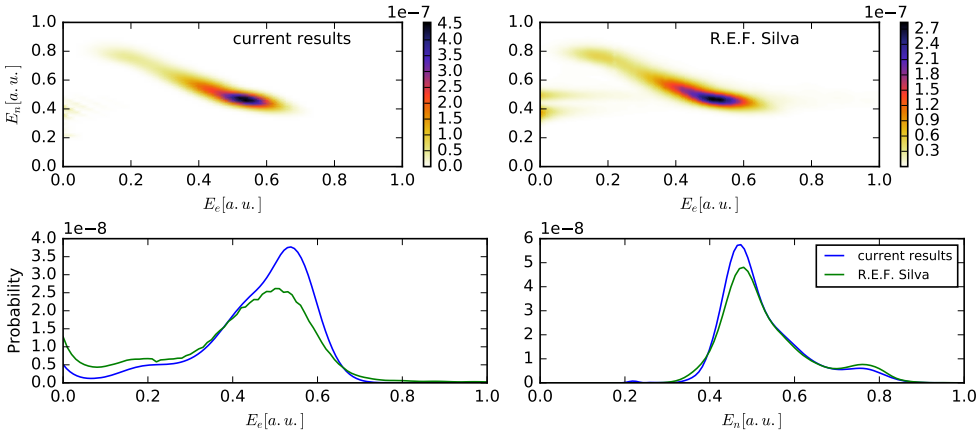

Fig. 5.16 Same as Fig. 5.13 but with $T = 2.5fs$, $\omega_0 = 0.8a.u.$.

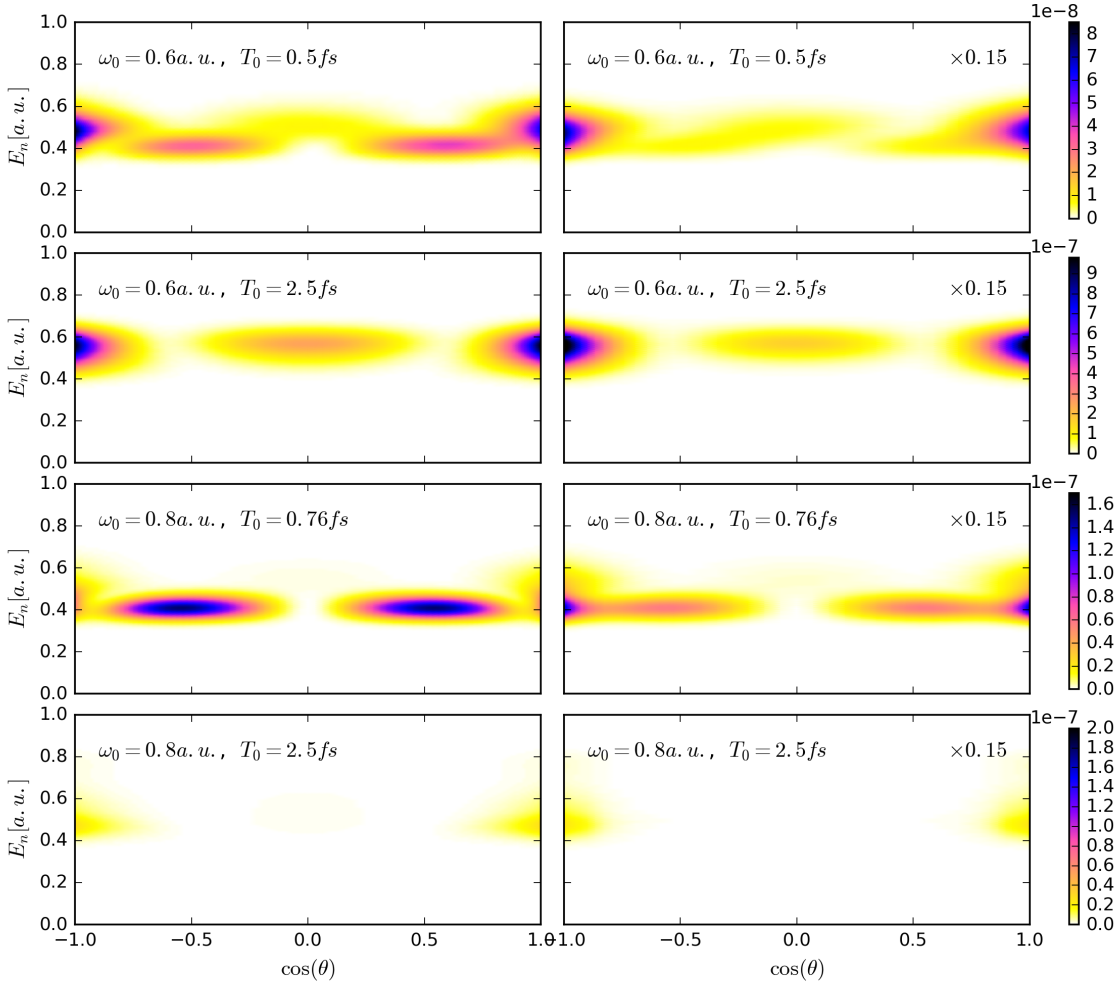

Fig. 5.17 Angular distributions ($P(E_{k_n}, \theta)$) calculated by surface integral method (left column), comparison with resolvent operator method [75] (right column), for different pulses. Data on the left are multiplied by indicated factor.

In Fig. 5.17 we show comparison of angular distributions with , [75] for the same pulses as previous four figures. The qualitative agreement, for this very sensitive calculation, can be seen, although not as good as in energy probability distribution.

Integration of the energy probability distribution, over electron energies, gives the nuclear kinetic energy release (KER) spectra shown in bottom right corner of Figs. 5.13, 5.14, 5.15 and 5.16. Selecting only gerade symmetry in the energy probability

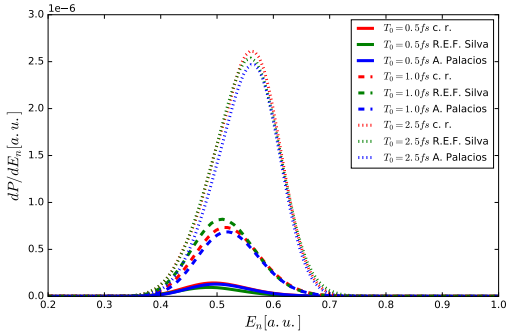

Fig. 5.18 Two-photon nuclear kinetic energy release spectra resulting from pulses with $\sin^2$ envelope, central frequency $\omega_0 = 0.6a.u.$ and pulse durations $T_0 = 0.5, 1.0$, and $2.5fs$, compared with resolvent operator method (R.E.F. Silva) in [75] and spectral method (A. Palacios) [58].

distribution, we get two-photon KER spectra, which is in Fig. 5.18 compared with [75] and [58], showing good agreement with both resolvent operator and spectral method.

The methods presented in this chapter give results that are in very good agreement with various data calculated with radically different methods. The shown results are already well know, but they gives us justification to introduce one more well known component: electron-electron interaction term, and get full-dimensional Hamiltonian, beyond the BO approximation for H_2 system. The results, demonstrating implementation of electron-electron interaction term are shown in the final chapter of this work.

Chapter 6

Imaging ultrafast molecular wavepackets with a single chirped UV pulse

The advent of free-electron-laser facilities and high-harmonic generation has opened the way to the production of intense and ultrashort ultraviolet (UV) pulses with durations in the femtosecond and attosecond range. One of the more awaited capabilities offered by such pulses is to use them to monitor and control electronic and nuclear dynamics, for example within a UV-UV pump-probe scheme, the so-called "holy grail" of attosecond physics. While some progress in this direction has been made [81, 87, 12, 11, 80], there are many technical challenges still to overcome, such as the limited intensity of the pulses and the fact that few optically active elements exist in the (extreme) ultraviolet. This precludes, for example, the use of pulse-shaping techniques and coherent control approaches that can be applied at optical and infrared frequencies to produce an "optimal" pulse for a desired photo-induced physical process or chemical reaction [3, 53, 84, 41, 9, 15, 17, 84, 57]. Consequently, most experiments performed so far with attosecond UV pulses rely instead on an intense infrared pulse for either the pump or the probe step, which can significantly distort the system and alter the dynamics. We present ab initio calculations performed in the H_2^+ molecule as a benchmark to demonstrate that by changing a single parameter, the spectral chirp of an ultrashort UV pulse, we can achieve a significant control over molecular multiphoton ionization, changing the total ionization yield by more than a factor of ten. More importantly, we show how to emulate a conventional pump-probe setup to obtain direct time-resolved imaging of ultrafast molecular dynamics. We introduce a simple model that can be applied to more complex molecular targets to retrieve the dynamical

information and validate its suitability by comparison with our ab initio simulations. The spectral chirp is experimentally tunable both in high harmonic generation and with free electron lasers [13, 72, 29, 7]. A similar idea was previously suggested by Yudin et al. [88], but only demonstrated for a superposition of two bound states in the hydrogen atom. In the present work, we aim at reconstructing the vibronic wave packet in a small molecule, simultaneously pumped and probed by a single chirped UV pulse.

At optical and infrared frequencies, the effect of frequency-chirped pulses has been actively investigated using theoretical approaches based on second-order time-dependent perturbation theory (TDPT) to treat few-photon excitation processes in atoms [1, 90, 22, 19, 53, 54, 14, 17, 78]. These methods have also been applied at ultraviolet frequencies, but, to our knowledge, only to describe the chirp-dependent photoelectron angular distributions in atomic photoionization [66, 65, 67]. In these approaches, only a limited number of states participate in the dynamics. In contrast, the additional nuclear degrees of freedom in molecular targets, as treated here, induce more complex wavepacket motion characterized by the participation of many vibronic states. We thus directly solve the full-dimensional time-dependent Schrödinger equation (TDSE), $i\frac{\partial}{\partial t}\Phi(t) = H(t)\Phi(t)$, using H_2^+ as a benchmark target to investigate the coherent manipulation of two-photon molecular photoionization by chirped pulses.

6.1 Parametrization of chirped pulse

The electromagnetic field $\mathbf{E}(t)$ of a (linearly polarized) chirped Gaussian pulse can be written as [88, 56, 65]:

$$\mathbf{E}(t) = \frac{1}{2}E_{\max}(\eta)F(t)\exp(i\phi(\eta,t))\mathbf{e}_z + c.c., \tag{6.1}$$

where the instantaneous phase is given by

$$\phi(\eta,t) = \omega_0 t - \frac{\eta}{2T_0^2(1+\eta^2)}t^2, \tag{6.2}$$

and the temporal envelope $F(t)$ is described by a Gaussian function:

$$F(t) = \exp\left(-\frac{t^2}{2T(\eta)^2}\right). \tag{6.3}$$

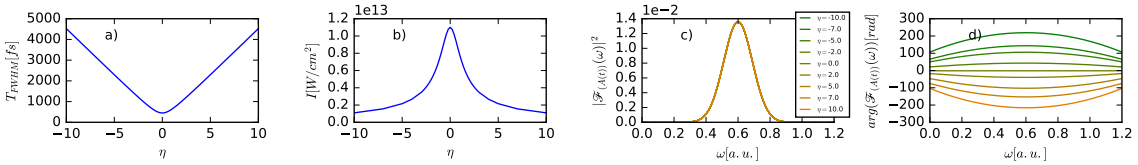

Fig. 6.1 Chirp parametrization for $\omega_0 = 0.6 a.u.$. Chirp η defines FWHM duration of the pulse a), and intensity b). The spectral distribution is independent of η c). Nonzero chirp introduces phase d).

The field amplitude, $E_{\max}(\eta)$, the pulse duration $T(\eta)$ and the instantaneous frequency $\omega(\eta, t) = \frac{\partial}{\partial t}\phi(\eta, t)$ explicitly depend on the chirp parameter η. Note that the spectral chirp (the quadratic term of the spectral phase) of the field defined here is directly proportional to η, but the temporal chirp (prefactor of the t^2 term in $\phi(\eta, t)$) has opposite sign in contrast with the definition in [88, 56, 65]. For unchirped pulses ($\eta = 0$), $E_{max}(\eta = 0) = E_0$ is the peak amplitude, T_0 defines the duration of the pulse (FWHM of the field envelope is $T_{\mathrm{FWHM}} = 2\sqrt{\log 4}\, T_0$), and ω_0 is the carrier frequency. The parametrization is chosen such that adding a chirp in frequency ($\eta \neq 0$), the spectrum remains unchanged. The duration of the pulse then increases to $T(\eta) = T_0\sqrt{1+\eta^2}$, while the peak amplitude decreases to $E_{\max}(\eta) = E_0/(1+\eta^2)^{1/4}$. In other words, the same frequencies are "stretched" over a longer duration. The Fourier transform of this Gaussian pulse leads to a Gaussian spectral function, with amplitude independent of η, but a spectral phase that is quadratic in ω with a spectral chirp given by $\eta T_0^2/2$.

The quantity that shows the time distributions of frequencies within a pulse is Wigner distribution function of the electromagnetic field, defined as:

$$W_E(t,\omega) = \int_{-\infty}^{\infty} E\left(t + \frac{\tau}{2}\right) E\left(t - \frac{\tau}{2}\right)^* e^{-2i\pi\tau\omega}\, d\tau. \tag{6.4}$$

In figure 6.2 we plot the Wigner distribution function for different chirp parameters, using the above-described parametrization. Right column in figure 6.2 a) are the Wigner distributions corresponding to the pulses plotted in the first column in the same figure. We have defined the pulses such that all the pules are centered at the central frequency ω_0 for $t = 0$. The chirp is defined with a spectral phase that varies quadratically in time, while the frequency distribution remains unchanged. The frequency distributions are thus identical for the three pulses shown in figure 6.2, middle column . As shown in the right column in figure 6.2, a non-zero positive value of the chirp parameter, η, introduces frequencies decreasing linearly with time, while a negative value introduces

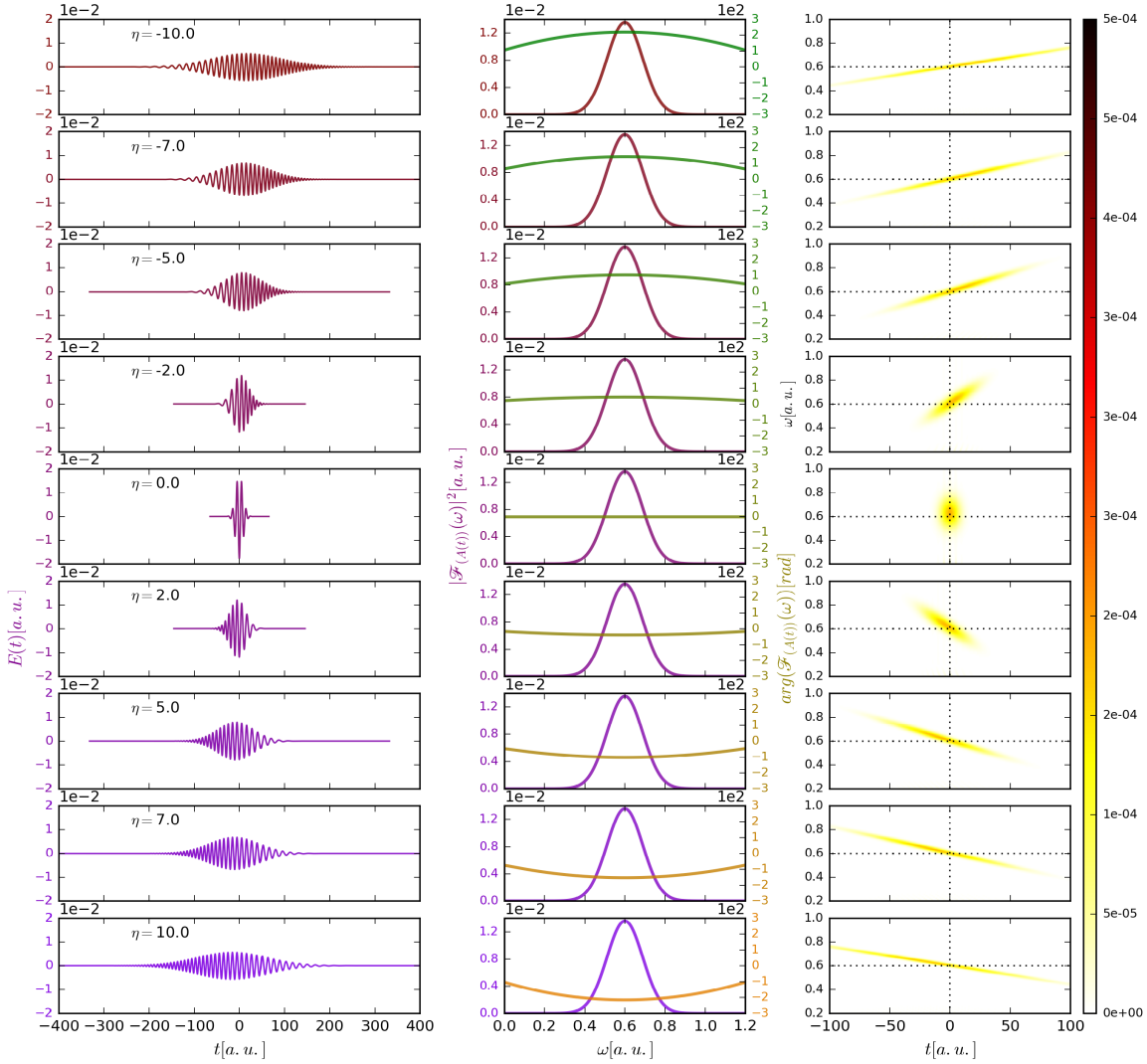

Fig. 6.2 Left column: electric field of the pulse. Middle column: Fourier transform, absolute value (left axis) and phase (right axis). Right column: Wigner distribution function. Each row correspond to the pulse for η indicated in the first colum.

equivalent increasing linear distributions. Even more, larger absolute value of the η parameter results in a smaller slope of the frequency distribution, while keeping spectrum intact (see figure 6.1 c) and d) and 6.9). In the following, we adopt a more intuitive terminology, referring to *down* chirp for pulses whose higher frequencies come earlier and lower frequencies come later (i.e., positive values of η), and *up* chirp to the pulses with the opposite sign.

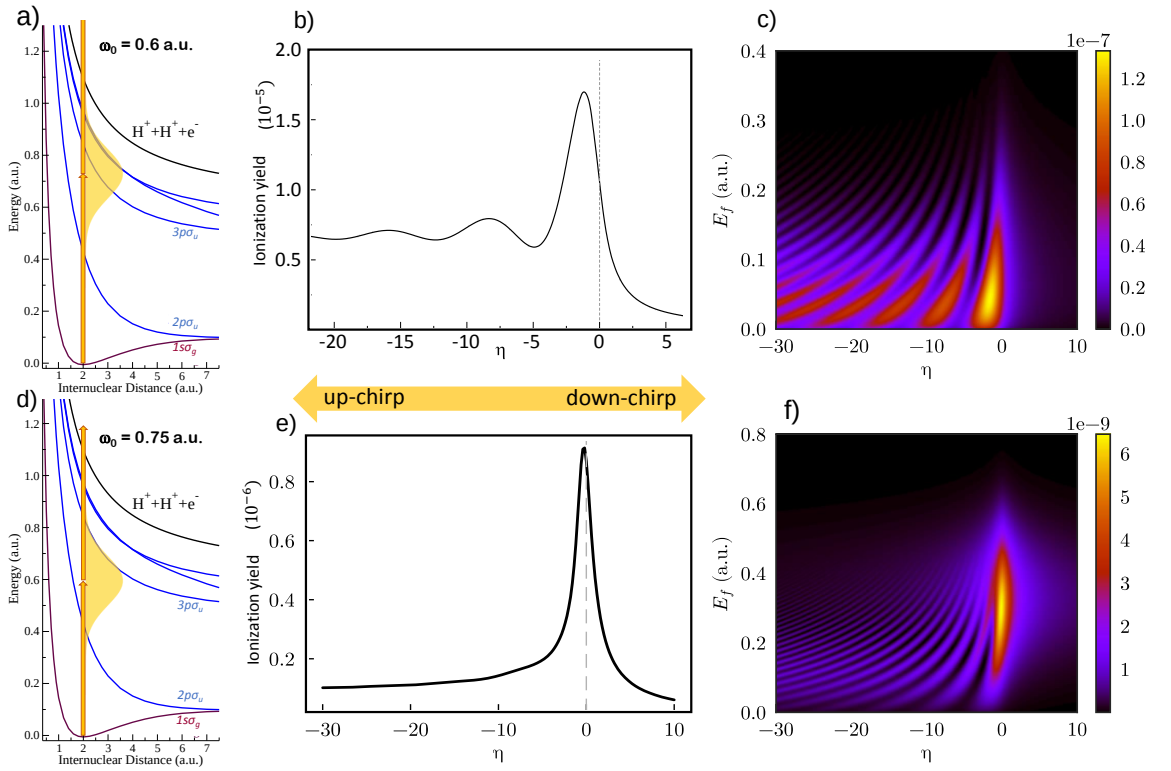

Fig. 6.3 Two-photon ionization probability for system in fixed nuclei approximation for chirped pulses with central frequencies $\omega_0 = 0.6$ a.u. (top) and $\omega_0 = 0.75$ a.u. (bottom). Left column: energetics of two-photon processes, with bandwidth of these pulses is plotted as an orange shadowed area. Center column: total two-photon ionization yield. Right column: photoelectron spectra.

6.2 Ionization yield enhancement and molecular decoherence

Despite the scarce number of applications using chirp attosecond pulses, there are some previous works using femtosecond pulses to explore two-photon excitation in atoms. For instance, in ref. [15], the authors employ a similar parametrization scheme for chirped femtosecond pulses to investigate excitation in a three-level system. This works shows that the excitation probability oscillates with the chirp parameter due to interferences between a two-photon direct and the two-photon (resonant) sequential paths. This results in an interference pattern in excited-state population, moreover it turns out that excited-state population can be manipulated by tuning the chirp of the employed pulse.

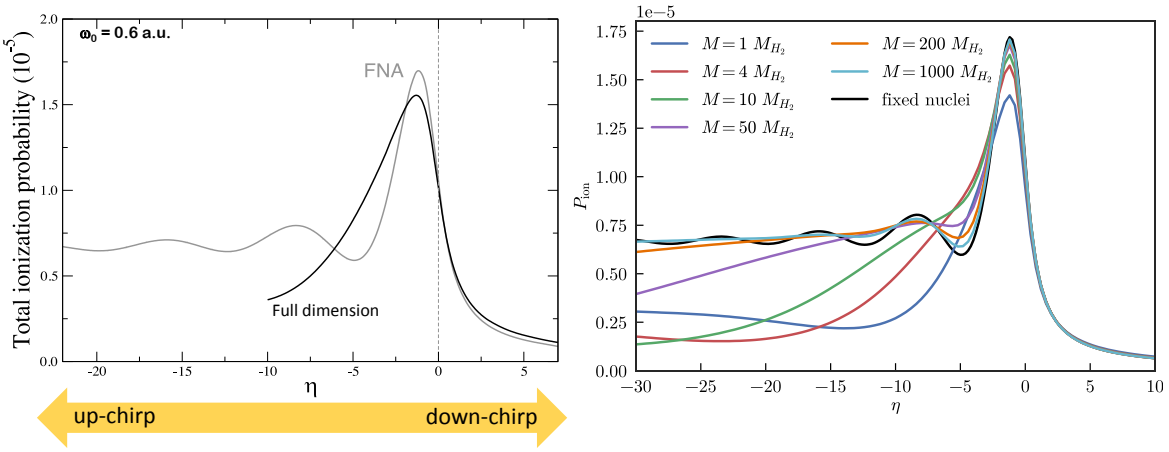

Fig. 6.4 Two-photon ionization probability chirped pulses with central frequencies $\omega_0 = 0.6$ a.u. Left: comparison of the full dimensional and FNA calculations. Right: simulation of nuclear motion where "effective" nuclear mass M is varied between FNA and nuclear motion limit and black line showing real FNA calculation.

In the present work, we employ attosecond pulses and investigate the possibility of controlling the two-photon ionization yield. Among the scarce (theoretical) works on attosecond chirp pulses, ionization has only been explored in atoms and in order to understand the effect of modifying the spectral phase variation in the angular distributions [67]. We here investigate the use of chirped attosecond pulses as an alternative to pump-probe techniques to map the ultrafast electronic and nuclear dynamics, analyzing total and energy-differential ionization probabilities. Moreover, to our knowledge, there is no existing works in molecules, thus we aim to elucidate the role of nuclear motion on the chirp-induced effects. We use pulses whose frequency spectra correspond to that one of an unchirped pulse ($\eta = 0$) with a FWHM duration of 450 as centered at $\omega_0 = 0.6$ a.u. and $\omega_0 = 0.75$ a.u. and a laser intensity of 1.1×10^{13} W/cm^2. First we the compute the two-photon ionization probability for H_2^+ system in fixed nuclei approximation (FNA), where the two nuclei are fixed at equilibrium internuclear distance $R = 2a.u.$. For an appropriate choice of photon energy, interplay of different quantum paths is present, reflecting atomic nature of FNA. For the $0.6a.u.$ (upper row in) and the $0.75a.u.$ (lower row) of central frequencies of the pulse, within the FNA, figure 6.3 a) and d) illustrate the energetics involved in the process. Figure 6.3 b) and e) show the total ionization yields as a function of the chirp parameter. And figure 6.3 c) and f) correspond to the photoelectron spectra. A photon energy of $0.6a.u.$ lies in between the first two excited states of H_2^+

($2p\sigma_u$ and $3p\sigma_u$). The total ionization yield (figure 6.3 b) oscillates as a function of the chirp parameter. These are interferences associated to the interplay between a two-photon direct ionization path and the two-photon resonant path through the $2p\sigma_u$ state. These are analogous results as those found in [15] for two-photon excitation with femtosecond pulses. Interestingly, we observe that the total yield varies almost in an order of magnitude as the chirp parameter changes. The maximum yield is reached at a value of $\eta = -1.4$, i.e. for an up chirped pulse where the lower frequencies (in resonant wit the $2p\sigma_u$ state) reach the molecule earlier in time. As we move to positive values of chirp, down-chirp, the ionization yield strongly decreases since we are moving towards the non-resonant limit. On the other hand, as we move to more negative values of chirp, the oscillations vanishes reaching the limit of the two-photon resonant contribution. In contrast with the previous findings in [15], the oscillations are fading out for more negative values, while for the two-photon excitation problems this oscillating patterns survive. In order to understand this behavior, one should look at a more detailed observable: the photoelectron spectrum as a function of the chirp parameter (figure 6.3 c)). Note that we are working in the FNA, therefore the same behavior will be found in photoionization of atomic targets. For a given final energy of the ejected electrons, oscillations do not fade out, but they are well-defined. However, since the total ionization implies an integral over all electron energies the oscillatory pattern is smoothed out. We also perform calculations for pulses centered at $0.75a.u.$, a scenario far from resonance. The total ionization yields for pulses centered at $0.75a.u.$ are shown in figure 6.3 e). We see that the interference patterns disappear, and the total yield decreases smoothly. This is due to the fact that the maximum of the ionization probability now is shifted up in energy as shown in figure 6.3 f). There is no longer a low photoelectron energy cut-off, as for the $0.6a.u.$ pulse. Consequently, although the two-photon paths interferences are still observable for a given final energy, integration over all electrons energies cancels out leading to a smooth behavior of the total yield as a function of the chirp parameter. This is a consequence of the presence of a final continuum, i.e. it is a feature associated to the photoionization event that is absent in two-photon excitation. Once the role of an electronic continuum is understood, we move to the effect of the nuclear degrees of freedom.

The results of the full dimensional calculations are plotted in figure 6.4. We repeat the calculation for a central frequency of $0.6a.u.$. For comparison, we include in the figure the FNA results taken from figure 6.4 b). First, we observe that the nuclear motion still allows for a great degree of control of the total ionization yield with the chirp parameter. However, we observe that the interference patters are completely

washed out. This is expected since including the nuclear motion introduces a continuum of energies in the intermediate states. In order to confirm this origin, we simulate the effect of including different relative motion of the nuclei. In the model, we reduce the simulation to a single electronic state, the $2p\sigma_u$, and then include different values for the nuclear masses. The results are plotted in figure 6.4 b). We obtain the model for different values of effective nuclear masses, as we increase the nuclear mass we approach the limit of the fixed nuclei approximation as expected. We confirm that the lightest masses are responsible for the smoothed out of the interference patters in the total ionization yields.

More interesting, we will now analyze the energy-differential ionization yields that are expected to imprint the dynamical information associated to the one-photon transition. Our premise is the following: we use chirped pulses such that the lower frequencies are in resonance with the lower excited states of the molecule. The higher frequencies come later and photoionize the molecule. Therefore, one expects to catch the evolution of the dynamics triggered by the lower frequencies and being probed in the fully-energy differential probabilities by the higher frequencies. In other words, we simulate an scheme similar to a pump-probe scheme where the pumping and probing frequencies are introduced within a single pulse and where the delay among them is given by the chirp parameter. We then analyze the full-dimensional calculation using a central frequency of $\omega_0 = 0.6$ a.u., where ionization is solely due to two-photon absorption paths. The energy bandwidth of these pulses is visible in 6.7 a) as an orange shadowed area is centered at $0.6 a.u.$, lying in between the $2p\sigma_u$ and $3p\sigma_u$ states. In 6.7 a) we show the potential energy scheme of the two-photon ionization process, where we use linearly polarized light parallel to the molecular axis of the H_2^+ molecule. The one-photon transition from the $1s\sigma_g$ ground state creates a vibronic wave packet in the dissociative excited states of σ_u symmetry. The two-photon transition reaches the ionization potential leading to the Coulomb explosion of the system ($H^+ + H^+ + e^-$).

As expected, the excitation probability, shown in 6.7(b), is independent of the chirp parameter. As illustrated by Brumer and Shapiro [10], the one-photon absorption probability is "*an emperor without clothes*", unaffected by the spectral phase, and only depends on the (chirp-independent) spectral frequency distribution of the pulse. The spectral phase introduced in the excited wave packet can only be captured in a second-order process, for instance the two-photon transition depicted in 6.7, where the time evolution of the nuclear wave packet is retrieved through its projection into the electronic continua. The excitation probabilities associated to the $2p\sigma_u$ and $3p\sigma_u$ states, which are independent of η, are plotted as a function of the vibronic

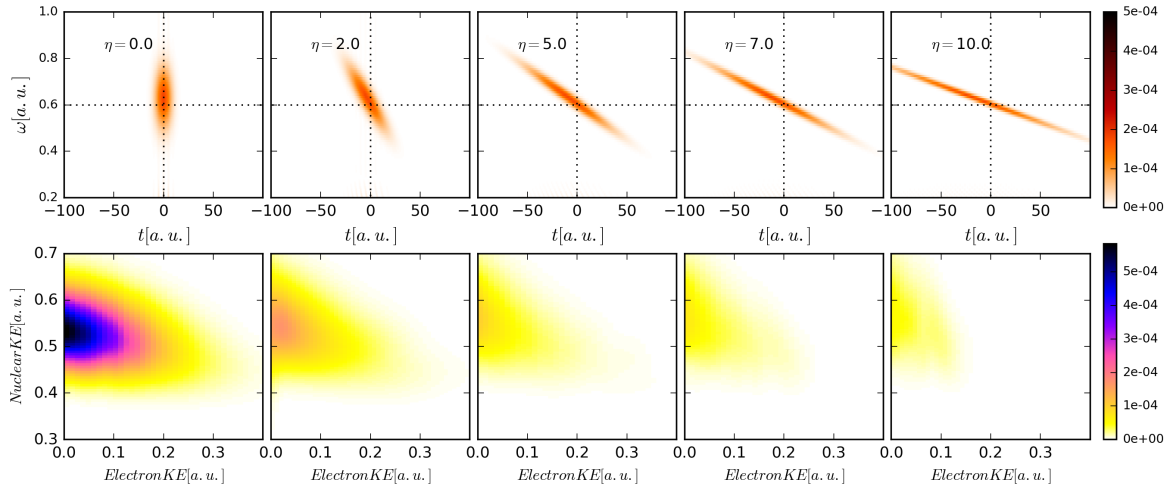

Fig. 6.5 Two-photon fully differential energy distribution for *down* chirps. Upper row: Wigner distribution functions. Lower row: Fully differential energy distributions for the ionized fragments after Coulomb explosion (x-axis: electronic energy, y-axis: nuclear energy).

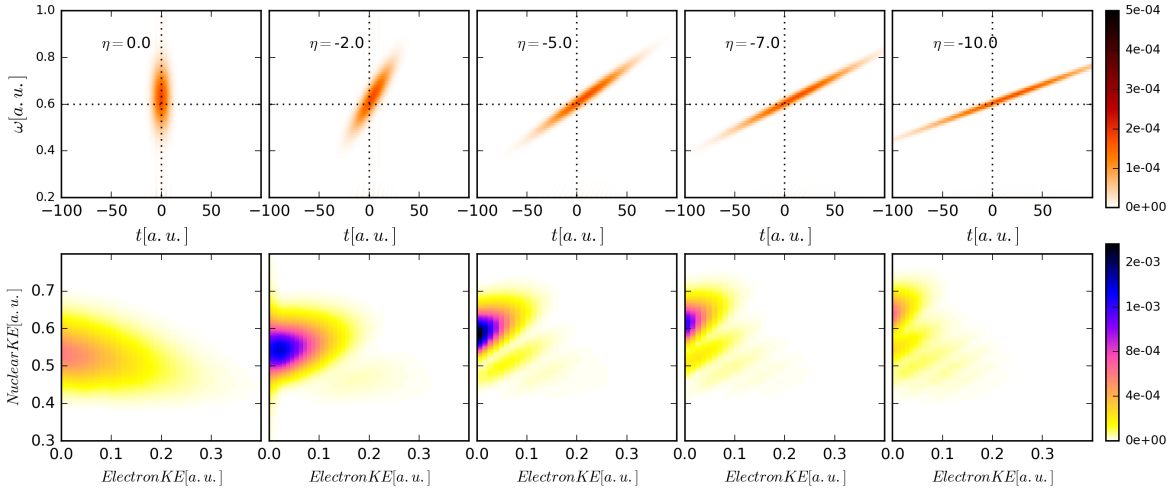

Fig. 6.6 Two-photon fully differential energy distribution for *up* chirps. Upper row: Wigner distribution functions. Lower row: Fully differential energy distributions for the ionized fragments after Coulomb explosion (x-axis: electronic energy, y-axis: nuclear energy).

(vibrational+electronic) energy in 6.8. For the pulses employed here, we can see that the two-photon ionization proceeds almost entirely through the first excited state. First, the photon energies within the pulse are energetically closer to the resonant vertical transition from the ground state to the $2p\sigma_u$ state. In addition, the dipole

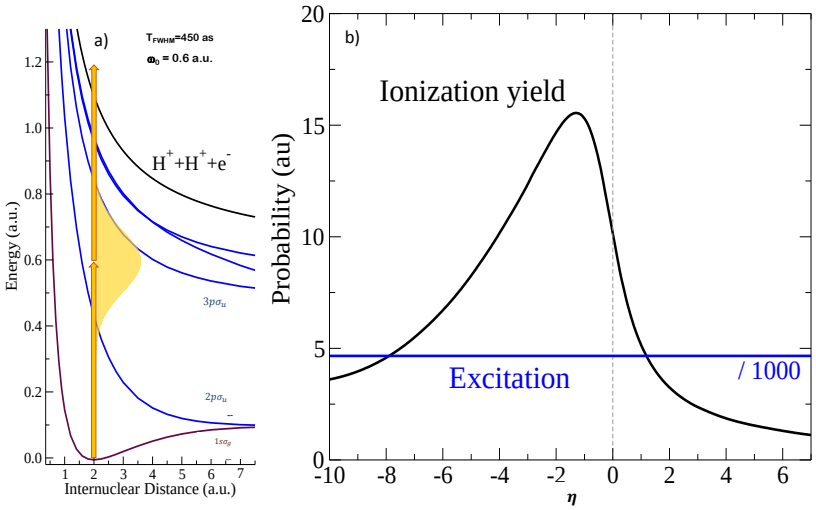

Fig. 6.7 (a) Energy scheme with the relevant potential energy curves: ground state of $H_2^+(1s\sigma_g)$ in violet, first four excited states of σ_u symmetry in blue and the Coulomb explosion potential in black. The energy bandwidth of the pulses employed in the present work is plotted in an orange shadowed area in the region where the one-photon absorption occurs, centered at 0.6 a.u. and covering an energy range around 0.4-0.8 a.u. The blue shadowed area indicates the Franck-Condon region. (b) Two-photon ionization (black) and one-photon excitation (blue) yields as a function of the chirp parameter η.

coupling to the $3p\sigma_u$ state is noticeably weaker than that to $2p\sigma_u$, resulting in three orders of magnitude smaller one-photon excitation probability to the $3p\sigma_u$ state than that to the $2p\sigma_u$ state (see figure 6.8).

The total ionization probability as a function of the η parameter is also included in 6.7(b). Ionization to the final states of Σ_g symmetry (even number of absorbed photons) is the dominant process, while the ionization to states of Σ_u symmetry (odd number of absorbed photons) is negligible. As shown in the figure, by tuning the chirp parameter the total ionization probability can be strongly modified, with a modulation range of more than an order of magnitude. At the H_2^+ equilibrium distance where dynamics is mostly initiated, the energy difference between the ground and the $2p\sigma_u$ state is 0.43 a.u., while the difference between the latter and the Coulomb explosion potential energy curve is 0.67 a.u.. It is thus expected that the total ionization yield is enhanced for negative values of η (up chirp), i.e. when lower frequencies ($<$0.6 a.u.) arrive earlier and larger frequencies ($>$0.6 a.u.) arrive later. In this way, both transitions, from the

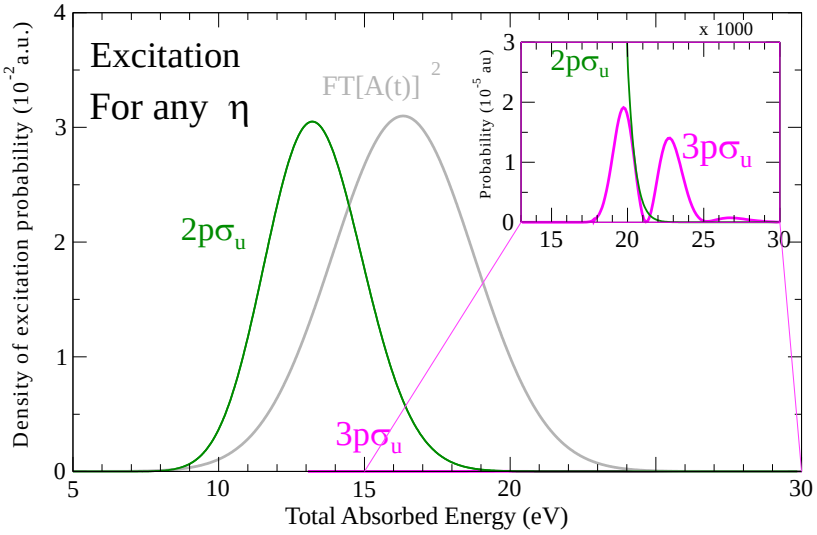

Fig. 6.8 One-photon excitation distributions as a function of the total absorbed energy for the two lowest excited states $2p\sigma_u$ (green) and $3p\sigma_u$ (red).

ground state to $2p\sigma_u$ and from $2p\sigma_u$ to the Coulomb explosion, can take place when the instantaneous frequency is close to resonant, thus maximizing ionization.

6.3 Reconstruction of vibronic wave packet

In order to extract dynamical information about the excited wave packet associated to the $2p\sigma_u$ state, we will study the energy-differential ionization probabilities for different values of the chirp parameter, shown in figures 6.5 and 6.6. In the upper row of 6.9, we plot the Wigner distribution functions of the electromagnetic field, which provides a combined time-frequency representation, for three different pulses with $\eta = 0$, -5 and -10. For the unchirped pulse, all frequencies reach the target simultaneously. However, for the chirped pulses, the more negative η (up chirp) the larger the time delay between the lower and the higher frequencies. In other words, by making η more negative, we are creating a nuclear wave packet in the $2p\sigma_u$ starting at earlier times (the direct vertical transition at 0.43 a.u. occurs earlier), which is probed by promotion into the Coulomb explosion channel at later times (frequencies around 0.67 a.u. arrive later). Therefore, this is conceptually equivalent to standard pump-probe schemes, where two time-delayed pulses are employed: one pulse launches the dynamics in the target and a second pulse, delayed (and ideally not overlapping) in time, probes the

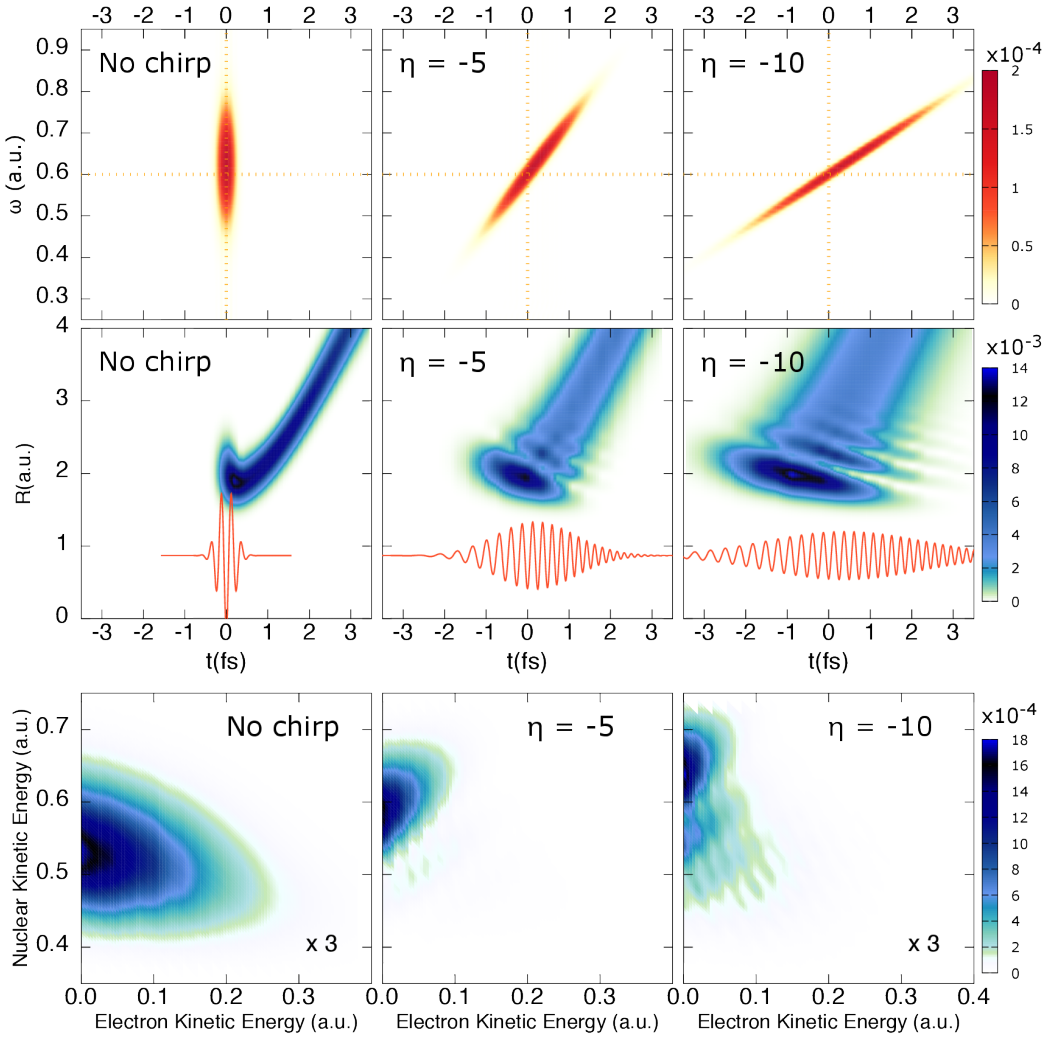

Fig. 6.9 Results for three different values of the chirp parameter ($\eta = 0$, -5, and -10 as labeled in each subplot). Upper row: Wigner distribution functions. Middle row: Nuclear wave packet associated to the $2p\sigma_u$ excited state as a function of time. The electromagnetic field of the pulse, $E(t)$, is included for each η (red line). Lower row: Fully differential energy distributions for the ionized fragments after Coulomb explosion (x-axis: electronic energy, y-axis: nuclear energy).

pumped dynamics through promotion to a given final state. In the present case, the time delay is encoded in the chirp parameter.

The middle panels of 6.9 show the corresponding nuclear wave packets (NWPs) in the $2p\sigma_u$ state as a function of time (x-axis) and internuclear distance (y-axis). In the same subplots, we include the electromagnetic field, $E(t)$, as a red line. We can see that the quadratic spectral phase associated to a given chirp value ($\eta \neq 0$) introduces

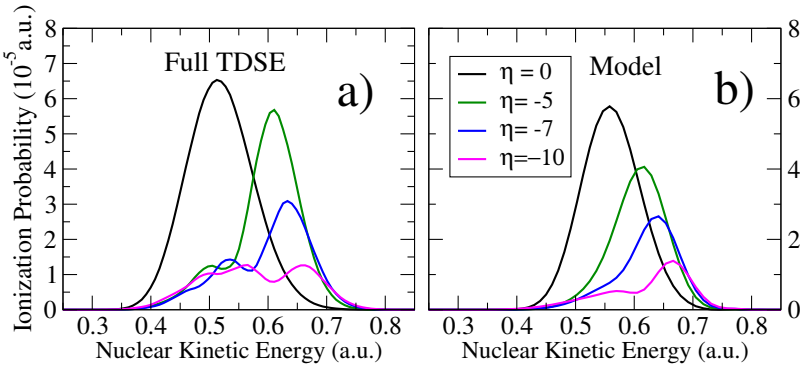

Fig. 6.10 Ionization probability as a function of the nuclear kinetic energy release for different values of the chirped parameters (see legend), extracted from the full dimensional calculation solving the TDSE (a) and extracted from the "sequential" model based on second order time-dependent perturbation theory as explained in the text (b).

structure in the pumped excited wave packet. This is due to interferences resulting from different frequency components with different spectral phases [15]. We observe nearly the same wave packet, but stretched in time. As discussed above (cf. 6.8, the energy distribution of the wave packet is identical for all values of η. However, as seen in 6.9, their spatial structure differs, since for the more negative (up) chirp , the same frequencies are reaching the target with a larger delay between them. This structured wave packet is mapped into the energy differential ionization probabilities upon absorption of a second photon, leading to distinct profiles.

The energy-differential ionization probabilities are shown in the contour plots in the bottom panels of 6.9, as a function of the ejected electron energy (x-axis) and the nuclear kinetic energy release of the nuclei (y-axis). The energy distribution resulting from the interaction with the unchirped pulse is smooth, while the chirped pulses yield distributions shifted towards higher nuclear kinetic energies and with internal structure. For a better visualization, we integrate the ionization probabilities over the electron kinetic energy and obtain the nuclear kinetic energy distributions shown in 6.10(a). Here, we have additionally included the results for $\eta = -7$. These energy distributions actually reflect the dynamics launched in the excited molecule. In order to prove this, in 6.10(b), we show the results of a sequential model where the excited NWP created in the $2p\sigma_u$ state by the lower frequencies is directly projected into the ionization channel. Note that the model qualitatively reproduces the position and the profile of each energy distribution. The model uses as starting point the exact second-order time-dependent

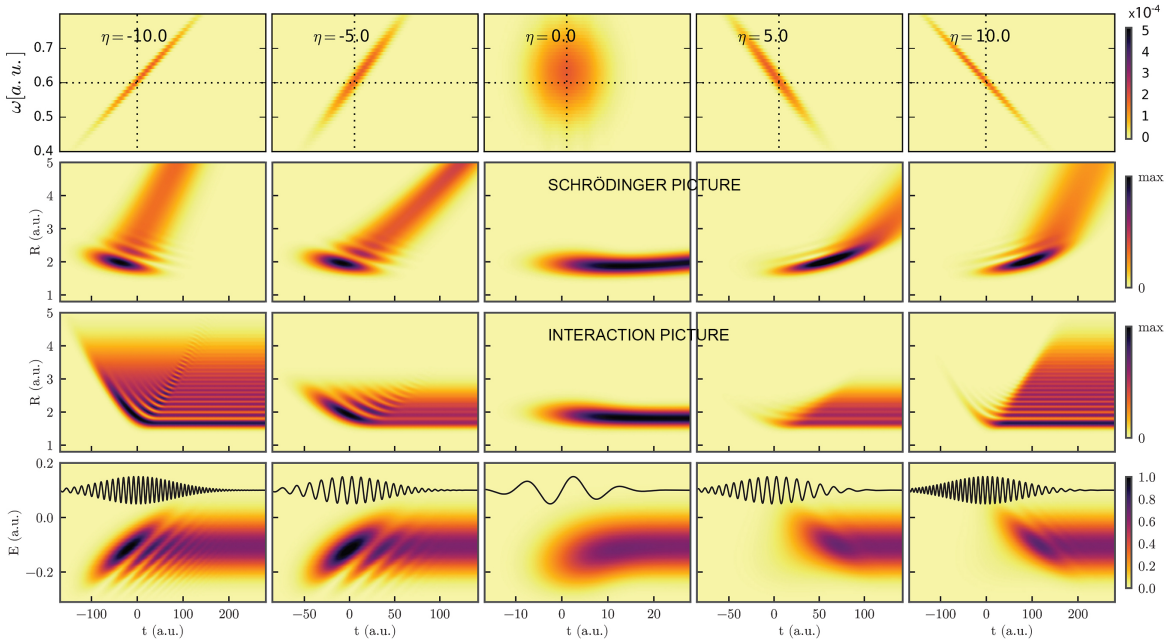

Fig. 6.11 Nuclear wave packets evolution. Top row: Wigner distribution functions for pulses with different η indicated in the legend. Second and third row: evolution of nuclear wave packets for $2p\sigma_u$ state in Schrödinger and interaction picture, respectively. Bottom row: evolution of energy distributions in interaction picture.

perturbation theory expression for the molecular wave packet, $\Psi_I^{(2)}(t)$, created after two-photon absorption from the ground state, Ψ_0. In the interaction picture, it is given by

$$|\Psi_I^{(2)}(t)\rangle = \frac{1}{i}\int_{-\infty}^{t} dt' \hat{V}_I(t')|\Psi_I^{(1)}(t')\rangle, \tag{6.5}$$

$$|\Psi_I^{(1)}(t')\rangle = \frac{1}{i}\int_{-\infty}^{t'} dt'' \hat{V}_I(t'')|\Psi_0\rangle, \tag{6.6}$$

where $\hat{V}_I(t) = e^{iH_0t}V(t)e^{-iH_0t}$ is the driving operator in the interaction picture. The ionization amplitude can be obtained by simply projecting the molecular wave packet, $|\Psi_I^{(2)}(t)\rangle$, into the final continuum states, leading to the ionization probabilities in the bottom panel of 6.9. The first-order wavepacket $|\Psi_I^{(1)}(t')\rangle$ corresponds to the nuclear wavepacket after one-photon absorption, as shown in the middle panels of 6.9. Note that those NWPs are plotted in the Schrödinger picture and consequently evolve in time even in the absence of the field. In figure 6.11, second and third row show the time evolution of NWP in Schrödinger and interaction picture, respectively. In the interaction picture, the wavepackets remain unchanged in time once the frequency components of the

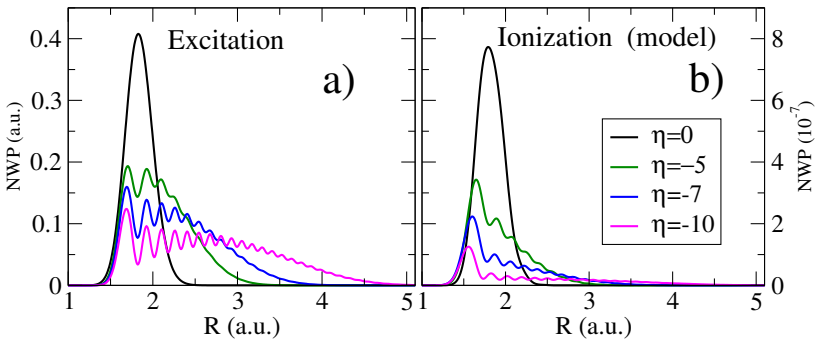

Fig. 6.12 Nuclear wave packets as a function of internuclear distance for different values of η indicated in the legend. (a) Ab initio calculated excitation nuclear wave packet in the interaction picture at the end of the pulse. (b) Mapping of the excitation wave packet plotted on the left into the Coulomb explosion potential energy curve using the model explained in the text.

driving pulse that are responsible for the transition have been absorbed. The ab initio first-order wavepackets at $t \to \infty$ are shown in 6.12(a). For up chirps, these wavepackets are already fully formed when the second (higher-frequency) photon is absorbed (see figure 6.11, third row). We can thus use a sequential approximation where the final first-order wavepacket (with $t \to \infty$) is used as the source for the second-order wavepacket:

$$|\Psi^{(2)}_{\text{seq}}(t)\rangle = \frac{1}{i}\int_{-\infty}^{t} dt' \hat{V}_I(t')|\Psi^{(1)}_I(t' \to \infty)\rangle. \tag{6.7}$$

The result of this approximation is plotted in 6.12(b), where we can see how the structure of the excited wave packet in 6.12(a) is reflected in the ionized wave packet extracted from the model. By using the definition of $\hat{V}_I(t)$ and 6.1, the corresponding ionization amplitude, i.e. the projection of the approximated second-order wave packet into the final states, $c_f = \langle f|\Psi^{(2)}_{\text{seq}}(t \to \infty)\rangle$, can be written as:

$$c_f \propto \sum_n a_{fn} a_{ni} e^{-i\frac{\eta T_0^2}{2}\left[(\omega_{fn}-\omega_0)^2+(\omega_{ni}-\omega_0)^2\right]}, \tag{6.8}$$

where $a_{jk} = \langle j|z|k\rangle|\tilde{E}(\omega_{jk})|$ is the product of the dipole matrix elements involving the ground i, intermediate n and final states f with the chirp-independent spectral amplitude of the pulse at the corresponding transition frequencies $\omega_{jk} = E_j - E_k$, and where $\tilde{E}(\omega) = \int_{-\infty}^{\infty} E^+(t)e^{i\omega t}\mathrm{d}t$ results from a Fourier transform of $E^+(t)$ [the

c.c. part in 6.1]. The exponential in 6.8 corresponds to the spectral phase of the field. The good agreement between the ionization probabilities resulting from this model [shown in 6.10(b)], and the ab initio ones [6.10(a)] validates the use of the sequential approximation to map the wave packet generated by the chirped pulse. More interestingly, 6.8 demonstrates the close relation between the current approach and conventional pump-probe setups [21, 59]. In such schemes, the two transitions are driven by two different pulses separated by a time delay Δt, leading to the analog expression for the ionization amplitudes, $c_f^{\mathrm{PP}} \propto \sum_n a_{fn}^{(2)} a_{ni}^{(1)} e^{-iE_n\Delta t}$, but with an important difference: For the single chirped pulse, the relative phase depends quadratically on the intermediate state energy E_n, while it does linearly in a pump-probe scheme. However, if the transition amplitude to intermediate states is peaked around an average value $\bar{E}_n$ (as in the present case, cf. 6.8, we can bridge this difference and make the analogy even more apparent. Expanding the energy of the intermediate states around this value, $E_n = \bar{E}_n + \delta_n$, one obtains

$$c_f \propto \sum_n a_{fn} a_{ni} e^{-i\delta_n \Delta t_\mathrm{e} - i\eta T_0^2 \delta_n^2} \simeq \sum_n a_{fn} a_{ni} e^{-i\delta_n \Delta t_\mathrm{e}}, \tag{6.9}$$

where $\Delta t_\mathrm{e} = (\bar{\omega}_{ni} - \bar{\omega}_{fn}) T_0^2 \eta$ corresponds to an effective time delay, defining $\bar{\omega}_{ni} = \bar{E}_n - E_i$ and $\bar{\omega}_{fn} = E_f - \bar{E}_n$, and the quadratic term can be neglected for sufficiently small δ_n. It can be easily shown that for large enough η the effective time delay matches the difference between the times when the instantaneous frequency $\omega(\eta, t)$ is resonant with the average transition energies $\bar{\omega}_{ni}$ and $\bar{\omega}_{fn}$. In summary, these expressions demonstrate that, within the validity of the sequential approximation, the chirped pulse acts like a conventional pump-probe setup, but with an effective time delay given by an average energy difference of the transition of interest.

In conclusion, we have shown that two-photon ionization of molecules can be manipulated by using frequency-chirped femtosecond pulses, leading to modulations of the ionization probability of more than an order of magnitude. We have also shown that chirped pulses can be used to probe the ultrafast molecular dynamics triggered in the excited molecule by just varying the frequency chirp, which is equivalent to varying the time delay in the long awaited UV pump-UV probe schemes. This has been demonstrated by using chirped pulses with the same energy spectrum and a quadratic spectral phase, which as shown in previous works [13, 72, 29, 7], can be easily reproduced in the lab. In this scenario, the energy distribution of the wave packet created by one-photon absorption does not vary with the chirp parameter, while the spatial distribution does. This can be retrieved from its direct mapping into the energy

distribution of the charged fragments after Coulomb explosion, and is shown to be formally analogous to a conventional pump-probe scheme. Although applied to H_2^+ in the present work, the method should also be suitable to probe wave packet dynamics in excited states of more complex molecules. It will not only be easier to implement than UV pump-IR probe methods, where two different pulses must be synchronized, but it will also avoid the significant distortion introduced by the IR probing.

Chapter 7

Double ionization of H_2

In this chapter, we present our most recent results on double photoionization of the hydrogen molecule in order to benchmark our numerical implementation. In the theory section, we have provided a complete description of the methodology including all electronic and nuclear degrees of freedom. In the following, we describe the technical details of the methodology to extract single and double ionization yields, total and differential in energy and angle, for the two-electron diatomic target, H_2. The methodology can provide a reliable description of multiple ionization by absorption of one or several photons in relatively intense fields. In this chapter, we present our benchmark results comparing with previous data when available. To date, we have obtained results within the fixed nuclei approximation, with the two nuclei fixed at the equilibrium distance, $R = 1.4a.u.$. Forthcoming simulations that include the nuclear degrees of freedom are straightforward with the current implementation.

In one-photon double ionization of H_2 molecule, it has been shown that fixed-nuclei is a good approximation [83, 82], when the two electrons are ejected instantaneously not allowing nuclear motion during the process. The two-photon ionization can occur through a sequential process in which one electron is ejected by absorption of first photon, and the second electron is later ejected by absorption of the second photon. If the time delay between the absorption of two photons is long enough to allow nuclear motion, the fixed-nuclei is not good approximation anymore. For photon energies larger than $31eV$ (the energy difference between the H_2^+ ground state and the H_2 double ionization continuum), only sequential process is allowed, and fixed-nuclei approximation gives a realistic results. The nuclear motion can be introduced by inclusion of electron-nuclear interaction, extensively investigated chapter 5, leaving us only a step from implementation capable to accurately describe non-sequential processes.

Initially in the ground state, the system is irradiated by a lineally polarized laser field with polarization parallel to the molecular axis (in figure 7.4 we include perpendicular polarization as well). A fully dimensional description of H_2 system, even in absence of nuclear motion, is computationally very expensive resulting in calculations limited to shorter boxes. We examine one-photon single and double ionization in time-independent LOPT approach and one- and two-photon single and double ionization by solving TDSE.

7.1 Bound states

The computation of the bound states of the H_2 molecule by comparison with existing data provides a good test to validate the construction of the field-free Hamiltonian. The diagonalization of the field-free Hamiltonian (equation 2.8) yields the wave functions and energies of the bound states. The ground state of the H2 molecule is a singlet state of $\Sigma_g symmetry$. The interaction with light considered in this work cannot initiate a transition from the *singlet* to *triplet* states, allowing calculation to be restricted to *singlet* configuration only. Using explicitly symmetric basis functions 3.8 presented in section 3.2 gives direct separation of singlet and triplet states, or consequently, symmetric and anti-symmetric parts of wave function in coordinates space, thus reducing size of the problem and removing any contributions from triplet states. In absence of an external perturbation, *parity* and the total angular momentum (M) are good quantum numbers, allowing calculations for each parity (gerade or ungerade) and each M (Σ, Π, Δ ...) to be preformed separately, therefore further reducing size of the problem.

In single center expansion, that we are using, where radial part of the wave function is expanded in FEM-DVR basis and angular in coupled spherical harmonics, see section 3.2, convergence in FEM-DVR parameters is easily achieved, compared to convergence in l_{max} parameter for the bound states of the neutral molecule with the maximum angular momenta, l_max. We plot the result of our simulations obtained for a total symmetry of the system Σ and Π and compare with the most accurate data provided in the literature by Wolniewicz and collaborators [86] and [85]. Figure 7.1 shows the results obtained with different values of angular momenta ($l_{max} = 3, 5$ and 7) for the two lowest bound states of Σ_g, Σ_u, Π_g and Π_u states. The agreement with the accurate values reported by Wolniewicz et al. [86] and [85], is excellent for short nuclear distances ($< 4a.u.$), while it becomes poor as the nuclei are placed far away. The larger the angular momenta the larger the internuclear distances for which the agreement

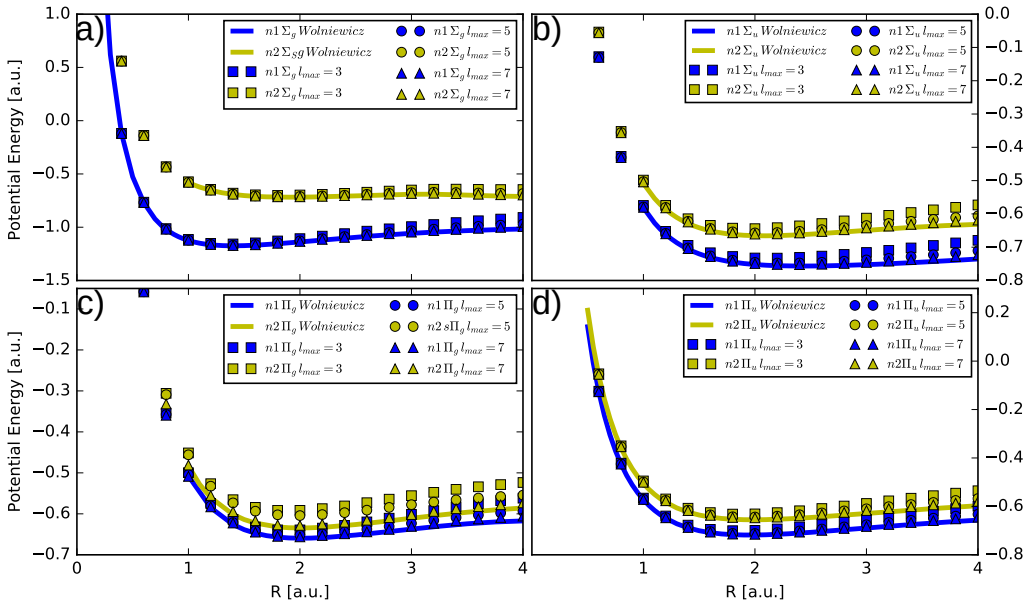

Fig. 7.1 Potential energy curves for two lowest electronic sates of H_2 molecule in each symmetry. Each panel corresponds to a given total symmetry of the system: a) Σ_g, b) Σ_u, c) Π_g and d) Π_u. Comparison with data from [86] and [85] (full lines). Convergence with l_{max} parameter is designated by different plot markers.

holds. This is an expected result because of the lack of spherical symmetry. For the energy of the ground state at the internuclear distance, $R = 1.4a.u.$, we obtain an energy of energy of $E_0 = -1.17342$ for relatively small $l_{max} = 9$, which is in reasonable agreement with the very precise value of $E_0 = -1.174475668$ as reported in [37].

The solution of equation 3.18 thus provides energies and their corresponding eigenvectors, i.e. expansion coefficients. In our implementation, evaluation of the wave function at any point of space is straightforward. The wave functions are plotted in figure 7.2, where we have integrated the probability distribution over all angular coordinates (Ω_1, Ω_2), on left. We can see localized wave function in $r_1 - r_2$ subspace but no details on internal structure, We thus plot the wave function as a function of the radial coordinates for electron 1 (x-axis) and electron 2 (y-axis) for the equilibrium internuclear distance (figure 7.2 on right), where we clearly see effect of electron-electron repulsion as minimum along $r_1 = r_2$ line.

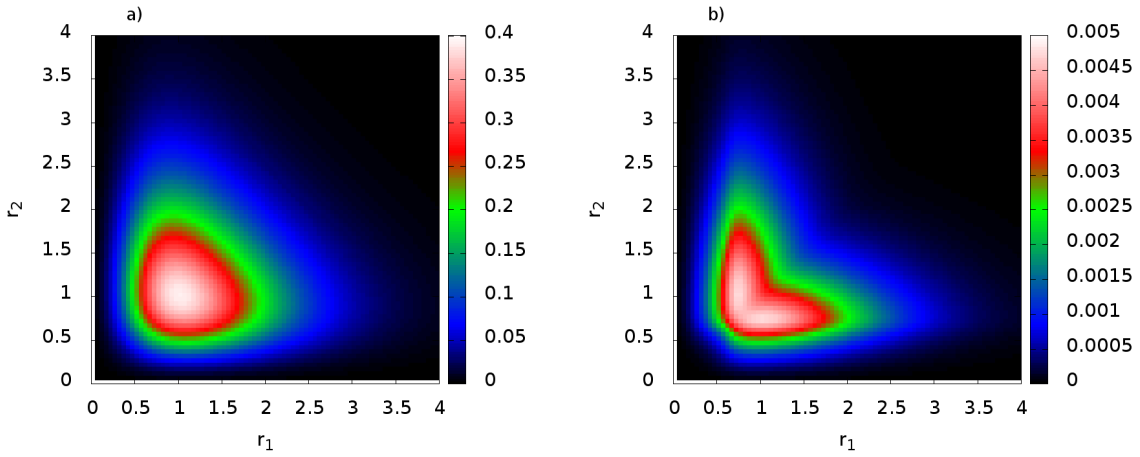

Fig. 7.2 Ground state probability distributions, $|\Phi(r_1, r_2, \hat{\boldsymbol{r_1}}, \hat{\boldsymbol{r_2}})|^2$, for $R = 1.4 a.u.$, $l_{max} = 10$, FEM-DVR grid:[0. 0.6 1.5 5. 10.], DVR-order=15. a) integrated over all angular coordinates ($\hat{\boldsymbol{r_1}}$ and $\hat{\boldsymbol{r_2}}$) b) evaluated on (half of) internuclear axis ($\hat{\boldsymbol{r_1}} = \hat{\boldsymbol{r_2}} = \hat{\boldsymbol{z}}$).

7.2 Time-independent LOPT approach

The time-independent lowest-order perturbation theory (LOPT) accurately describes physical situation where laser pulses are very long and monochromatic with narrow spectral bandwidth and of moderate intensities [30]. We use LOPT to calculate the one-photon double ionization in H_2 molecule in FNA, that we will be latter compared with nonperturbative TDSE results. We assume the molecular system in its ground state. The interaction with the light is written within the dipole approximation. The scattering wave function for one-photon absorption ($\Psi_{sc}^{(+)}$) is calculated from the driven Schrödinger equation 4.2 with ECS which imposes correct boundary conditions. In this section we use different methods to extract physical observables, in particular, we will use the optical theorem (section 7.2.1) and the quantum-mechanical flux method (section 7.2.2) to calculate the one-photon single ionization total cross section, for calculation of angular distributions of outgoing electrons we will use surface integral technique in section 7.2.3.

7.2.1 Optical theorem

The first method that we use to compute the total one-photon absorption cross section is optical theorem, presented in section 4.1.1. Computationally less expensive, for each photon absorption optical theorem involves only one operation of dipole operator over the wave function. Optical theorem provides one-photon absorption probability in the

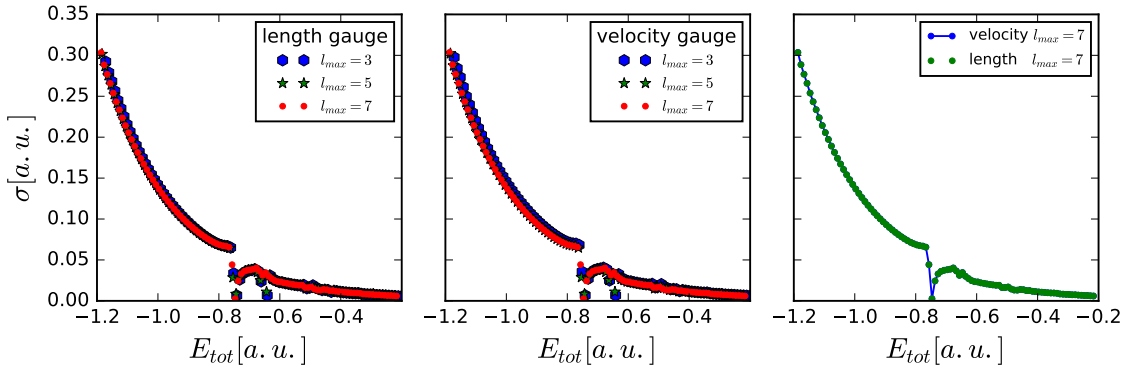

Fig. 7.3 One-photon single-ionization (SI) cross section by optical theorem for H_2 in fixed nuclei approximation and parallel polarization of light. Left: convergence in l_{max} parameter for length gauge. Center: convergence in l_{max} parameter for velocity gauge. Right: comparisons of convergence in l_{max} between gauges.

lowest order of time-independent perturbation theory (LOPT), therefore comparable to nonperturbative time-dependent calculations for long pulse durations and moderate intensities. In addition to field-free Hamiltonian, optical theorem provides test of accuracy of dipole operator implementation. The key point in the method is ECS that imposes correct boundary conditions, which is imposed on both electronic coordinates equally. It is also possible to extend time-independent LOPT within ECS formalism to two-photon absorption processes as demonstrated in [55].

We consider system initially to be in the ground sate of Σ_g symmetry, irradiated by linearly polarized electromagnetic field parallel and perpendicular to the molecular axis. Parallel polarization preserves cylindrical symmetry of the system, initiating one-photon absorption process transition to Σ_u state. In perpendicular polarization and one-photon absorption, dipole selection rules require final state to be in Π_u symmetry.

The calculated cross sections contains all possible photo-absorption contributions, which in case of H_2 molecule includes single- and double-ionization. Optical theorem does not provide a direct way to separate these contributions, therefore in this section we focus on the energy region where double-ionization is not accessible, i.e. $E_{tot} = E_0 + \omega < 0$, where E_{tot} is the total energy of the system, E_0 is ground state energy and ω photon energy.

In figure 7.3 we show convergence in l_{max} of one-photon cross section, computed by optical theorem, in single-ionization energy region for parallel polarization of light (final sate of Σ_u) symmetry. On left we see convergence in length gauge, central plot shows convergence in velocity gauge, comparison on the right shows that velocity gauge

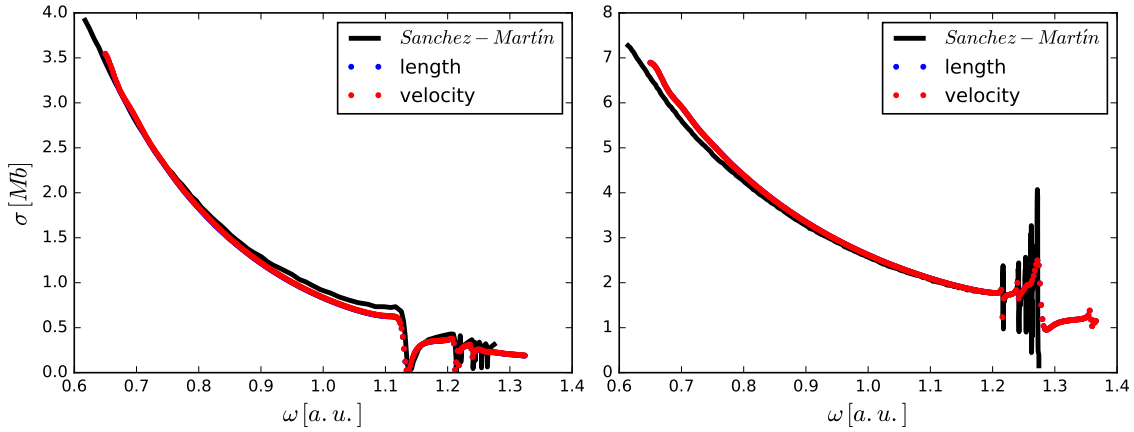

Fig. 7.4 One-photon SI cross section by optical theorem for H_2 in fixed nuclei approximation, in length (blue dots) and velocity (red dots) gauge. Left: Final state of Σ_u symmetry. Comparison with SI cross sections from [45] (yellow line) and [69] (black line). Right: Final state of Π_u symmetry.

converges faster that length gauge and that for $l_{max} = 7$ convergence is already reached. Figure 7.4 shows one-photon single-ionization cross section for both parallel (left) and perpendicular (right) polarization of lights and comparison with the data from [45] and [69], which shows good agreement taking into account that in optical theorem we have all one-photon absorption contributions (including excitation).

7.2.2 Quantum-mechanical flux

Although, time-independent quantum-mechanical flux method for LOPT (presented in 4.1.2), for total cross section for one-photon absorption, does not provide additional information with respect to the optical theorem method, it involves the integral over the hypersurface, thus providing a convenient test for the implementation of multiphoton absorption and for double ionization problems. Moreover, the definition of the flux allows one, first to select a given final energy of the system, and second, to restrict the integrals in separated regions to distinguish different breakup channels. Such distinction can only be accurately achieved by means of the surface integral approach through the definition of the proper testing functions associated to a well-defined breakup channel, nevertheless the extraction of the flux already provides a good quantitative estimation of the relative contribution of the different channels.

The same formalism discussed for the H_2^+ system in section 5.3.2, can be easily generalized to be applied to the H_2 molecule. The two electrons, as undistinguisable particles, can be treated defining the same electronic coordinates and simplifies the

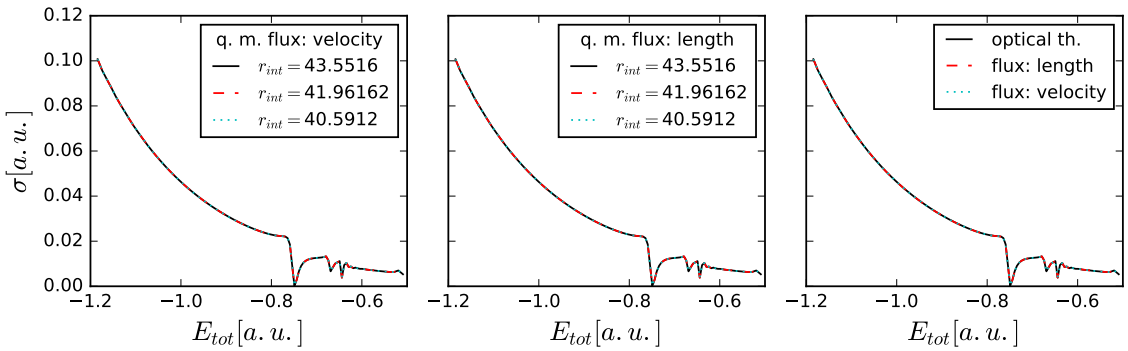

Fig. 7.5 One-photon SI cross section by time-independent quantum-mechanical flux for H_2 in fixed nuclei approximation. Left: convergence with r_{int} parameter in velocity gauge. Center: convergence with r_{int} parameter in length gauge. Right: comparison of quantum-mechanical flux with optical theorem method. Used $l_{max} = 9$.

choice of the integration hypersurface given in equation 4.9. As for the H_2^+ target, we integrate over every angular coordinates and chose appropriate integration curve in $r_1 - r_2$ radial subspace. Because of computational advantages, as mentioned in section 5.3.2 we choose rectangular surface instead of circular one used in literature, defined by:

$$\begin{aligned} L1 &: r_1 \in [0, r_{int}],\ r_2 = r_{int},\ \hat{\boldsymbol{n}} = \hat{\boldsymbol{r_2}} \\ L2 &: r_2 \in [0, r_{int}],\ r_1 = r_{int},\ \hat{\boldsymbol{n}} = \hat{\boldsymbol{r_1}}, \end{aligned} \tag{7.1}$$

where parameter r_{int} is chosen to be in non-ECS region, typically a few FEM-DVR grid points below ECS region.

In figure 7.5 we show the single photon single ionization cross sections obtained with the flux method. We plot the results computed in velocity (left) and length gauge (middle panel) for the different choice of the integration radius r_{int} in equation 7.1. We observe that convergence is fully achieved, results for different integration radius are undistinguisable. On the right panel, we show the excellent agreement of the results of each gauge in comparison with the outcome of the optical theorem (already shown to be gauge-independent).

7.2.3 Angular distributions

In this section, we focus on the numerical checks for the implementation of the surface integral technique described in the theory section 4.2.2. This method is a formal approach that enables the extraction of the double ionization yields (total, energy and

angle-differential) from scattering wave function computed ether in LOPT or TDSE. The existing works on H_2 double ionization are still scarce and only performed within fixed nuclei approximation, for one-photon [83] and [55, 24, 32] two-photon double ionization. Therefore, here we test our implementation against existing data. We first describe the specific implementation to treat one-photon double ionization of the hydrogen molecule. The formalism extracts double ionization yields from the previously computed scattering wave function at a given energy, it is thus equivalent for one- or multi-photon absorption processes. The difference for one- and two-photon absorption comes from the scattering wave function that we are extracting information from.

In surface integral, in equation 4.22, we use the scattering wave function $\Psi_{sc}^{(-)}$, computed by the time-independent driven equation 4.2, instead of time-deponent in equation 4.16. We use the same single-electron testing function as for H_2^+ system, given by equation 4.26. For two electron system, we use the product of two uncorrelated single-electron testing functions, properly expressed in coupled symmetrized basis that we are using. If we write single-electron testing function as:

$$\Phi^{(+)}(\mathbf{k},\mathbf{r}) = \sum_{l_k,l,m} \varphi_{l_k,l,m}(r) Y^*_{l_k,m}(\hat{\mathbf{k}}) Y_{l,m}(\hat{\mathbf{r}}), \tag{7.2}$$

uncorrelated product of testing function for two electron system in uncoupled spherical basis is:

$$\begin{aligned}\Phi_{(t)}(\mathbf{k}_1,\mathbf{r}_1,\mathbf{k}_2,\mathbf{r}_2) \equiv \Phi^{(+)}(\mathbf{k}_1,\mathbf{r}_1)\Phi^{(+)}(\mathbf{k}_2,\mathbf{r}_2) = \\ \sum_{l_{k_1},l_1,m_1} \sum_{l_{k_2},l_2,m_2} \varphi_{l_{k_1},l_1,m_1}(r_1) Y^*_{l_{k_1},m_1}(\hat{\mathbf{k}_1}) Y_{l_1,m_1}(\hat{\mathbf{r}_1}) \varphi_{l_{k_2},l_2,m_2}(r_2) Y^*_{l_{k_2},m_2}(\hat{\mathbf{k}_2}) Y_{l_2,m_2}(\hat{\mathbf{r}_2}).\end{aligned} \tag{7.3}$$

To express two-electron testing functions in coupled symmetric basis, we project uncorrelated product in 7.3 to the basis given by equation 3.15.

$$\begin{aligned}\langle \Phi_{(t)}(\mathbf{k}_1,\mathbf{r}_1,\mathbf{k}_2,\mathbf{r}_2) | \Psi^{i_1,l_1,i_2,l_2}_{L,M} \rangle = \sum_{l_{k_1},m_1,l_{k_2},m_2} Y_{l_{k_1},m_1}(\hat{\mathbf{k}_1}) Y_{l_{k_2},m_2}(\hat{\mathbf{k}_2}) \\ \sum_{i'_1,i'_2,l'_1,l'_2} a_{i'_1,l_{k_1},l'_1,m_1} a_{i'_2,l_{k_2},l'_2,m_2} \langle i'_1, i'_2; l'_1, l'_2, m_1, m_2 | i_1, i_2; l_1, l_2, L, M \rangle_s ,\end{aligned} \tag{7.4}$$

where subscript $_s$ indicates coupled and symmetrized (ket state) basis function, $a_{i,l_k,l,m}$ are expansion coefficients of radial part of single-electron testing functions in FEM-DVR

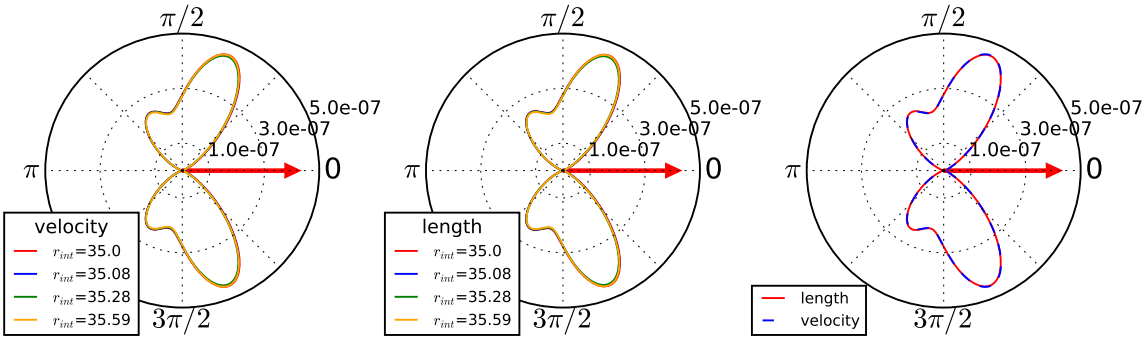

Fig. 7.6 One-photon double ionization of H_2 for a photon energy of $\omega = 2.75 a.u.$: triple differential probabilities within the fixed nuclei approximation obtained with the surface integral method. The red arrow indicates the outgoing direction of the fixed electron while polar plot represents angular distribution of probability of detection of second electron (black curve). We pick an 50% energy sharing of the total available energy between the electrons. Left: convergence with r_{int} parameter in velocity gauge. Center: convergence with r_{int} parameter in length gauge. Right: comparison of length and velocity gauges.

basis, given by:

$$\varphi_{l_k,l,m}(r) = \sum_i a_{i,l_k,l,m}\chi_i(r). \tag{7.5}$$

Projection factor in 7.4 can be evaluated by writing testing function in coupled spherical basis for $\hat{\mathbf{r}_1}$ and $\hat{\mathbf{r}_2}$, while keeping it uncoupled for $\hat{\mathbf{k}_1}$ and $\hat{\mathbf{k}_2}$:

$$\begin{aligned}
&\langle i_1', i_2'; l_1', l_2', m_1, m_2 | i_1, i_2; l_1, l_2, L, M\rangle_s = \\
&= \sum_{L',M'} \langle l_1', l_2', m_1, m_2 | l_1', l_2', L', M'\rangle \langle i_1', i_2'; l_1', l_2', L', M' | i_1, i_2; l_1, l_2, L, M\rangle_s \\
&= \sum_{L',M'} \langle l_1', l_2', m_1, m_2 | l_1', l_2', L', M'\rangle \langle i_1', i_2'; l_1', l_2', L', M' | \times \\
&\quad \left[|i_1, i_2; l_1, l_2, L, M\rangle + (-1)^{l_1+l_2-L} |i_2, i_1; l_2, l_1, L, M\rangle\right] A^{i_1,l_1,i_2,l_2}_{L,M} \\
&= \langle l_1', l_2', m_1, m_2 | l_1', l_2', L, M\rangle \times \\
&\quad \left(\delta_{i_1',i_1}\delta_{i_2',i_2}\delta_{l_1',l_1}\delta_{l_2',l_2} + (-1)^{l_1+l_2-L}\delta_{i_1',i_2}\delta_{i_2',i_1}\delta_{l_1',l_2}\delta_{l_2',l_1}\right) A^{i_1,l_1,i_2,l_2}_{L,M},
\end{aligned} \tag{7.6}$$

where $\langle l_1', l_2', m_1, m_2 | l_1', l_2', L', M'\rangle$ is Clebsch-Gordan coefficient and $A^{i_1,l_1,i_2,l_2}_{L,M}$ is normalization factor in coupled symmetrized basis (3.9). In forth line we have written coupled symmetrized basis ($|\rangle_s$) explicitly. Inserting it back to the expression for projection of

testing function to symmetrized basis element (in equation 7.4), follows:

$$\begin{aligned}\langle\Phi_{(t)}(\mathbf{k}_1,\mathbf{r}_1,\mathbf{k}_2,\mathbf{r}_2)|\Psi_{\substack{i_1,l_1,i_2,l_2\\L,M}}\rangle = &\sum_{l_{k_1},m_1,l_{k_2},m_2} Y_{l_{k_1},m_1}(\hat{\mathbf{k}_1})Y_{l_{k_2},m_2}(\hat{\mathbf{k}_2})\\ \times\Big(&a_{i_1,l_{k_1},l_1,m_1}a_{i_2,l_{k_2},l_2,m_2}\,\langle l_1,l_2,m_1,m_2|l_1,l_2,L,M\rangle +\\ &a_{i_2,l_{k_1},l_2,m_1}a_{i_1,l_{k_2},l_1,m_2}\,\langle l_2,l_1,m_1,m_2|l_2,l_1,L,M\rangle\,(-1)^{l_1+l_2+L}\Big)A_{\substack{i_1,l_1,i_2,l_2\\L,M}}.\end{aligned} \tag{7.7}$$

Now we can write two-electron testing function in coupled symmetric basis as:

$$\Phi_{(t)}(\mathbf{k}_1,\mathbf{r}_1,\mathbf{k}_2,\mathbf{r}_2) = \sum_{\substack{i_1,l_1,i_2,l_2\\L,M}} \langle\Psi_{\substack{i_1,l_1,i_2,l_2\\L,M}}|\Phi_{(t)}(\mathbf{k}_1,\mathbf{r}_1,\mathbf{k}_2,\mathbf{r}_2)\rangle\cdot|\Psi_{\substack{i_1,l_1,i_2,l_2\\L,M}}\rangle \tag{7.8}$$

This completes formalism needed for the surface integral technique, where the transition amplitude to double ionization state, with outgoing electrons having momenta $\mathbf{k}_1$ and $\mathbf{k}_2$, given by:

$$f(\mathbf{k}_1,\mathbf{k}_2) = \oint_S \left(\Phi^*_{(t)}\boldsymbol{\nabla}\Psi^{(+)}_{sc} - \Psi^{(+)}_{sc}\boldsymbol{\nabla}\Phi^*_{(t)}\right)d\boldsymbol{a}, \tag{7.9}$$

where $\oint_S$ indicates integration over all angular coordinates and rectangular integration curve in equation 7.1.

We define single $Y_{l_{k_1},m_1}(\hat{\mathbf{k}_1})Y_{l_{k_2},m_2}(\hat{\mathbf{k}_2})$ component of testing function in equation 7.3 by writing

$$\Phi_{(t),l_{k_1},m_1,l_{k_2},m_2}(\mathbf{k}_1,\mathbf{r}_1,\mathbf{k}_2,\mathbf{r}_2) \equiv \varphi_{l_{k_1},l_1,m_1}(r_1)\varphi_{l_{k_2},l_2,m_2}(r_2)Y_{l_1,m_1}(\hat{\mathbf{r}_1})Y_{l_2,m_2}(\hat{\mathbf{r}_2}). \tag{7.10}$$

We express the transition amplitude as a sum of (uncoupled) product of spherical harmonics terms for wave vectors $\mathbf{k}_1$ and $\mathbf{k}_2$:

$$f(\mathbf{k}_1,\mathbf{k}_2) = \sum_{l_{k_1},m_1,l_{k_2},m_2} f_{l_{k_1},m_1,l_{k_2},m_2}(k_1,k_2)Y_{l_{k_1},m_1}(\hat{\mathbf{k}_1})Y_{l_{k_2},m_2}(\hat{\mathbf{k}_2}), \tag{7.11}$$

where,

$$f_{l_{k_1},m_1,l_{k_2},m_2}(k_1,k_2) \equiv \oint_S \left(\Phi^*_{(t),l_{k_1},m_1,l_{k_2},m_2}\boldsymbol{\nabla}\Psi^{(+)}_{sc} - \Psi^{(+)}_{sc}\boldsymbol{\nabla}\Phi^*_{(t),l_{k_1},m_1,l_{k_2},m_2}\right)d\boldsymbol{a}, \tag{7.12}$$

is single $Y_{l_{k_1},m_1}(\hat{\mathbf{k}_1})Y_{l_{k_2},m_2}(\hat{\mathbf{k}_2})$ term in surface integral, independent of direction of outgoing electrons.

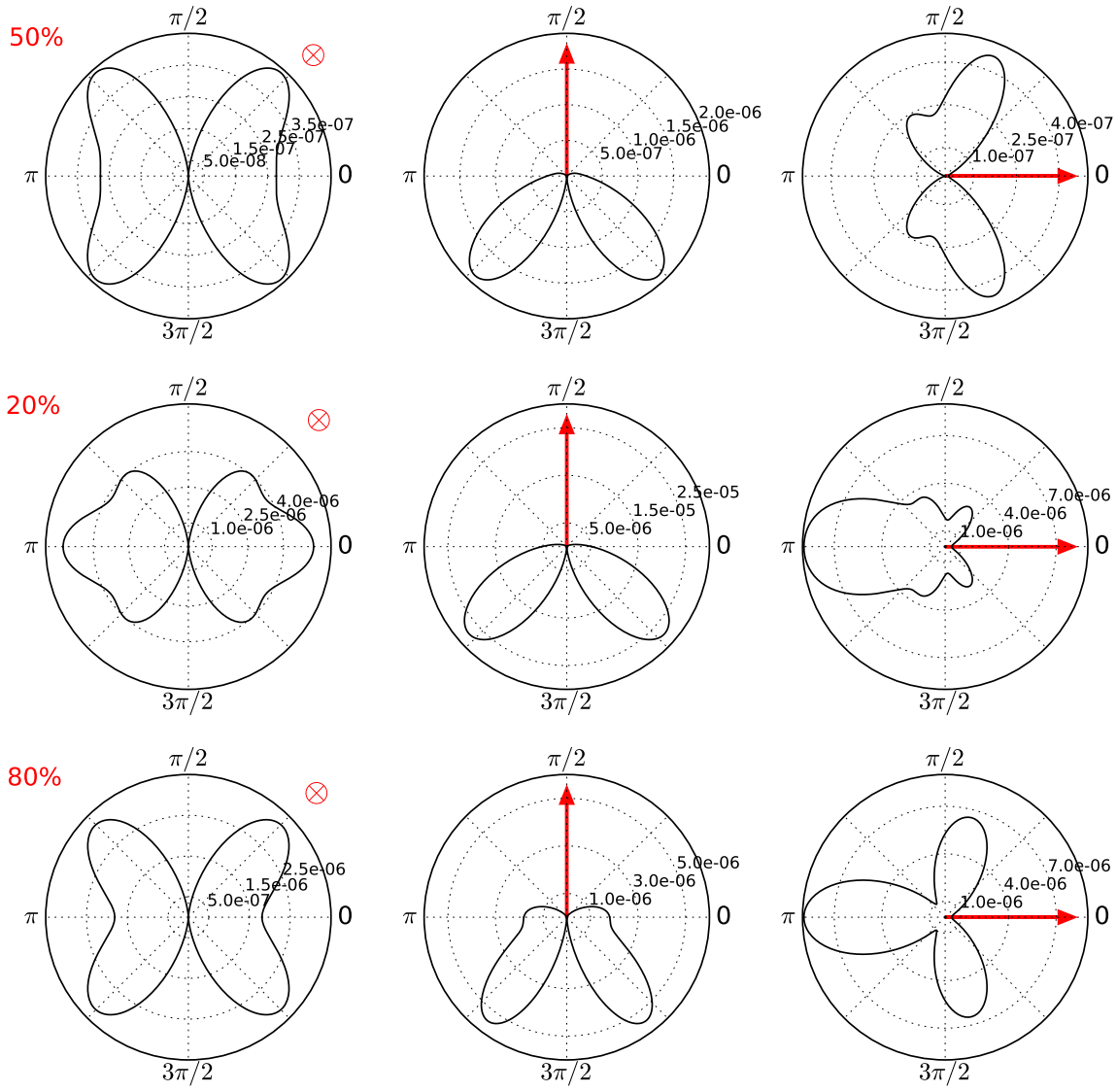

Fig. 7.7 One-photon double ionisation: triply differential probability (TDP) for H_2 in fixed nuclei approximation by time-independent surface integral method. Photon energy $\omega = 2.75620 a.u.$. The molecule is aligned along z-axis (protons placed at $\theta_2 = 0$ and $\theta_2 = \pi$ angular coordinate in plot). Red arrow indicates the outgoing direction of the fixed electron for in-plane-geometry, for out-of-plane geometry red cross indicates direction perpendicular to the page of fixed electron. Polar plot represents angular distribution of probability of detection of second electron (black curve), as a function of θ_2 coordinate of not fixed electron in $\phi_2 = 0$ plane. Rows represents 50%, 20% and 80% of energy sharing carried by fixed electron. (data in length gauge are multiplied by ω and in velocity by $1/\omega$).

In figures 7.6 and 7.7 we show the angular distributions resulting after one-photon double ionization of H_2 for a photon energy of $2.75 a.u.$. We explore the interaction with linearly polarized light parallel to the molecular axis. The plots show the double ionization probability $|f(\mathbf{k}_1, \mathbf{k}_2)|^2$ (black line) as a function of angular coordinate θ_2 of second electron in $\phi_2 = 0$ plane (paper plane), where k_2, θ_2, ϕ_2 are spherical coordinates of $\mathbf{k}_2$ vector. We fix $\mathbf{k}_1$ direction of first electron, indicated by red arrow and cross in plots. For geometry where the fixed electron moves in $\phi_2 = 0$ (paper plane) red arrow indicate outgoing direction, and for out-of-plane geometry where, fixed electron is perpendicular to the page as red cross. Molecule is aligned along z-axes or $\theta_1 = 0$. In figure 7.6, we show convergence in integration radius r_{int}, where we checked that the ionization probabilities are converged for $l_{max} = 5$. It should be remark that the convergence with the angular momenta strongly depends on the photon energy absorbed. On left we see convergence in r_{int} for velocity and in central plot for length gauge. In the right plot we see perfect agreement between results obtained with length and velocity gauge. For comparison, the length gauge data have been multiplied by ω and the velocity results have been multiplied by $1/\omega$ factor. Figure 7.7 shows the angular distribution for one-photon double ionization for three different energy sharings. We plot results for which the fixed electron carries 50% (upper row), 20% (middle row) and 80% (lower row) of the total available energy. We also include three different directions for the fixed electron: out-of plane geometry (firs column) column) and in-plane geometry for fixed electron perpendicular (second column) and aligned with (third column) with field and molecular axes. In all cases we find an excellent agreement with results obtained in reference [82], therefore validating the accuracy of our current implementation.

7.3 Time-dependent Schrödinger equation

The solution of the Schrödinger equation, given in equation 4.12, provides the evolution of the system in time under the influence of an external field. The given numerical wave function thus contains all possible breakup channels that can be retrieved by computing the quantum-mechanical flux or, more conveniently, applying the surface integral method. In this section, we perform calculations where Hamiltonian consists of field-free part and time-dependent laser-molecule interaction, described in semiclassical dipole approximation (see section 2.3.2). We assume, system is initially in ground state $\Psi_0(\mathbf{r}_1, \mathbf{r}_2)$ of Σ_g symmetry, giving initial condition $\Psi(t = 0) = \Psi_0$ for TDSE and having final wave function $\Psi_{fin}\Psi(t = t_{fin})$ as a solution. From the expansion of wave

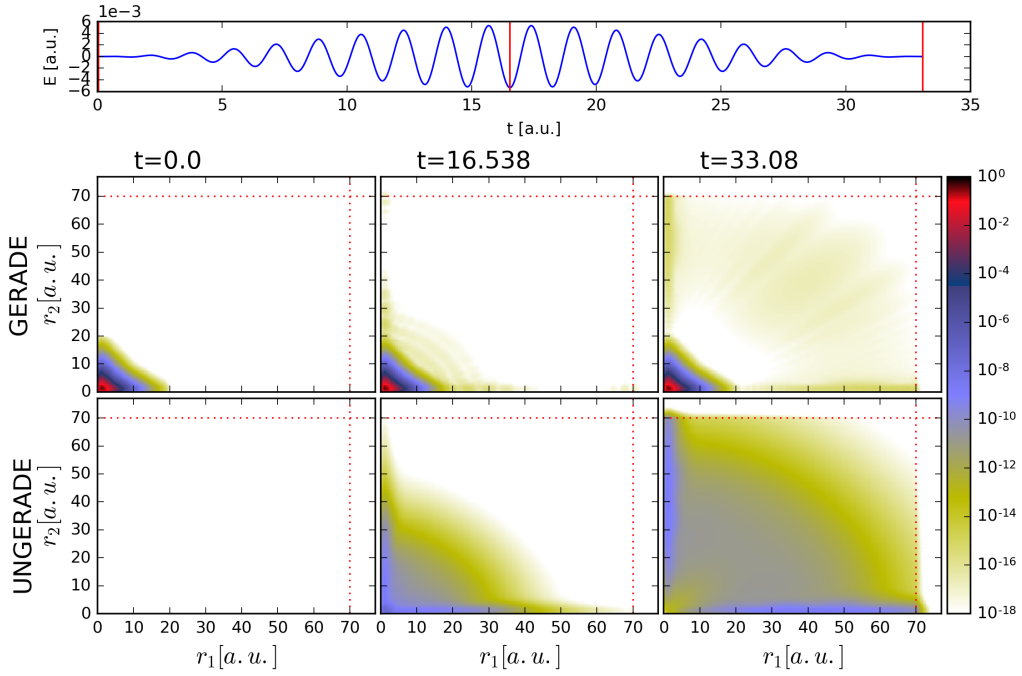

Fig. 7.8 Time propagation of H_2 system in fixed nuclei approximation, for $\sin^2$ pulse with pulse duration of $T = 800a.s.$ and central frequency $\omega_0 = 100eV$. Top panel: electric field of the pulse, with time points (red vertical line) in which the probability distribution is plotted below. Bottom panel: Probability distribution during the time propagation (columns), integrated over all angular coordinates, separated in gerade (up) and ungerade (down) contributions.

function in spherical harmonics, we can distinguish single- (ungerade) and two-photon (gerade) absorption processes (assuming gerade symmetry of ground state). In solving TDSE we apply different numerical methods listed in section 5.4, mostly Runge-Kutta ordinary differential equations solver schemes of order 4 with nonadaptive time steps.

In figure 7.8 we show a different processes in the wave function during the pulse propagation. We plot the probability distributing (like in the ground state in figure 7.2 on left) integrated over all angular coordinates ($\hat{\mathbf{r}_1}$ and $\hat{\mathbf{r}_2}$) of the wave function, for electric field shown in top panel, with pulse duration $T = 800a.s.$, central frequency $\omega_0 = 100eV$ and envelope of $\sin^2$ type. In bottom panel, we show gerade (up) and ungerade (down) contributions for three different times during the pulse propagation (different columns), indicated by red vertical lines in the electric field plot. The first column shows the initial ground state. Localized ground state in gerade symmetry remains the main contribution through the whole pulse propagation. Middle and third column, representing middle and end of the pulse, show pulse-initiated single

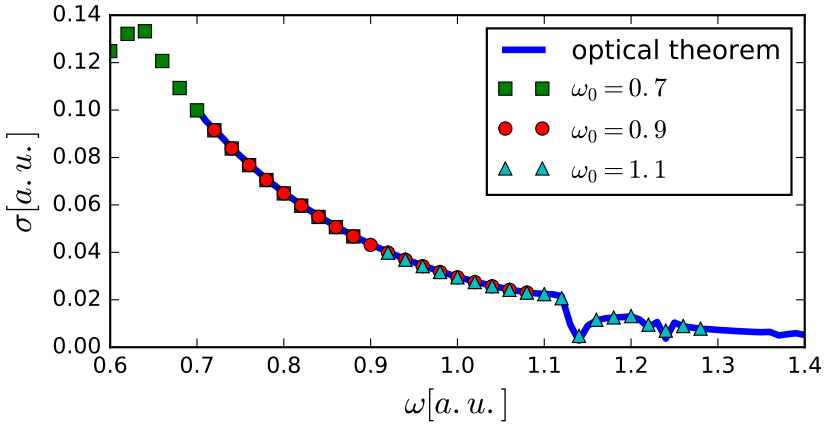

Fig. 7.9 SI cross section by time-dependent quantum-mechanical flux for H_2 in fixed nuclei approximation. Used pulses with $\sin^2$ envelopes, pulses duration of $T = 800a.s.$, intensities $I = 10^{12}W/cm^2$ and central frequencies $\omega_0 = 0.7a.u.$, $\omega_0 = 0.9a.u.$ and $\omega_0 = 1.1a.u.$. Compared with optical theorem calculations (full blue line).

single ionization, visible as probability localized close to axes (similar to He system, as explained in [20]), as well as double ionization visible as broad arcs of lower intensities. This is visible for one-photon (ungerade) and two-photon (gereade) processes. In the last column, we see absorption of energetically higher single ionization by ECS region (border marked by red doted line).

7.3.1 Quantum-mechanical flux

From the solution of TDSE, Ψ_{fin}, we compute the scattering wave function Ψ_{sc} using driven equation 4.16, which represents implicit field-free time propagation of Ψ_{fin} from $t = 0$ to $t = \infty$ and simultaneously Fourier transformation [60]. This gives single spectral component of scattering wave function, which contains contributions of all photoabsorption channels.

To demonstrate validity of solution of TDSE, we calculate the total cross section from quantum-mechanical flux from Ψ_{sc} using equation 4.17 and. 4.20, in the same way as in H_2^+ system (see section 5.3.2). Not having adequate method to separate single- and double-ionisation in quantum-mechanical flux, as in time-independent methods, we focus on one-photon single-ionisation energy region ($E_{tot} < 0$), to be able to compare the two approaches. In one-photon cross section calculated from TDSE, we have to take into account one-photon shape function, defined by Fourier transform of laser pulse (see equation 4.18) [60].

The correct one-photon single ionisation cross section is obtained for photon energies within pulses (one-photon) bandwidth, i.e. $\omega_0 - \Delta\omega < \omega < \omega_0 + \Delta\omega$ where ω_0 is central frequency of the pulse and $\Delta\omega = 2\pi/T$, for a pulse of duration T. Figure 7.9 shows one-photon SI cross section, computed by quantum-mechanical flux and using pulses with central frequencies of $\omega_0 = 0.7a.u.$, $\omega_0 = 0.9a.u.$ and $\omega_0 = 1.1a.u.$. We see perfect agreement of the time-independent results from optical theorem and the time-dependent quantum-mechanical flux method, supporting our effort toward time-dependent surface integral technique.

7.4 Two-photon double ionization of H_2: surface integral technique

Having independently checked that we have correct implementation of TDSE in section 7.3.1 and surface integral technique for extraction of observables in time-independent treatment in section 7.2.3, we combine the two methods into single method. We get a central method in this work, capable to extract one- and two-photon transition amplitudes (equation 7.11) in nonperturbative regime for Coulomb breakup channel. Same as in equation 4.39 for H_2^+ system, we compute the joint energy probability distribution $P(E_{k_1}, E_{k_2}))$ to the final state, where electrons have energies E_{k_1} and E_{k_2} as:

$$P(E_{k_1}, E_{k_2}) = \sum_{l_{k_1}, m_1, l_{k_2}, m_2} \left| f_{l_{k_1}, m_1, l_{k_2}, m_2}(k_1, k_2) \right|^2 . \tag{7.13}$$

By integration 7.13 over energies of one of electron we get single-electron energy probability distribution for double ionization:

$$P(E) = \int_0^{E_{tot}} P(E_{tot} - E', E') dE'. \tag{7.14}$$

To compare one-photon Coulomb breakup breakup computed in time-dependent and time-independent treatment, we chose pulse with $\sin^2$ envelopes, duration of $T = 800a.s.$, intensities $I = 10^{12} W/cm^2$ and central frequency same as photon energy used in figure 7.7: $\omega_0 = 2.75620a.u.$. From TDSE we calculate the scattering wave functions for final energy that corresponds to the central frequency of the pulse $E_1 + E_2 = \omega_0$. Using surface integral technique we get transition amplitudes for different energy sharings and outgoing directions of electrons. In figure 7.10, we show the calculated angular distributions, that show excellent (besides missing factor from

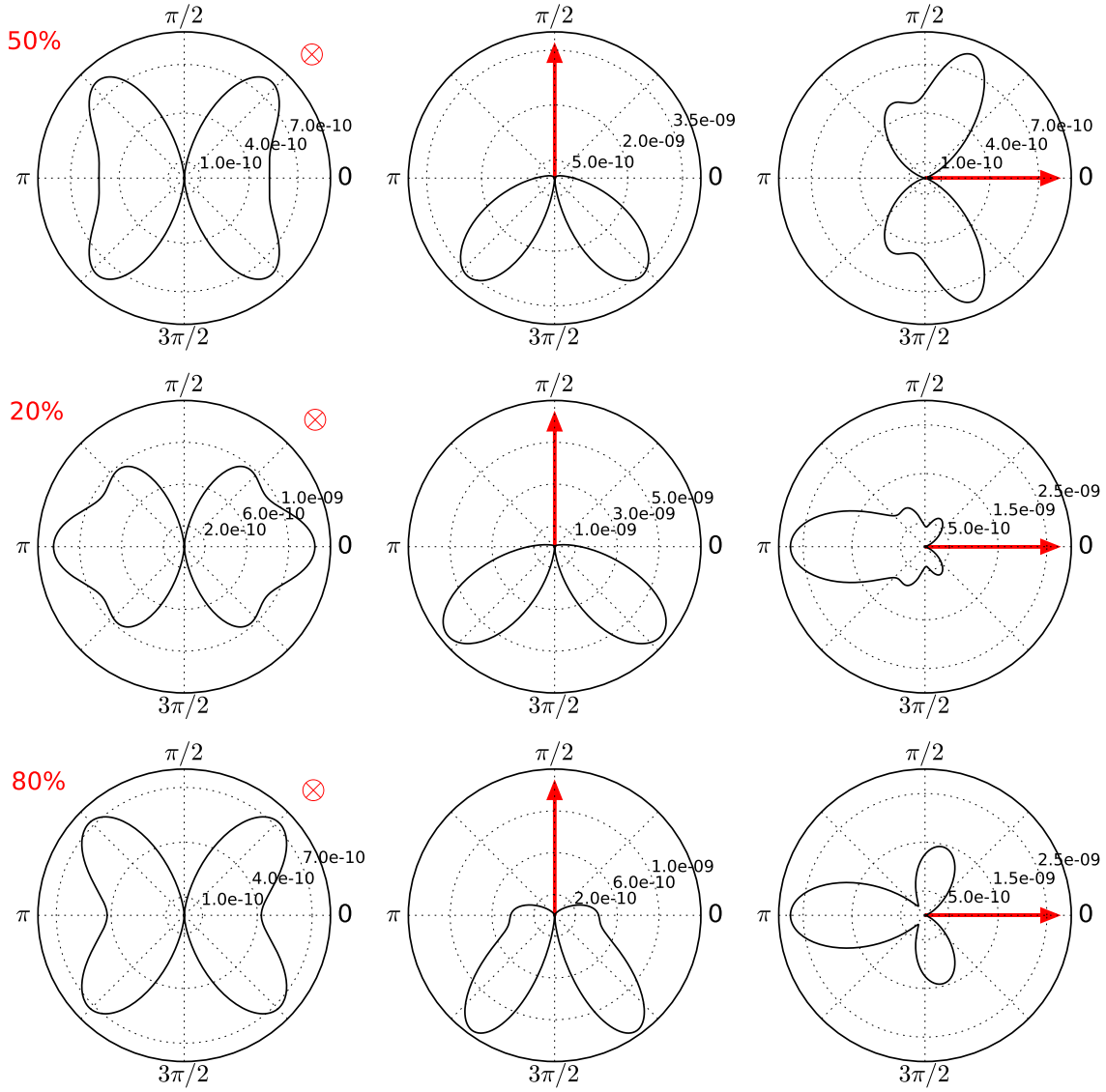

Fig. 7.10 Same as in figure 7.7, but with transition probability calculated in *time-dependent* surface integral method. Used pulses with $\sin^2$ envelope, duration of $T = 800 a.s.$, intensities $I = 10^{12} W/cm^2$ and central frequencies $\omega_0 = 2.75620 a.u.$ $(75eV)$. Final energy corresponds to the central frequency of pulse: $E_1 + E_2 = \omega_0$.

one-photon shape function [60]) agreement with the calculations in time-independent treatment from figure 7.7.

We perform a two calculations for pulses with $\sin^2$ envelopes, duration of $T = 550 a.s.$, central frequency $\omega_0 = 1.10248 a.u.$ $(30eV)$ and intensities $I = 10^{12} W/cm^2$ and $I = 3.5 \times 10^{14} W/cm^2$. In figure 7.11 we show that structure of energy differential probability does not depend on the intensity of the pulse and it favors unequal energy

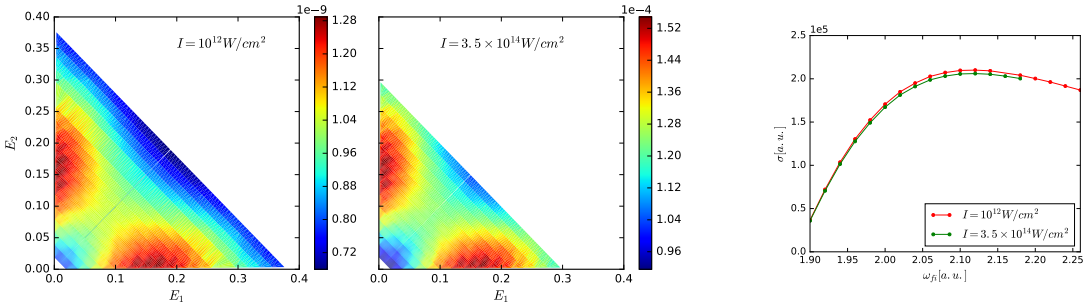

Fig. 7.11 Energy distribution probability for $\sin^2$ pulse with duration of $T = 550a.s.$, $\omega_0 = 1.10248a.u.$ and intensities $I = 10^{12}W/cm^2$ (left) and $I = 3.5 \times 10^{14}W/cm^2$ (center), and comparison of the total cross sections for the two pulses (right).

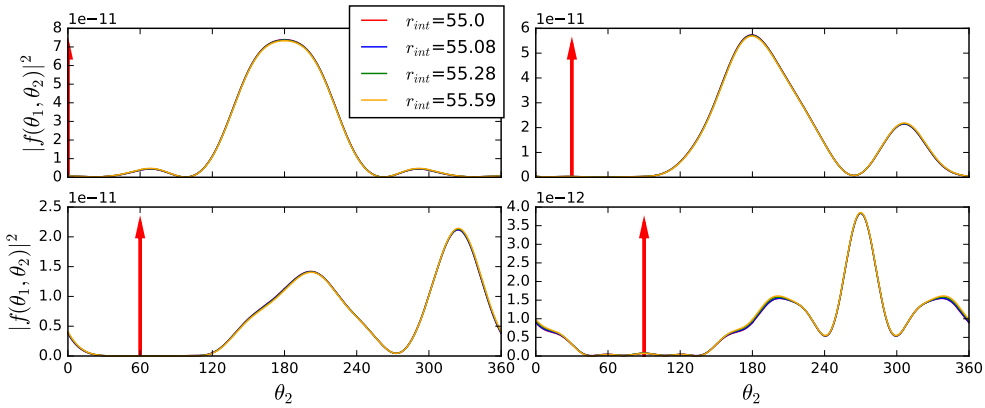

Fig. 7.12 Angular distributions of transition probability for two-photon Coulomb breakup, using pulse with $\sin^2$ envelope, duration of $T = 550a.s.$, intensities $I = 10^{12}W/cm^2$ and central frequencies $\omega_0 = 1.10248a.u.$ $(30eV)$. Final energy corresponds to the central frequency of pulse: $E_1 + E_2 = \omega_0$. Energy shared equally. Full line shows dependence of transition probability on outgoing direction of second electron: θ_2, while first electron is fixed. Red arrow indicates outgoing directions of fixed electron (θ_1) for in plane geometry, top left: $\theta_1 = 0$; top right $\theta_1 = \pi/6$; bottom left $\theta_1 = \pi/3$; bottom right $\theta_1 = 2\pi/6$. Colors in legend presents data obtained from different integration radii in surface integral.

sharing. We take into account the shape function from [62], where it is assumed that photon energy is not too close to being in resonance with a transition to one of the intermediate states, we get a cross section independent on intensity of the pulse, as shown in figure 7.11 on the right.

In figure 7.12 we reproduce the results of angular distributions for equal energy sharing from [32] (FIG. 2.) of ejected electrons, using the same pulse as in figure 7.11,

where we see good agreement in the structure of angular distributions with the data and references therein.

The applicability of FEM-DVR and ECS methods has been demonstrated for two-electron system, H_2 in fixed nuclei approximation, showing very good agreement in one- and two-photon single and double ionization between different approaches, as well as agreement with previously published results. We employed time-independent and time-dependent approach to one-photon double-ionization process that show perfect agreement, giving us confidence on accuracy of the method. We computed two-photon double-ionization angular distributions, where in literature agreement still has not been reached, that shows good agreement with the recent results. We also demonstrate agreement of cross section calculated by different laser pulses in one- and two-photon double ionization processes.

Chapter 8

Conclusions

Conclusion

A new full dimensional method, beyond the Born-Oppenheimer approximation, has been developed for the accurate description of the multi-photon Coulomb breakup problem of diatomic molecules. There is a need for a new numerical tools to treat the simplest molecular systems in full dimensionality. Most of the existing methods work within the fixed nuclei or the Born-Oppenheimer approximations and are only able to provide a realistic description of single ionization processes. We aim to move a step forward providing a method that enables an accurate representation of the non-adiabatic processes, as well as double ionization events. We test our newly developed implementation by comparing with a previous data when available. In particular, we discuss the suitability of different approaches (optical theorem, quantum-mechanical flux and surface integral approach) for the extraction of one- and two-photon absorption total cross sections.

We have used the H_2^+ system to benchmark our implementation to account for the coupled electron and nuclear dynamics. Moreover, we have used the simplest molecular system, H_2^+, to demonstrate a new scheme to retrieve the time-resolved images of molecular dynamics. We show that a single frequency-chirped ultrashort UV pulse can be used as an alternative to a conventional pump-probe, providing access to a time-resolved image of molecular ultrafast dynamics. We also show that by adjusting the chirp of the pulse, while keeping the power spectrum intact, we can achieve a significant enhancement the total ionization yield. Moreover, we show our preliminary simulations on one- and multi-photon double ionization of the hydrogen molecule in the fixed nuclei approximation. We particularly focused on the extraction of angle- and energy-differential double ionization probabilities. We also provide our most recent

results on the two-photon double ionization of H_2 in the fixed nuclei approximation, for which scarce results are available in the literature.

By developing the formalism for extraction of observables in Coulomb-breakup channel for H_2^+, and double-ionization channel in H_2 molecule in FNA, we have completed the formalism for a realistic description of the multi-photon breakup of H_2 molecule. We expect to use this methodology in the near future to produce the first simulation in full dimensionality for the two-photon double ionization of H_2, as well as to provide a complete description of unsolved problems as the neutral dissociation involving non-adiabatic couplings.

Conclusión

Se ha desarrollado un nuevo método teórico para obtener una descripción teórica exacta de los procesos de ruptura Coulombiana inducida por la absorción de varios fotones en moléculas diatómicas. La metodología incluye todas las dimensiones del problema y trabaja más allá de la aproximación Born-Oppenheimer. La mayor parte de los métodos existentes hasta la fecha emplean esta aproximación, o directamente trabajan en la aproximación de núcleos fijos, y en gran parte de estos casos, únicamente son capaces de tratar el problema de la ionización simple. Consecuentemente, nuestro objetivo es dar un paso más allá y desarrollar un método que permite incluir los procesos non-adiabáticos, y que a su vez, permita estudiar la doble ionización. Donde ha sido posible, la implementación aquí desarrollada se ha comparado con datos previos. Se ha hecho particular hincapié en la idoneidad de diferentes estrategias (resolviendo el teorema óptico, obteniendo flujo mecánico cuántico y realizando una integral de superficie) para la extracción de las secciones eficaces de absorción de uno y dos fotones.

Hemos empleado la molécula de H_2^+ como referencia inicial para la incorporación de la dinámica electrónica y nuclear acoplada. Además, hemos empleado el sistema molécular más sencillo, H_2^+, para mostrar un nuevo esquema capaz de obtener imágenes resueltas temporalmente de la dinámica molecular: demostramos que es posible usar un pulso ultracorto único, con una frecuencia variable en tiempo, como una alternativa a los métodos de bombeo-prueba (pump-probe) convencionales, dando así acceso a imágenes temporales de la dinámica molecular ultrarrápida. Mediante este esquema, es posible ajustar el parámetro de frecuencia variable en tiempo (chirp) del pulso manteniendo intacto el espectro de frecuencias, para manipular y lograr un incremento significativo de la eficiencia de ionización total. Además, hemos mostrado nuestros resultados más recientes, resultados preliminares, de nuestras simulaciones de doble

ionización de la molécula de hidrógeno obtenidos en la aproximación de núcleos fijos. Se ha puesto particular atención a la extracción de probabilidades de doble ionización diferenciales en ángulo y energía. También, se han aportado nuestros últimos resultados en la doble ionización de H_2 por absorción de dos fotones en la aproximación de núcleos fijos, problema para los que existen escasos datos en la literatura hasta el momento.

En resumen, se ha completado el formalismo para obtener una descripción exacta, en toda su dimensionalidad, de todos los canales de ruptura posibles en la molécula de hidrógeno tras la absorcón de cualquier número de fotones. En el futuro más inmediato, esperamos producir la primera simulación incluyendo todos los grados de libertad para la doble ionización de H_2 por absorción de dos fotones, así como proveer una descripción completa de otros fenómenos que aún quedan por explorar como la disociación en neutros, para los que los acoplamientos no adiabáticos pueden jugar un papel relevante.

References

[1] Adler, A., Rachman, A., and Robinson, E. J. (1995). A time-dependent theory of resonant multiphoton ionization of atoms by short pulses. I. Weak-field results for the two-photon ionization of caesium. *J. Phys. B*, 28(23):5057.

[2] Alt, E. O. and Mukhamedzhanov, A. M. (1993). Asymptotic solution of the schrödinger equation for three charged particles. *Phys. Rev. A*, 47:2004–2022.

[3] Assion, A., Baumert, T., Bergt, M., Brixner, T., Kiefer, B., Seyfried, V., Strehle, M., and Gerber, G. (1998). Control of Chemical Reactions by Feedback-Optimized Phase-Shaped Femtosecond Laser Pulses. *Science*, 282(5390):919.

[4] Ayvazyan, V., Baboi, N., Bähr, J., Balandin, V., Beutner, B., Brandt, A., Bohnet, I., Bolzmann, A., Brinkmann, R., Brovko, O., et al. (2006). First operation of a free-electron laser generating gw power radiation at 32 nm wavelength. *The European Physical Journal D-Atomic, Molecular, Optical and Plasma Physics*, 37(2):297–303.

[5] Bachau, H., Cormier, E., Decleva, P., Hansen, J., and Martín, F. (2001). Applications of b-splines in atomic and molecular physics. *Reports on Progress in Physics*, 64(12):1815.

[6] Balay, S., Abhyankar, S., Adams, M. F., Brown, J., Brune, P., Buschelman, K., Dalcin, L., Eijkhout, V., Gropp, W. D., Kaushik, D., Knepley, M. G., McInnes, L. C., Rupp, K., Smith, B. F., Zampini, S., Zhang, H., and Zhang, H. (2016). PETSc Web page. http://www.mcs.anl.gov/petsc.

[7] Bostedt, C., Boutet, S., Fritz, D. M., Huang, Z., Lee, H. J., Lemke, H. T., Robert, A., Schlotter, W. F., Turner, J. J., and Williams, G. J. (2016). Linac Coherent Light Source: The first five years. *Rev. Mod. Phys.*, 88(1):015007.

[8] Bostedt, C., Chapman, H. N., Costello, J. T., Crespo López-Urrutia, J. R., Düsterer, S., Epp, S. W., Feldhaus, J., Föhlisch, A., Meyer, M., Möller, T., Moshammer, R., Richter, M., Sokolowski-Tinten, K., Sorokin, A., Tiedtke, K., Ullrich, J., and Wurth, W. (2009). Experiments at FLASH. *Nucl. Inst. Meth. A*, 601(1-2):108.

[9] Brixner, T., Krampert, G., Pfeifer, T., Selle, R., Gerber, G., Wollenhaupt, M., Graefe, O., Horn, C., Liese, D., and Baumert, T. (2004). Quantum Control by Ultrafast Polarization Shaping. *Phys. Rev. Lett.*, 92(20):208301.

[10] Brumer, P. and Shapiro, M. (1989). One photon mode selective control of reactions by rapid or shaped laser pulses: An emperor without clothes? *Chem. Phys.*, 139(1):221.

[11] Campi, F., Coudert-Alteirac, H., Miranda, M., Rading, L., Manschwetus, B., Rudawski, P., L'Huillier, A., and Johnsson, P. (2016). Design and test of a broadband split-and-delay unit for attosecond XUV-XUV pump-probe experiments. *Rev. Sci. Inst.*, 87(2):023106.

[12] Carpeggiani, P. A., Tzallas, P., Palacios, A., Gray, D., Martín, F., and Charalambidis, D. (2014). Disclosing intrinsic molecular dynamics on the 1-fs scale through extreme-ultraviolet pump-probe measurements. *Phys. Rev. A*, 89(2):023420.

[13] Chang, Z. (2005). Chirp of the single attosecond pulse generated by a polarization gating. *Phys. Rev. A*, 71(2):023813.

[14] Chatel, B., Degert, J., Stock, S., and Girard, B. (2003). Competition between sequential and direct paths in a two-photon transition. *Phys. Rev. A*, 68(4):041402.

[15] Chatel, B. and Girard, B. (2005). Coherent Control of Atomic Dynamics with Chirped and Shaped Pulses. In *Femtosecond Laser Spectroscopy*, pages 267–304. Springer-Verlag, New York.

[16] Colgan, J., Pindzola, M. S., and Robicheaux, F. (2007). Triple differential cross sections for the double photoionization of h_2. *Phys. Rev. Lett.*, 98:153001.

[17] Djotyan, G. P., Bakos, J. S., Sörlei, Z., and Szigeti, J. (2004). Coherent control of atomic quantum states by single frequency-chirped laser pulses. *Phys. Rev. A*, 70(6):063406.

[18] Drescher, M., Hentschel, M., Kienberger, R., Tempea, G., Spielmann, C., Reider, G. A., Corkum, P. B., and Krausz, F. (2001). X-ray pulses approaching the attosecond frontier. *Science*, 291(5510):1923–1927.

[19] Dudovich, N., Dayan, B., Gallagher Faeder, S., and Silberberg, Y. (2001). Transform-Limited Pulses Are Not Optimal for Resonant Multiphoton Transitions. *Phys. Rev. Lett.*, 86(1):47.

[20] Feist, J., Nagele, S., Pazourek, R., Persson, E., Schneider, B., Collins, L., and Burgdörfer, J. (2008). Nonsequential two-photon double ionization of helium. *Physical Review A*, 77(4):043420.

[21] Feist, J., Nagele, S., Ticknor, C., Schneider, B. I., Collins, L. A., and Burgdörfer, J. (2011). Attosecond Two-Photon Interferometry for Doubly Excited States of Helium. *Phys. Rev. Lett.*, 107(9):093005.

[22] Felinto, D. and López, C. E. E. (2009). Theory for direct frequency-comb spectroscopy. *Phys. Rev. A*, 80(1):013419.

[23] Friedrich, H. and Friedrich, H. (2006). *Theoretical atomic physics*, volume 3. Springer.

[24] Guan, X., Bartschat, K., and Schneider, B. I. (2011). Breakup of the aligned h_2 molecule by xuv laser pulses: A time-dependent treatment in prolate spheroidal coordinates. *Phys. Rev. A*, 83:043403.

[25] Guan, X., Bartschat, K., Schneider, B. I., and Koesterke, L. (2014). Effects of autoionizing states on two-photon double ionization of the h2 molecule. In *Journal of Physics: Conference Series*, volume 488, page 012024. IOP Publishing.

[26] Haxton, D. J. (2013). Breakup of $\mathbf{H}_2{}^+$ by photon impact. *Phys. Rev. A*, 88:013415.

[27] Hernandez, V., Roman, J. E., and Vidal, V. (2005). SLEPc: A scalable and flexible toolkit for the solution of eigenvalue problems. *ACM Trans. Math. Software*, 31(3):351–362.

[28] Hijikata, Y., Nakashima, H., and Nakatsuji, H. (2009). Solving non-born–oppenheimer schrödinger equation for hydrogen molecular ion and its isotopomers using the free complement method. *The Journal of chemical physics*, 130(2):024102.

[29] Hofstetter, M., Schultze, M., Fieß, M., Dennhardt, B., Guggenmos, A., Gagnon, J., Yakovlev, V. S., Goulielmakis, E., Kienberger, R., Gullikson, E. M., Krausz, F., and Kleineberg, U. (2011). Attosecond dispersion control by extreme ultraviolet multilayer mirrors. *Opt. Expr.*, 19(3):1767.

[30] Horner, D. A., Morales, F., Rescigno, T. N., Martín, F., and McCurdy, C. W. (2007). Two-photon double ionization of helium above and below the threshold for sequential ionization. *Phys. Rev. A*, 76:030701.

[31] Igarashi, A. (2014). Cross sections for dissociative ionization and dissociative excitation of $\mathbf{H}_2{}^+$ by single photon absorption. *The European Physical Journal D*, 68(9):266.

[32] Ivanov, I. and Kheifets, A. (2013). Two-photon double ionization of the h 2 molecule: Cross sections and amplitude analysis. *Physical Review A*, 87(2):023414.

[33] Jackson, J. D. (1975). *Electrodynamics*. Wiley Online Library.

[34] Jelovina, D., Feist, J., Martín, F., and Palacios, A. (2017). Imaging ultrafast molecular wave packets with a single chirped uv pulse. *Physical Review A*, 95(4):043424.

[35] Kadyrov, A. S., Mukhamedzhanov, A. M., and Stelbovics, A. T. (2003). Asymptotic form of the electron-hydrogen scattered wave. *Phys. Rev. A*, 67:024702.

[36] Kling, M. F. and Vrakking, M. J. J. (2008). Attosecond Electron Dynamics. *Annu. Rev. Phys. Chem.*, 59(1):463.

[37] Kol/os, W., Szalewicz, K., and Monkhorst, H. J. (1986). New born–oppenheimer potential energy curve and vibrational energies for the electronic ground state of the hydrogen molecule. *The Journal of Chemical Physics*, 84(6):3278–3283.

[38] Krausz, F. and Ivanov, M. (2009). Attosecond physics. *Rev. Mod. Phys.*, 81(1):163.

[39] Krylov, V. I. and Stroud, A. H. (2006). *Approximate calculation of integrals*. Courier Corporation.

[40] Kurka, M., Feist, J., Horner, D., Rudenko, A., Jiang, Y., Kühnel, K., Foucar, L., Rescigno, T., McCurdy, C., Pazourek, R., et al. (2010). Differential cross sections for non-sequential double ionization of he by 52 ev photons from the free electron laser in hamburg, flash. *New Journal of Physics*, 12(7):073035.

[41] Levis, R. J., Menkir, G. M., and Rabitz, H. (2001). Selective Bond Dissociation and Rearrangement with Optimally Tailored, Strong-Field Laser Pulses. *Science*, 292(5517):709.

[42] Lünnemann, S., Kuleff, A. I., and Cederbaum, L. S. (2008). Charge migration following ionization in systems with chromophore-donor and amine-acceptor sites. *The Journal of chemical physics*, 129(10):104305.

[43] Macías, A., Martín, F., Riera, A., and Yaanez, M. (1988). A practical solution to the "unknown normalization" problem. *International journal of quantum chemistry*, 33(4):279–300.

[44] Manolopoulos, D. and Wyatt, R. (1988). Quantum scattering via the log derivative version of the kohn variational principle. *Chemical physics letters*, 152(1):23–32.

[45] Marante, C., Klinker, M., Corral, I., González-Vázquez, J., Argenti, L., and Martín, F. (2017). Hybrid-basis close-coupling interface to quantum chemistry packages for the treatment of ionization problems. *Journal of Chemical Theory and Computation*, 13(2):499–514. PMID: 28058835.

[46] Martín, F., Fernández, J., Havermeier, T., Foucar, L., Weber, T., Kreidi, K., Schöffler, M., Schmidt, L., Jahnke, T., Jagutzki, O., et al. (2007). Single photon-induced symmetry breaking of h2 dissociation. *Science*, 315(5812):629–633.

[47] McCurdy, C. and Rescigno, T. (1997). Calculating differential cross sections for electron-impact ionization without explicit use of the asymptotic form. *Physical Review A*, 56(6):R4369.

[48] McCurdy, C. and Rescigno, T. (2000). Practical calculations of quantum breakup cross sections. *Physical Review A*, 62(3):032712.

[49] McCurdy, C. W., Baertschy, M., and Rescigno, T. N. (2004a). Solving the three-body coulomb breakup problem using exterior complex scaling. *Journal of Physics B: Atomic, Molecular and Optical Physics*, 37(17):R137.

[50] McCurdy, C. W., Horner, D. A., and Rescigno, T. N. (2002). Time-dependent approach to collisional ionization using exterior complex scaling. *Physical Review A*, 65(4):042714.

[51] McCurdy, C. W., Horner, D. A., Rescigno, T. N., and Martín, F. (2004b). Theoretical treatment of double photoionization of helium using a *b*-spline implementation of exterior complex scaling. *Phys. Rev. A*, 69:032707.

[52] Meier, C. and Engel, V. (1994). Interference structure in the photoelectron spectra obtained from multiphoton ionization of na_2 with a strong femtosecond laser pulse. *Phys. Rev. Lett.*, 73:3207–3210.

[53] Meshulach, D. and Silberberg, Y. (1998). Coherent quantum control of two-photon transitions by a femtosecond laser pulse. *Nature*, 396(6708):239.

[54] Meshulach, D. and Silberberg, Y. (1999). Coherent quantum control of multiphoton transitions by shaped ultrashort optical pulses. *Phys. Rev. A*, 60(2):1287.

[55] Morales, F., Martin, F., Horner, D. A., Rescigno, T. N., and McCurdy, C. W. (2009). Two-photon double ionization of h 2 at 30 ev using exterior complex scaling. *Journal of Physics B: Atomic, Molecular and Optical Physics*, 42(13):134013.

[56] Nakajima, T. (2007). Above-threshold ionization by chirped laser pulses. *Phys. Rev. A*, 75(5):053409.

[57] Nuernberger, P., Selle, R., Langhojer, F., Dimler, F., Fechner, S., Gerber, G., and Brixner, T. (2009). Polarization-shaped femtosecond laser pulses in the ultraviolet. *J. Opt. A*, 11(8):085202.

[58] Palacios, A., Bachau, H., and Martín, F. (2005). Resonant effects in the coulomb explosion of h_2^+ by ultrashort laser pulses. *Journal of Physics B: Atomic, Molecular and Optical Physics*, 38(6):L99.

[59] Palacios, A., González-Castrillo, A., and Martín, F. (2014). Molecular interferometer to decode attosecond electron-nuclear dynamics. *Proc. Natl. Acad. Sci.*, 111(11):3973.

[60] Palacios, A., McCurdy, C. W., and Rescigno, T. N. (2007). Extracting amplitudes for single and double ionization from a time-dependent wave packet. *Physical Review A*, 76(4):043420.

[61] Palacios, A., Rescigno, T., and McCurdy, C. (2009a). Time-dependent treatment of two-photon resonant single and double ionization of helium by ultrashort laser pulses. *Physical Review A*, 79(3):033402.

[62] Palacios, A., Rescigno, T. N., and McCurdy, C. W. (2008). Cross sections for short-pulse single and double ionization of helium. *Physical Review A*, 77(3):032716.

[63] Palacios, A., Rescigno, T. N., and McCurdy, C. W. (2009b). Two-electron time-delay interference in atomic double ionization by attosecond pulses. *Physical review letters*, 103(25):253001.

[64] Palacios, A., Sanz-Vicario, J. L., and Martín, F. (2015). Theoretical methods for attosecond electron and nuclear dynamics: applications to the h 2 molecule. *Journal of Physics B: Atomic, Molecular and Optical Physics*, 48(24):242001.

[65] Peng, L.-Y., Tan, F., Gong, Q., Pronin, E. A., and Starace, A. F. (2009). Few-cycle attosecond pulse chirp effects on asymmetries in ionized electron momentum distributions. *Phys. Rev. A*, 80(1):013407.

[66] Pronin, E. A., Starace, A. F., Frolov, M. V., and Manakov, N. L. (2009). Perturbation theory analysis of attosecond photoionization. *Phys. Rev. A*, 80(6):063403.

[67] Pronin, E. A., Starace, A. F., and Peng, L.-Y. (2011). Perturbation-theory analysis of ionization by a chirped few-cycle attosecond pulse. *Phys. Rev. A*, 84(1):013417.

[68] Rescigno, T. and McCurdy, C. (2000). Numerical grid methods for quantum-mechanical scattering problems. *Physical review A*, 62(3):032706.

[69] Sánchez, I. and Martín, F. (1997). Representation of the electronic continuum of with b-spline basis. *Journal of Physics B: Atomic, Molecular and Optical Physics*, 30(3):679.

[70] Sansone, G., Benedetti, E., Calegari, F., Vozzi, C., Avaldi, L., Flammini, R., Poletto, L., Villoresi, P., Altucci, C., Velotta, R., et al. (2006). Isolated single-cycle attosecond pulses. *Science*, 314(5798):443–446.

[71] Scrinzi, A. and Elander, N. (1993). A finite element implementation of exterior complex scaling for the accurate determination of resonance energies. *The Journal of chemical physics*, 98(5):3866–3875.

[72] Scrinzi, A., Ivanov, M. Y., Kienberger, R., and Villeneuve, D. M. (2006). Attosecond physics. *J. Phys. B*, 39(1):R1.

[73] Sekikawa, T., Kosuge, A., Kanai, T., and Watanabe, S. (2004). Nonlinear optics in the extreme ultraviolet. *Nature*, 432(7017):605.

[74] Seres, J., Seres, E., Verhoef, A. J., Tempea, G., Streli, C., Wobrauschek, P., Yakovlev, V., Scrinzi, A., Spielmann, C., and Krausz, F. (2005). Laser technology: Source of coherent kiloelectronvolt x-rays. *Nature*, 433(7026):596–596.

[75] Silva, R. E. F., Catoire, F., Rivière, P., Niederhausen, T., Bachau, H., and Martín, F. (2015). Energy- and angle-resolved ionization of $h_2{}^+$ interacting with xuv subfemtosecond laser pulses. *Phys. Rev. A*, 92:013426.

[76] Simon, B. (1979). The definition of molecular resonance curves by the method of exterior complex scaling. *Physics Letters A*, 71(2-3):211–214.

[77] Sorokin, A., Wellhöfer, M., Bobashev, S., Tiedtke, K., and Richter, M. (2007). X-ray-laser interaction with matter and the role of multiphoton ionization: Free-electron-laser studies on neon and helium. *Physical Review A*, 75(5):051402.

[78] Stowe, M. C., Cruz, F. C., Marian, A., and Ye, J. (2006). High Resolution Atomic Coherent Control via Spectral Phase Manipulation of an Optical Frequency Comb. *Phys. Rev. Lett.*, 96(15):153001.

[79] Sun, Z. and Lou, N. (2003). Autler-townes splitting in the multiphoton resonance ionization spectrum of molecules produced by ultrashort laser pulses. *Phys. Rev. Lett.*, 91:023002.

[80] Takanashi, T., Golubev, N. V., Callegari, C., Fukuzawa, H., Motomura, K., Iablonskyi, D., Kumagai, Y., Mondal, S., Tachibana, T., Nagaya, K., Nishiyama, T., Matsunami, K., Johnsson, P., Piseri, P., Sansone, G., Dubrouil, A., Reduzzi, M., Carpeggiani, P., Vozzi, C., Devetta, M., Negro, M., Faccialà, D., Calegari, F., Trabattoni, A., Castrovilli, M. C., Ovcharenko, Y., Mudrich, M., Stienkemeier, F.,

Coreno, M., Alagia, M., Schütte, B., Berrah, N., Plekan, O., Finetti, P., Spezzani, C., Ferrari, E., Allaria, E., Penco, G., Serpico, C., De Ninno, G., Diviacco, B., Di Mitri, S., Giannessi, L., Jabbari, G., Prince, K. C., Cederbaum, L. S., Demekhin, P. V., Kuleff, A. I., and Ueda, K. (2017). Time-Resolved Measurement of Interatomic Coulombic Decay Induced by Two-Photon Double Excitation of Ne_2. *Phys. Rev. Lett.*, 118(3):033202.

[81] Tzallas, P., Skantzakis, E., Nikolopoulos, L. A. A., Tsakiris, G. D., and Charalambidis, D. (2011). Extreme-ultraviolet pump–probe studies of one-femtosecond-scale electron dynamics. *Nat. Phys.*, 7(10):781.

[82] Vanroose, W., Horner, D. A., Martin, F., Rescigno, T. N., and McCurdy, C. W. (2006). Double photoionization of aligned molecular hydrogen. *Physical Review A*, 74(5):052702.

[83] Vanroose, W., Martín, F., Rescigno, T. N., and McCurdy, C. W. (2005). Complete photo-induced breakup of the h2 molecule as a probe of molecular electron correlation. *Science*, 310(5755):1787–1789.

[84] Weiner, A. M. (2000). Femtosecond pulse shaping using spatial light modulators. *Rev. Sci. Inst.*, 71(5):1929.

[85] Wolniewicz, L. (1995). Adiabatic potentials of the lowest in 1 π g and 1, 3 δ g states of the hydrogen molecule. *Journal of Molecular Spectroscopy*, 169(2):329–340.

[86] Wolniewicz, L. and Staszewska, G. (2003). Excited 1πu states and the $1\pi u \rightarrow x1\sigma g+$ transition moments of the hydrogen molecule. *Journal of Molecular Spectroscopy*, 220(1):45–51.

[87] Wöstmann, M., Mitzner, R., Noll, T., Roling, S., Siemer, B., Siewert, F., Eppenhoff, S., Wahlert, F., and Zacharias, H. (2013). The XUV split-and-delay unit at beamline BL2 at FLASH. *J. Phys. B*, 46(16):164005.

[88] Yudin, G. L., Bandrauk, A. D., and Corkum, P. B. (2006). Chirped attosecond photoelectron spectroscopy. *Phys. Rev. Lett.*, 96:063002.

[89] Zewail, A. H. (2006). 4d ultrafast electron diffraction, crystallography, and microscopy. *Annu. Rev. Phys. Chem.*, 57:65–103.

[90] Zhang, S., Zhang, H., Jia, T., Wang, Z., and Sun, Z. (2009). Coherent control of two-photon transitions in a two-level system with broadband absorption. *Phys. Rev. A*, 80(4):043402.

Appendix A

Conversion of volume to surface integral

We can use the well known Green's theorem [33], which states that for any well-behaved functions ϕ and ψ, volume integral over three-dimensional volume V can be converted into two dimensional surface integral along closed surface S, bounding V. The theorem states:

$$\int_V \left(\phi\nabla^2\psi - \psi\nabla^2\phi\right) d^3x = \int_S \left(\phi\boldsymbol{\nabla}\psi - \psi\boldsymbol{\nabla}\phi\right)\hat{\boldsymbol{n}}da, \tag{A.1}$$

where d^3x is a volume element, da is area element and $\hat{\boldsymbol{n}}$ is a unit vector normal to the surface da and pointing outward. The theorem can be generated to N spaces, volumes and surfaces. Dimension of the space that we are going to use will depend on physical system and in general it corresponds to number independent variables that a wave function depends on.

The volume integral that we have is (4.22):

$$\int_V \Phi^*_{(t)}\left(E - T - V_1\right)\Psi^{(+)}_{sc}dV, \tag{A.2}$$

where volume element dV has to be understood as volume element in N-dimensional space.

We write explicitly single particle kinetic energy operators:

$$\begin{aligned}&\int_V \Phi^*_{(t)}\left(E - T - V_1\right)\Psi^{(+)}_{sc}dV = \\ &\int_V \left[\Phi^*_{(t)}\left(E - V_1\right)\Psi^{(+)}_{sc} - \frac{-1}{2}\Phi^*_{(t)}\nabla^2\Psi^{(+)}_{sc}\right]dV,\end{aligned} \tag{A.3}$$

now we apply the Green's theorem to the second term under integral to get and reorder the first therm since $E - V_1$ is scalar

$$\begin{aligned} &\int_V \Phi^*_{(t)} \left(E - V_1 - T\right) \Psi^{(+)}_{sc} dV = \\ &\int_V \Psi^{(+)}_{sc} \left(E - V_1 - T\right) \Phi^*_{(t)} + \int_S \left(\Phi^*_{(t)} \boldsymbol{\nabla} \Psi^{(+)}_{sc} - \Psi^{(+)}_{sc} \boldsymbol{\nabla} \Phi^*_{(t)}\right) \hat{\boldsymbol{n}} da. \end{aligned} \tag{A.4}$$

By noting that the testing function is eigenfunction of Hamiltonian $h_1 = T + V_1$, i.e. $\left(E - h_1\right) \left|\Phi_{(t)}\right\rangle = 0$, we can see that the first therm is zero and the result follows.

$$\int_V \Phi^*_{(t)} \left(E - V_1 - T\right) \Psi^{(+)}_{sc} dV = \int_S \left(\Phi^*_{(t)} \boldsymbol{\nabla} \Psi^{(+)}_{sc} - \Psi^{(+)}_{sc} \boldsymbol{\nabla} \Phi^*_{(t)}\right) \hat{\boldsymbol{n}} da. \tag{A.5}$$

Appendix B

Angular momentum algebra

For two angular momentum operators $\hat{\boldsymbol{L}}_1$, $\hat{\boldsymbol{L}}_2$ one can form two different sets of mutually commuting operators, the *uncoupled representation*

$$\hat{\boldsymbol{L}}_1^2, \hat{\boldsymbol{L}}_2^2, L_{1,z}, L_{2,z} \tag{B.1}$$

and the *coupled representation*

$$\hat{\boldsymbol{L}}_1^2, \hat{\boldsymbol{L}}_2^2, \hat{\boldsymbol{L}}^2, L_z, \tag{B.2}$$

where

$$\hat{\boldsymbol{L}} = \hat{\boldsymbol{L}}_1 + \hat{\boldsymbol{L}}_2. \tag{B.3}$$

The according eigenfunctions $|l_1, l_2, m_1, m_2\rangle$ and $|l_1, l_2, L, M\rangle$ are connected by the unitary transformations

$$|l_1, l_2, L, M\rangle = \sum_{m_1, m_2} \langle l_1, l_2, m_1, m_2 | l_1, l_2, L, M\rangle \, |l_1, l_2, m_1, m_2\rangle \tag{B.4}$$

and inverse

$$|l_1, l_2, m_1, m_2\rangle = \sum_{L, M} \langle l_1, l_2, L, M | l_1, l_2, m_1, m_2\rangle \, |l_1, l_2, L, M\rangle \, . \tag{B.5}$$

Clebsch-Gordan coefficients

The expansion coefficients in (B.4) and (B.4) are called *Clebsch-Gordan (CG) coefficients* and the standard phase convention is to make them real,

$$\langle l_1, l_2, L, M | l_1, l_2, m_1, m_2\rangle = \langle l_1, l_2, L, M | l_1, l_2, m_1, m_2\rangle \equiv \begin{bmatrix} l_1 & l_2 & L \\ m_1 & m_2 & M \end{bmatrix} \tag{B.6}$$

The CG are nonzero only if all of the following conditions (selection rules) are fulfield

$$\begin{aligned} &|l_1 - l_2| \leq L \leq l_1 + l_2 \\ &M \leq |L|, m_1 \leq |l_1|, m_2 \leq |l_2| \\ &m_1 + m_2 = M \\ &l_1 + l_2 + L \in \mathbb{N} \end{aligned} \tag{B.7}$$

The orthonormality relations of the CG coefficients are given by

$$\sum_{m_1,m_2} \begin{bmatrix} l_1 & l_2 & L \\ m_1 & m_2 & M \end{bmatrix} \begin{bmatrix} l_1 & l_2 & L' \\ m_1 & m_2 & M' \end{bmatrix} = \delta_{L,L'}\delta_{M,M'}, \tag{B.8}$$

and

$$\sum_{L,M} \begin{bmatrix} l_1 & l_2 & L \\ m_1 & m_2 & M \end{bmatrix} \begin{bmatrix} l_1 & l_2 & L \\ m_1{}' & m_2{}' & M \end{bmatrix} = \delta_{m_1,m_1'}\delta_{m_2,m_2'}. \tag{B.9}$$

Some important symmetry relations under the permutation of any two columns or the sign reversal of the projection quantum numbers are

$$\begin{bmatrix} l_1 & l_2 & L \\ m_1 & m_2 & M \end{bmatrix} = (-1)^{l_1+l_2-L} \begin{bmatrix} l_1 & l_2 & L \\ -m_1 & -m_2 & -M \end{bmatrix} \tag{B.10}$$

$$= (-1)^{l_1+l_2-L} \begin{bmatrix} l_2 & l_1 & L \\ m_2 & m_1 & M \end{bmatrix} \tag{B.11}$$

$$= (-1)^{l_2+m_2} \frac{\sqrt{2L+1}}{\sqrt{2l_2+1}} \begin{bmatrix} l_1 & L & l_2 \\ m_1 & -M & -m_2 \end{bmatrix}. \tag{B.12}$$

As a consequence of (B.10) for $m_1 = m_2 = M = 0$

$$\begin{bmatrix} l_1 & l_2 & L \\ 0 & 0 & 0 \end{bmatrix} = (-1)^{l_1+l_2-L} \begin{bmatrix} l_1 & l_2 & L \\ 0 & 0 & 0 \end{bmatrix}, \tag{B.13}$$

and for odd $l_1 + l_2 - L$, we have

$$\begin{bmatrix} l_1 & l_2 & L \\ 0 & 0 & 0 \end{bmatrix} = 0. \tag{B.14}$$

Wigner 3j-symbol

The Wigner 3j-symbols are closely related to the CG coefficients

$$\begin{pmatrix} l_1 & l_2 & L \\ m_1 & m_2 & M \end{pmatrix} \equiv \frac{(-1)^{l_1-l_2-M}}{\sqrt{2L+1}} \begin{bmatrix} l_1 & l_2 & L \\ m_1 & m_2 & M \end{bmatrix}, \tag{B.15}$$

but have higher symmetry because they remain unchanged under an even permutation of the columns,

$$\begin{pmatrix} l_1 & l_2 & L \\ m_1 & m_2 & M \end{pmatrix} = \begin{pmatrix} l_2 & L & l_1 \\ m_2 & M & m_1 \end{pmatrix} = \begin{pmatrix} L & l_1 & l_2 \\ M & m_1 & m_2 \end{pmatrix}, \tag{B.16}$$

and odd permutation brings in the phase factor $(-1)^{l_1+l_2+L}$

$$\begin{pmatrix} l_1 & l_2 & L \\ m_1 & m_2 & M \end{pmatrix} = (-1)^{l_1+l_2+L} \begin{pmatrix} l_2 & l_1 & L \\ m_2 & m_1 & M \end{pmatrix} \tag{B.17}$$

$$= (-1)^{l_1+l_2+L} \begin{pmatrix} l_1 & L & l_2 \\ m_1 & M & m_2 \end{pmatrix} \tag{B.18}$$

$$= (-1)^{l_1+l_2+L} \begin{pmatrix} L & l_2 & l_1 \\ M & m_2 & m_1 \end{pmatrix}. \tag{B.19}$$

Reversing the sign of the projection quantum numbers gives the same phase factor

$$\begin{pmatrix} l_1 & l_2 & L \\ m_1 & m_2 & M \end{pmatrix} = (-1)^{l_1+l_2+L} \begin{pmatrix} l_1 & l_2 & L \\ -m_1 & -m_2 & -M \end{pmatrix} \tag{B.20}$$

The 3j-symbols fulfill the same selection rules as the CG coefficients since they differ only by a phase. In analogy to (B.8) and (B.9) the orthonormality relations of the Wigner 3j-symbols are

$$\sum_{m_1,m_2} \begin{pmatrix} l_1 & l_2 & L \\ m_1 & m_2 & M \end{pmatrix} \begin{pmatrix} l_1 & l_2 & L' \\ m_1 & m_2 & M' \end{pmatrix} = \frac{\delta_{L,L'}\delta_{M,M'}}{2L+1}, \tag{B.21}$$

$$\sum_{L,M} \begin{pmatrix} l_1 & l_2 & L \\ m_1 & m_2 & M \end{pmatrix} \begin{pmatrix} l_1 & l_2 & L \\ m_1{}' & m_2{}' & M \end{pmatrix} = \frac{\delta_{m_1,m_1'}\delta_{m_2,m_2'}}{2L+1}. \tag{B.22}$$